Accepted Manuscript

Geochemistry and depositional environments of Paleocene–Eocene phosphorites: Metlaoui Group, Tunisia

Hechmi Garnit, Salah Bouhlel, Ian Jarvis

PII: S1464-343X(17)30293-5

DOI: 10.1016/j.jafrearsci.2017.07.021

Reference: AES 2973

To appear in: *Journal of African Earth Sciences*

Received Date: 7 October 2016

Revised Date: 11 July 2017

Accepted Date: 14 July 2017

Please cite this article as: Garnit, H., Bouhlel, S., Jarvis, I., Geochemistry and depositional environments of Paleocene–Eocene phosphorites: Metlaoui Group, Tunisia, *Journal of African Earth Sciences* (2017), doi: 10.1016/j.jafrearsci.2017.07.021.

Journal of African Earth Sciences *** (2017) ***–***

Geochemistry and depositional environments of Paleocene–Eocene phosphorites: Metlaoui Group, Tunisia

Hechmi Garnit [a], Salah Bouhlel [a], Ian Jarvis [b,*]

[a] *University of Tunis El Manar, Faculty of Sciences of Tunis, Mineral Resources and Environment Lab (LR01ES06), Mineralogy and Geochemistry Research Group, 2092 Tunis, Tunisia*

[b] *Department of Geography and Geology, Kingston University London, Penrhyn Road, Kingston upon Thames KT1 2EE, UK*

*Corresponding author: Ian Jarvis

E-mail address: i.jarvis@kingston.ac.uk

ABSTRACT

The Late Paleocene–Early Eocene phosphorites of the Metlaoui Group in Tunisia are a world-class phosphate resource. We review the characteristics of phosphorites deposited in three areas: the Northern Basins; Eastern Basins; and Gafsa-Metlaoui Basin. Comprehensive new bulk rock elemental data are presented, together with complementary mineralogical and mineral chemical results. Carbonate fluorapatite (francolite) constitutes the dominant mineral phase in the deposits. Phosphorite samples are enriched in Cd, Sr, U, rare-earth elements and Y, together with environmentally diagnostic trace elements that provide detrital (Cr, Zr), productivity (Cu, Ni, Zn) and redox (Mo, V) proxies. Suboxic bottom-water conditions predominated, with suboxic to anoxic porewaters accompanying francolite precipitation. Phosphorite deposition occurred under increasingly arid climate conditions, accompanying global Paleocene–Eocene warming. The Northern Basins show the strongest Tethys Ocean influence, with surface seawater rare-earth element signatures consistently developed in the phosphorites. Bed-scale compositional variation indicates relatively unstable environmental conditions and episodes of sediment redeposition, with varying detrital supply and a relatively wet local climate. Glauconitic facies in the Northern Basins and the more isolated evaporite-associated phosphorites in the dryer Eastern Basins display the greatest diagenetic influences. The phosphorite – organic-rich marl – diatom-bearing porcelanite facies association in the Gafsa-Metlaoui Basin represents the classic coastal upwelling trinity. Modified Tethyan waters occurred within the Basin during phosphorite deposition, with decreasing marine productivity from NW to SE evidenced by systematically falling enrichment factors for Cu, Ni, Cd and Zn in the phosphorites. Productivity declined in concert with increasing basin isolation during the deposition of the commercial phosphorite beds in the latest Paleocene to earliest Eocene. This isolation trend was temporarily reversed during an episode of maximum flooding associated with the earliest Eocene Paleocene–Eocene Thermal Maximum (PETM).

Keywords Phosphorites; Francolite; Geochemistry; Trace elements; Rare-earth elements and yttrium; Multivariate analysis; Tunisia; Palaeogeography; Paleocene-Eocene climate change; PETM.

1. Introduction

Tunisia is one of the largest producers of rock phosphate in the world: annual production was about 8 million tons of marketable phosphate in 2010 placing Tunisia 5th among the world producers of phosphate rock (Jasinski, 2011). The Tunisian revolution, which began in December 2010, led to a major decline in phosphate production during the period 2011–2015. However, production reached 3.5 million tons during 2016 (Jasinski, 2017). With political and social tensions easing, national and international private companies are investing in exploration and planning activities, with large reserves again under consideration for exploitation at the Sra Ouertane mine, Kef Governorate (Tunis-Afrique-Press, 2016), and elsewhere.

Phosphorites occur in three main areas of Tunisia: the Northern Basins, the Eastern Basins (North–South Axis area), and the Gafsa-Metlaoui Basin (Fig. 1). The phosphorites lie predominantly within the Paleocene–Eocene Chouabine Formation and its lateral equivalents within the Metlaoui Group; they form part of the Middle Eastern to North African Late Cretaceous–Paleogene phosphogenic province (Notholt, 1980; Sheldon, 1987; Notholt et al., 1989; Glenn et al., 1994; Lucas and Prévôt-Lucas, 1996). Economic phosphorite deposits occur principally in the Gafsa-Metlaoui Basin of central Tunisia. Here, phosphorites are exploited by the Compagnie des Phosphate de Gafsa (CPG), and are widely used as raw materials for fertilizer production by the Groupe Chimique Tunisien (GCT). In other Tunisian basins phosphorite beds are generally thinner and are of lower grade.

Previous studies have examined the stratigraphy, mineralogical composition, sedimentary facies, depositional environment, and diagenetic history of Tunisian phosphorites (Thomas, 1885; Cayeux, 1896, 1941; Pervinquière, 1903; Castany, 1951; Burollet, 1956; Sassi, 1974; Belayouni and Trichet, 1983; Chaabani, 1995; Béji-Sassi, 1999; Béji-Sassi and Sassi, 1999;

Zaïer, 1999; Felhi et al., 2008; Ben Hassen et al., 2009, 2010; Ferreira da Silva et al., 2010; Galfati et al., 2010; Ounis, 2011; Tlili et al., 2011; Garnit et al., 2012a, b; Kocsis et al., 2013, 2014; Galai and Sliman, 2014; Ahmed et al., 2015; El Ayachi et al., 2016), but geochemical data remain limited, particularly regarding sediments in the Northern and Eastern Basins. Published data are predominantly from the Gafsa-Metlaoui deposits, and were commonly obtained using analytical methodologies that have been superseded or recently improved. Despite the common geological setting of these phosphorites, considerable geochemical variability arises due to differences in palaeoenvironmental setting (basin configuration and lithofacies) and depositional conditions (redox values, productivity, and detrital flux; e.g. Garnit et al., 2012a; Kocsis et al., 2014).

Here, we present the first fully integrated geochemical study of Tunisia's three major phosphorite basins, and highlight key similarities and differences between them. This work addresses the abundances of major-, trace-, and rare-earth elements, their distribution patterns, and inter-element relationships. To identify the processes controlling phosphorite geochemistry, we have applied two multivariate statistical methods: principal components analysis (PCA) and hierarchical cluster analysis (HCA). Results are interpreted in a framework provided by a review of previous research in the area. The geochemical data offer insights into the depositional environments and geological history of Tunisia during the Paleogene. They further provide key parameters to inform the utilisation of phosphorites in applications that include agronomics, fertilizer technology, uranium and rare-earth element extraction, and provide constraints for environmental impact assessments (e.g. Ferreira da Silva et al., 2010).

2. Geological setting and study locations

North Africa during the Paleocene–Eocene represented one of the largest phosphogenic provinces in the geological record (Notholt et al., 1989). In Tunisia, commercial phosphorites occur principally in the Upper Paleocene–Lower Eocene Chouabine Formation of the Gafsa-Metlaoui area (Burollet, 1956; Sassi, 1974; Fournié, 1980; Fig. 1). Recent stable-isotope (C and O) and Sr-isotope stratigraphy, and palaeontological data, indicate that the main units of the phosphorite succession are of latest Paleocene, Thanetian age (Fig. 1C; Kocsis et al., 2013, 2014).

An important factor that contributed to the development of phosphorites in central Tunisia is the late Cretaceous tectonic framework, which generated a Late Paleocene – Early Eocene palaeogeography consisting of a shallow marine shelf bordering the open Tethys Ocean, punctuated by two gentle topographic highs (Fig. 1B): Kasserine Island in the centre; and Jeffara Island to the south (Sassi, 1974; Burollet and Oudin, 1980; Winnock, 1980; Chaabani, 1995; Zaïer et al., 1998). This configuration, and the development of local structurally controlled basins and highs, resulted in semi-restricted marine circulation and contributed to the trapping of abundant organic-rich sediments in the Gafsa-Metlaoui area, and other marginal basins.

Complex interactions between organic, inorganic, syngenetic and authigenic processes, and suitable redox conditions, led to the formation of apatite minerals (cf. Jarvis et al., 1994), and episodes of winnowing and reworking resulted in the concentration of pellets, coprolites and other mineralized grains to form beds of granular phosphorite (cf. Glenn et al., 1994; Föllmi, 1996). The chemistry of basin waters and subsequent post-depositional processes played significant roles in generating different phosphorite lithofacies (Ben Hassen et al., 2010; Galfati et al., 2010; Ounis, 2011).

Phosphorite deposits occur at a number of localities bordering Kasserine Island (Fig. 1B). The Northern Basins, situated to the north of the Island, representing a shallow open-marine platform setting (Garnit et al., 2012a). The Eastern Basins (Meknassy-Mezzouna Basins) and the Gafsa-Metlaoui Basin, situated to the east and south of Kasserine Island, respectively, were characterized by more restricted basin configurations (Belayouni et al., 1990; Garnit et al., 2012a; Kocsis et al., 2014).

Samples analyzed in the present study targeted phosphorites from each of the three basin areas (Figs. 1–5), sampled at eight locations: 2 in the Northern Basins; 1 in the Eastern Basins; and 5 in the Gafsa-Metlaoui Basin. These localities offer sufficient variation in facies and palaeogeographic setting to enable representative sampling of all three basins.

2.1 Northern Basins

The Northern Basins lie between 35°30’ – 36°30’N and 8°30’ – 9°15’E. The Basins are located in the central Atlas of Tunisia, to the south of the Diapirs Zone (Perthuisot, 1981) and extend westwards across the Algerian border. This zone covers the Thala–Tajerouine–El Kef areas, and contains NE–SW oriented folds crossed by the NW–SE trending Miocene–Quaternary Kalaat Khasba Graben in the west, and the Rohia Graben in the east (Haji et al., 2014; Fig. 2). During the Late Paleocene–Early Eocene phosphorites accumulated in the embayment between Kasserine Island and the Algerian Promontory (Fig. 1B), while farther to the north and northeast the successions pass into marls and shales with less phosphorite and more glauconite, indicative of less confined, deeper water and better-oxygenated environments (Sassi, 1974; Zaïer et al., 1998; Zaïer, 1999). The phosphorites show considerable lateral variation in thickness and phosphate content, accumulating in a series of small fault-controlled basins. Synsedimentary growth faults controlling sediment thickness are well expressed in both the Gafsa-Metlaoui and Northern Basins.

Phosphorites in the Northern Basins were studied at Sra Ouertane and Sekarna (Figs. 2, 5). The Sra Ouertane deposit is located approximately 40 km SE of El Kef, 50 km from the Algerian border. A structural interpretation of the deposit was presented by Zaïer et al. (1998, fig. 9). Following Zaïer (1999), the Chouabine Formation at Sra Ouertane may be subdivided into four units (Figs. 2B, 5; locality 1): Unit A, at the base, ranges from 0.3 to 75 m thick, and consists of alternating marls, carbonate and phosphorite beds. This unit may be split into two subunits based on the abundance of carbonate layers: carbonate phosphorite (A1), below; and marly phosphorite (A2), above. Unit B consists of a 1 m thick marl layer that separates phosphorite Units A and C. The latter package is composed of interbedded phosphorites and carbonates, up to 15 m thick, grading upwards into a coprolite-rich layer below bioturbated carbonates with thin beds of phosphorite and marl (Unit D). A thick (~95 m) succession of nummulitic limestones constitutes the top of the Metlaoui Group in the area (El Garia Formation; Fournié, 1978; Zaïer et al., 1998), below marls of the Middle Eocene Souar Formation.

The Sekarna deposit is located 20 km SW of Maktar (Fig. 2A). The Sekarna phosphorites are more lithologically diverse than others in Tunisia. They are green to brown-grey coloured, lithified, glauconite-rich and locally silicified granular beds, and exhibit distinctive Zn–Pb mineralization in some levels (Garnit et al., 2012b). The Chouabine equivalent in the undivided Metlaoui Group consists of a glauconitic-microconglomeratic phosphorite (5–7 m thick) resting on a thin bed of Paleocene El Haria Formation marl (Fig. 5; locality 2). The phosphorites are overlain by a thick, well-bedded Lower Eocene carbonate succession containing abundant nummulites (Fig. 2C; El Garia Formation equivalent). The Metlaoui Group is overlain by the Middle Eocene Souar Formation.

2.2 Eastern Basins

These basins lie between 34°00' – 36°50'N and 9°15' – 10°10'E. The Eastern Basins are located in the southern region of the North–South Axis (Nord–Sud Axis, Burollet, 1956) structural high, in the Sidi Bouzid–Meknassy–Mezzouna areas (Figs. 1, 3). Here, a number of small basins, developed as couplets or en echelon, parallel the main structural lineament. From north to south, they include the three sub-basins of: (1) Es Souda; (2) Jebs; (3) Oued Abiod, Kef Nsour, Rouijel (Béji-Sassi, 1999). The phosphorites deposited in these basins during the Late Paleocene–Early Eocene show significant lateral and vertical variation and are overlain by, and occur within, a dolostone–evaporite succession that here constitutes the bulk of the Metlaoui Group. It is envisaged that deposition occurred in a series of small embayments bordering Kasserine Island (Fig. 1), that were separated from the open ocean by shallows and inlets (Zaïer et al., 1998). The succession is similar to that developed on the eastern margin of the Gafsa-Metlaoui Basin. To the north, along the eastern margin of Kasserine Island, more open-marine phosphorite and glauconitic facies are developed.

Some levels within Upper Paleocene–Lower Eocene of both the Eastern Basins and the Chouabine Formation in the Gafsa-Metlaoui Basin include a mineral assemblage derived from a calc-alkaline volcanic source, consisting of quartz, clinoptilolite, and feldspar with local concentrations of euhedral ilmenite and zircon (Clocchiatti and Sassi, 1972; Sassi, 1980; Béji-Sassi et al., 1996; Béji-Sassi et al., 2001). The source area of the volcanism is uncertain, but it is believed to have been located either in the eastern part of the Gafsa-Metlaoui Basin or in the Gulf of Gabes, offshore eastern Tunisia (Sassi, 1980; Winnock, 1980). Hyaloclastites are a common feature of wells drilled in Upper Cretaceous sections offshore (Zaïer et al., 1998).

Phosphorites in the Eastern Basins were investigated in Jebel Jebs (Mount Jebs), situated 8 km north of Meknassy, bounded by Oued Leben to the south, Jebel Gouleb to the north, and

Jebel Meloussi to the NW (Fig. 3A). Jebel Jebs is a north–south trending, perched synform with an elliptical shape. Outcrops generally consist of Upper Cretaceous to Eocene strata. Two packages of phosphorite characterise an undivided Metlaoui Group, one at the base, the second in the middle of the succession, sandwiched between thick beds of massive gypsum (Figs. 3, 5; locality 3). The lower phosphorite beds contain three phosphorite levels (I, II, and III in Fig. 5). These beds are separated by clay, gypsum, and dolostone interlayers. The thicknesses of Beds I, II and III are 2.85–17.0, 0.50–2.75, and 3.15–6.0 m, respectively. The upper phosphorite beds include two thick (6–10 m) phosphorites (Fig. 5). The Metlaoui Group is overlain by thick, massive gypsum and/or dolostone beds of the middle to upper Eocene Jebs Formation.

2.3 Gafsa-Metlaoui Basin

The Gafsa-Metlaoui Basin is located in the southern Atlas of central Tunisia, covering an area of approximately 4500 km^2 between 34°00' – 34°45'N and 8°00 – 9°15'E (Figs. 1, 4). Structurally, it is a transitional area between a strongly faulted and folded area to the north, the central-northern Atlasic Domain, and the undeformed Saharan Platform to the south (Zargouni, 1985; Hlaiem et al., 1997; Saïd et al., 2011). The Basin is bounded by the Metlaoui mountain range to the north, including Jebels Bouramli, Ben Younes and Orbata, and by the North Chotts Range to the south (Figs. 1, 4). The sedimentary rocks at outcrop range in age from Cretaceous to Quaternary.

Sedimentation in the Gafsa-Metlaoui Basin occurred in a relatively restricted setting, which fluctuated between littoral and lagoonal conditions, resulting in rhythmic or episodic sedimentation (Garnit et al., 2012a; El Ayachi et al., 2016). As a consequence, there is significant variation in facies within the basin, including phosphorites, porcelanites, cherts, shales, marls, limestones, dolostones, and gypsum. Marly interbeds within the phosphorite succession typically contain from 1–2% up to 7% total organic carbon (TOC). The organic

matter is immature (Tmax < 430°C) and almost entirely of marine planktonic and bacterial origin (e.g. Belayouni and Trichet, 1983; Belayouni, 1984; Trichet et al., 1990; Felhi et al., 2008; Ben Hassen et al., 2009; Tlili et al., 2011). Palynofacies are characterised by abundant organic-walled dinoflagellate cysts and a general absence of terrestrial palynomorphs (Belayouni and Trichet, 1980; Fauconnier and Slansky, 1980; Trichet et al., 1990).

Phosphorite deposits are generally exposed on the flanks of the east–west trending anticlinal structures of Jebels Bliji, Chouabine and Alima (Fig. 4A). The main phosphorite succession constitutes the Chouabine Formation (Burollet, 1956; Fournié, 1978) of the Paleocene–Eocene Metlaoui Group (cf. Moody, 1987). The Group lies above the Maastrichtian–Danian El Haria Formation (green shales interbedded with thin limestone beds), and is overlain by the middle to upper Eocene Jebs Formation (massive bedded gypsum deposits).

The Chouabine Formation generally ranges from 25 to 100 m thick (Sassi, 1974; Chaabani, 1995; Ounis et al., 2008; Kocsis et al., 2013). Ten main phosphorite units (from top to bottom: layers 0–IX) are developed within the Formation, separated by beds of marl, marly limestone and diatom-bearing porcelanite and chert. In the eastern part of the basin the amount of phosphorite decreases and a higher proportion of carbonates and marl occurs (Chaabani, 1995), while to the west biosiliceous sediments (diatom-bearing porcelanite) become more important (Burollet, 1956; Sassi, 1974, 1980; Ahmed et al., 2015). Diatom faunas indicate a warm climate, coastal shallow-marine environment within the central basin, with more brackish eutrophic conditions to the east (Ahmed et al., 2015). Water depths increased for east to west (Ounis, 2011), attaining a maximum water depth of <100 m (cf. Adatte et al., 2002). The phosphorite – organic-rich marl – diatom-bearing porcelanite facies, represents the classic coastal upwelling trinity (McKelvey et al., 1953). The upper part of the Metlaoui Group is represented by oyster-rich limestones with phosphorite intercalations,

known by the miners as the 'phosphate du toit'; these beds constitute the Kef Eddour Formation (Ben Haj Ali et al., 2002). The limestones locally contain abundant nodular chert and are dolomitic towards the eastern and western basin margins.

Phosphorites of the Gafsa-Metlaoui Basin were investigated at five locations (Figs. 4A, 5; localities 4 – 8): Naguess, central Kef Eddour, Table Metlaoui 315, Mzinda, and Jellabia 56. The Mzinda and Jellabia deposits (localities 7, 8) lie to the SE of the other sections, in the NW section of Jebel Sehib. Eight main economic phosphorite beds are exploited in the northern sections, labelled I – VIII in Figure 5, separated by marl intercalations, lumachellic and minor phosphatic layers, and concretionary limestones (Figs. 4B, 5).

The Naguess deposit (locality 4) lies north of Jebel Alima (Figs. 4A, 5). The average total thickness of the phosphorite layers is approximately 11.2 m, with an additional 12.2 m of intercalated units. The central Kef Eddour deposit (locality 5) is located approximately 10 km NNW of Metlaoui (Figs. 4A, B, 5). The average total thickness of the phosphorite beds is 12.3 m, with approximately 12.8 m of intercalated beds. The Table Metlaoui 315 deposit (locality 6) is located on the southern side of the line of hills ranging between Jebel Alima and Jebel Stah (Figs. 4A, 5). The average total thickness of the phosphorite beds is 12.4 m, with 11.3 m of intercalated layers. The average total thickness of phosphorites in the main phosphatic unit in the Mzinda and Jellabia 56 deposits is 7.2 m (Figs. 4A, C, D, 5; localities 7, 8). Here, the uppermost part of the phosphatic sequence (beds 0 and I> in Fig. 5) is a reworked facies that is 8.5 m thick and comprises sandy, coarse-grained, well-sorted, and friable phosphorites.

2.4 Age constraints on phosphorite deposition

Accurate dating of the Chouabine and equivalent phosphorites has proved challenging. The paucity and poor preservation of calcareous fossils, a general absence of biostratigraphically significant taxa, and abundant evidence of sediment reworking and

hiatuses, limit the application of biostratigraphy. Detailed biostratigraphic and chemostratigraphic studies have been undertaken almost exclusively on Gafsa-Metlaoui Basin deposits. More generally, the onset of phosphorite deposition has been considered to represent a base Ypresian marker (Zaïer et al., 1998).

Ben Abdessalem (1978) placed the Paleocene–Eocene boundary at the bottom of Bed II in the Gafsa-Metlaoui succession, based on the occurrence of an organic walled dinoflagellate cyst assemblage dominated by *Apectodinium* spp. in beds 0–I. An *Apectodinium* acme provides a global marker around of the Palaeocene–Eocene boundary (Bujak and Brinkhuis, 1998; Crouch et al., 2001). Chaabani (1995) recorded the planktonic foraminifera *Globorotalia wilcoxensis* Cushman & Ponton in the lower Chouabine Formation, and placed the series boundary in the middle of the marly interval between beds VIII and IX. Bolle et al. (1999) placed the base of the Eocene at the top of the Chouabine Formation in the Gafsa-Metlaoui Basin, based on a tentative assignment of beds 0–II to calcareous nannofossil zone NP9 with records of *Discoaster multiradiatus* Bramlette & Riedel, and a sequence stratigraphic correlation to the Elles section in northern Tunisia.

Most recently, El Ayachi et al. (2016) placed the Paleocene–Eocene boundary in the lower beds of the Chouabine Formation (below the interval studied here) in the Oued Thelja section, based on the two samples that yielded planktonic foraminifera. The occurrence of *Morozovella velascoensis* Cushman in both samples and *M. subbotinae* Renz & Morozova in their higher sample support a latest Paleocene–earliest Eocene age (P5–E2 planktonic foraminifera zones) for the lower phosphorites, but in the absence of other productive samples, it is not possible to place the boundary more precisely.

Ounis et al. (2008) documented a large negative carbon isotope excursion (CIE) of 3–4 ‰ VPDB $\delta^{13}C_{phos}$ centred on beds IV–III of the Chouabine Formation. The excursion was recorded in both coprolites and shark teeth from two sites (Jebels Alima and Bliji), with

minima of -16‰ and -12‰ $\delta^{13}C_{phos}$ in the two different phosphate archives, respectively. Ounis et al. (2008) correlated the $\delta^{13}C$ minimum to the global CIE accompanying the Palaeocene–Eocene transition – the PETM Event (Fig. 5; McInerney and Wing, 2011). However, no coincident negative shift in $\delta^{18}O$ was observed in either the structural carbonate (CO_3^{2-}) or phosphate (PO_4^{3-}) of the apatite, as would be expected to result from the global warming associated with the PETM (Zachos et al., 2001, 2008; McInerney and Wing, 2011). The lack of a coincident $\delta^{18}O$ minimum was attributed to the semi-closed nature of the basin, which prevented the preservation of the global signal. However, a stratigraphically higher negative shift of $\delta^{18}O_{PO4}$, of around 2‰ VSMOW in Bed 0 has been tentatively correlated to the "Early Eocene Climatic Optimum" (EECO, Fig. 5) by Kocsis et al. (2013).

A recent Sr-isotope study (Kocsis et al., 2013) yielded ages consistent with the carbon isotope interpretation of Ounis et al. (2008): layer IX 61.8±2.2 Ma; layers VIII–V 57.2±1.8 Ma; layers IV–0 54.6±1.6 Ma, with the base Eocene currently dated at 56.0 Ma (Vandenberghe et al., 2012). However, the Sr-isotope age model is not unambiguous because some samples showed anomalous values that were attributed to sediment reworking, to variable input of local Sr sources into the restricted basin, or to diagenesis. These samples were excluded from the age determinations.

We follow Ounis et al. (2008) and Kocsis et al. (2013, 2014) in placing the base of the Eocene at the top of Chouabine Formation Bed III in the Gafsa-Metlaoui Basin (Fig. 5).

3. Materials and methods

We collected 58 phosphorite samples from the locations detailed above, and examined standard and polished thin-sections under a light microscope using transmitted and reflected light. Sample positions are indicated in Fig. 5. The bulk mineralogy and clay mineral assemblages were determined by semi-quantitative (±5%) X-ray diffraction. Analyses were

314 performed using a PANalytical X'Pert PRO X-ray diffractometer, and the diffraction data
315 were interpreted using X'Pert HighScore Plus software.

316 Sample preparation and geochemical analyses were performed at Actlabs (Ontario,
317 Canada) using the 4Litho, 4B1 and 4E-INAA analytical packages; further details of the
318 analytical techniques may be found at: http://www.actlabs.com. Samples were split and
319 pulverised in mild steel. Major-elements [SiO_2, TiO_2, Al_2O_3, Fe_2O_3(T), MnO, MgO, CaO,
320 Na_2O, K_2O, P_2O_5] and selected trace-elements (TEs: Ba, Sr, V, Y, Zr) determinations were
321 obtained by inductively coupled plasma – atomic emission spectrometry (ICP-AES) analysis,
322 following fusion of 0.2 g subsamples in graphite crucibles with lithium metaborate and
323 tetraborate flux, the melt being dissolved in 5 % nitric acid. Other TEs (Hf, Mo, Nb, Rb, Th,
324 U), together with the rare-earth elements (REEs: La, Ce, Pr, Nd, Sm, Eu, Gd, Tb, Dy, Ho, Er,
325 Tm, Yb, Lu), were obtained by ICP-mass spectrometry (ICP-MS) analysis of the fusion
326 solutions. Data were supplemented by instrumental neutron activation analysis (INAA) of 30
327 g subsamples for the determination of As, Br, Cr, Sb, Sc, and a mixed acid (HF, $HClO_4$,
328 HNO_3) open-vessel digestion of 0.25 g subsamples and dissolution in HCl, with ICP-AES
329 determination of Cd, Cu, Ni, S and Zn.

330 Detection limits were 0.01% for all major elements except MnO and TiO_2, for which the
331 limits were 0.001%. The detection limits (ppm) for TEs were: Sc, Th, U, 0.1; Hf, Sb, 0.2; As,
332 Br, Cd, 0.5; Cu, Nb, Ni, Zn, 1; Mo, Rb, Sr, Y, 2; Ba, 3; Zr, 4; Cr, V, 5. Detection limits
333 (ppm) for REEs were: La, Ce, Nd, Sm, Gd, Tb, Dy, Ho, Er, Yb, 0.1 ; Pr, Eu, Tm, 0.05; Lu,
334 0.04.

335 Standard reference materials and internal control samples were analyzed with each
336 sample batch to monitor analytical accuracy and precision. Data quality was additionally
337 assessed via replicate analyses performed on four samples. Reference materials measured
338 along with the unknowns of this study consisted of NIST 694 Western Phosphate Rock, NIST

1633b, USGS BIR-1a, DNC-1, W-2a and GBW 07113 for major elements and some trace elements, and GSJ JR-1, NCS DC-86312, DC-70014, DC-70009, OREAS-100a and 101a for TEs and REEs. Analytical data for quality control samples were presented by Garnit (2013, Annexe 1). For the major elements, the mean deviation of the unknowns from the standards was typically better than 5% relative; reproducibility of duplicate analyses was generally within 2% relative. The TEs and REEs were generally accurate to within 10% relative; duplicate analyses show reproducibility within 3% relative.

The trace-element contents of selected sphalerite and pyrite grains were determined by Laser Ablation - Inductively Coupled Plasma - Mass Spectrometry (LA-ICP-MS) using an Elan DRCe (Perkin Elmer/SCIEX) instrument at the Department of Earth Sciences, Università della Calabria, following the method of Garnit et al. (2012a). Analytical accuracy was assessed by the analysis of USGS BCR 2G glass. Accuracy, calculated as the difference from reference values (Gao et al., 2002), was always better than 10%, with most elements having values in the order of 5%.

For statistical investigation**,** we applied two multivariate methods using StatSoft Statistica 7.1 software: principal component analysis (PCA) and hierarchical cluster analysis (HCA). Some individual data points are missing (e.g. SO_3, Cd) or are below the detection limit (e.g. As, Mo, Nb, Sb) for some samples in our geochemistry dataset. These missing data needed to be replaced for multivariate statistical analysis of the full element suite. We replaced the missing data with the mean concentration of the element from all other locations, and we replaced the data below the detection limit with the detection limit itself. This approach is consistent with several previous studies that performed statistical analyses on large geochemical datasets (Meglen, 1992; Yunker et al., 1995, 2005; Güler et al., 2002).

Values of variables in our geochemical dataset commonly differ significantly in magnitude, and may be reported in different units (%, ppm). To ensure that all terms are non-

dimensional and differences in magnitude are minimal, the data must be standardized. Without standardization, more abundant variables are over-represented in the variance of the re-expressed dataset. To accord the same weight to all measurements (as is generally appropriate in geochemical studies), each data point in the original dataset was auto-scaled by subtracting the mean of the variable and dividing by the standard deviation, as follows:

$$Z_i = (X_i - M)/S \qquad \text{(Equation 1)}$$

where X_i is the ith data point for variable i in the raw data set X (Moreda-Pineiro et al., 2001; Davis, 2002). The mean and standard deviation of i are M and S, respectively, and Z_i is the ith data point for variable i in the newly generated data set A, which has a mean of zero and a standard deviation of one unit.

We investigated correlations between the element concentrations using Pearson correlations without any assumptions regarding the distribution of values in the range. For the HCA, we used the Euclidean distance as the distance measure (similarity measurement) between sampling sites, and Ward's method as the linkage rule.

4. Results

4.1 Petrography and mineralogy

The petrography and mineralogy of Tunisian phosphorites have been studied previously by a number of authors (e.g. Sassi, 1974; Chaabani, 1995; Béji-Sassi, 1999; Zaïer, 1999; Felhi et al., 2008; Ben Hassen et al., 2010; Galfati et al., 2010; Ounis, 2011; Garnit et al., 2012a; Galai and Sliman, 2014; Ahmed et al., 2015). Sediments are generally grey-brown coloured, well-rounded, moderately sorted, fine–medium grained phosphate sands with a marly matrix.

Some beds are poorly sorted mixed sands and gravels, others display variable cementation by calcite, more rarely dolomite or silica. Despite some well-defined bedding surfaces, the phosphorites generally display an absence of internal bed structures other than *Thalassinoides* burrows, and are commonly intensely bioturbated.

Petrographic examination shows similarities in the phosphatic constituents (pellets, coprolites, bioclasts including bone and teeth, and phosphatized intraclasts) contained within the different deposits, but distinct variation in the non-phosphatic constituents (quartz, glauconite, lithoclasts, calcitic bioclasts and microcrystalline aggregates of carbonate minerals) was observed. Non-phosphatic constituents in the Gafsa-Metlaoui phosphorites are dominated by calcite, dolomite and silicate minerals (quartz, opal-CT, clinoptilolite and clay minerals). By contrast, the carbonate component in the Eastern Basins at Jebel Jebs is primarily dolomite (Table A1), which occurs mainly as cement. Phosphorites rich in glauconite and quartz (detrital and/or authigenic) are specific to the Sekarna area.

The Tunisian phosphorite ores are composed predominantly of the mineral francolite, a complex carbonate-substituted fluorapatite (McConnell, 1973; McArthur, 1985; Jarvis et al., 1994), while the associated gangue minerals include calcite, dolomite, quartz, diagenetic zeolites (clinoptilolite-heulandite) commonly associated with opal-CT, gypsum (occasionally), and clay minerals (smectite, illite, palygorskite, sepiolite, kaolinite). Accessory minerals (as endogangue and/or exogangue) present in some beds include glauconite at various stages of evolution, sulphides (pyrite, sphalerite), heavy minerals (ilmenite, zircon, apatite, amorphous Ti-Fe oxides), and feldspar (Fig. 6). The mineral association of the phosphorite samples is relatively uniform, although the proportion of mineral phases varies significantly, even within a single deposit.

Clay minerals in the Gafsa-Metlaoui deposits are dominated by smectite (Table A1; 45–100% of the clay mineral assemblage), with subordinate quantities of palygorskite (typically

10–20%), sepiolite (generally 5–20%), and kaolinite (≤10%, in the lowest beds only), as reported previously from the basin (Sassi, 1974; Bolle et al., 1999; Felhi et al., 2008; Tlili et al., 2010, 2011; Ahmed et al., 2015). Neoformed sepiolite appears systematically in association with palygorskite, indicating a genetic link with the latter mineral. Kaolinite is present only at the bottom of the phosphorite succession.

The clay assemblages in the Eastern Basins at Jebel Jebs yield even higher proportions of smectite (100% in several upper phosphorite beds), with minor amounts of palygorskite and kaolinite (~15% each) present in the lowest phosphorite beds (Table A1); illite (up to 30%) is present in the uppermost phosphorites. In the Northern Basins at Sra Ouertane, smectite (60–100%), kaolinite (0–20%) and illite (0–30 %) constitute the clay mineral assemblages, kaolinite giving way to illite as the subordinate clay mineral up section. Kaolinite (64–85%), illite (0–36%), and minor amounts of smectite are found in the Sekarna deposit.

Sulphides are mostly recognized in the heavy mineral fraction of fresh samples from the Gafsa-Metlaoui Basin. The main sulphide minerals are pyrite and sphalerite. Both minerals occur as dispersed free crystals, intergranular cement, micrometric inclusions in phosphatic particles, and/or as foraminifera test infillings. The heavy minerals apatite, zircon and Fe-Ti oxides (ilmenite, rutile) occur as accessory phases in Tunisian phosphorites, and are most prominent in samples from the Northern and Eastern Basins. Grain sizes are principally of silt to very fine sand grade, and do not exceed 100 µm. Zircon crystals are almost always prismatic with elongated (100) faces; no signs of reworking or inclusions were observed.

Ilmenite occurs as tabular crystals containing fine ~20 µm inclusions of apatite and shows chemical zonation. Fe-Ti oxides generally show heterogeneous chemical compositions suggesting a complex intergrowth of Fe-Ti minerals. However, apatite inclusions in ilmenite could result from early syn-crystallization in an alkaline magma. Zircon, ilmenite, and rutile likely were derived from acid igneous rocks, and the occurrence of fresh magmatic minerals

in the phosphorites indicates that magmatic rocks played a role in the provenance of the siliciclastic fraction during the formation of the phosphate-bearing units.

The presence of igneous minerals in the phosphorites has been linked to contemporary late Paleocene–Eocene calc-alkaline volcanism (Clocchiatti and Sassi, 1972; Béji-Sassi et al., 1996, 2001).

4.2 Geochemistry

Phosphorites are recognised as being enriched in many trace elements (TE) and rare-earth elements and yttrium (REY) compared to shale and other sedimentary rocks (Gulbrandsen, 1966; Altschuler, 1980; Prévôt, 1990; Jarvis et al., 1994). Results of the major element, TE, and REY analyses obtained in the present study are presented in Table 1. Samples are listed sequentially from stratigraphically highest (youngest) to lowest (oldest) in each deposit.

4.2.1 Major elements

Major oxides in the phosphorite samples are dominated by CaO, P_2O_5, and SiO_2; Al_2O_3, MgO, Na_2O, and SO_3 are the next most abundant elements, while the concentration of all other oxides [Fe_2O_3(T), MnO, K_2O, TiO_2] is generally low (<1%). The major-element composition reflects the dominance of francolite, a carbonate fluorapatite with >1% fluorine and appreciable amounts of CO_2 (Sandell et al., 1939; McConnell, 1973), as the primary mineral in the phosphorites, together with subordinate calcite, dolomite, quartz, opal-CT, feldspar and clay minerals (Fig. 6).

The highest P_2O_5 values (up to 30%) are recorded in samples from Gafsa-Metlaoui Basin (Table 1, Fig. 6A). Taking an average P_2O_5 content of 34.7% for francolite in commercial Tunisian phosphate rock (McClellan, 1980), yields an average francolite content of 75% (maximum 87%) for the Gafsa-Metlaoui Basin sediments, 52% for the Eastern Basins

460 (maximum 85%), and 39% for the Northern Basins (maximum 75%). Similar francolite
461 values were obtained by semi-quantitative x-ray diffraction analysis (Table A1).

462 MgO contents range from 0.23–12.6%, compared to a maximum Mg concentration in
463 sedimentary francolite of 0.36 ± 0.03% (McArthur, 1985; Jarvis et al., 1994). Samples from
464 Sra Ouertane and Jebel Jebs are characterized by the highest CaO and MgO contents,
465 respectively (Table 1, Fig. 6B), reflecting high proportions of calcite and dolomite in these
466 deposits.

467 SiO_2 and Al_2O_3 concentrations show significant variation (2.64–35.6%, 0.43–3.67%,
468 respectively), that reflects the changing proportions of quartz (detrital and from biogenic
469 sources), opal-CT (a product of biogenic opal, principally diatoms, diagenesis), and mixed
470 clay mineral assemblages in the deposits (Fig. 6D). TiO_2 values vary between 0.02–0.17%,
471 and are considered to principally represent clay minerals, as this element shows a strong
472 positive correlation with Al_2O_3 (r = 0.88). However, the highest TiO_2 values (0.16%, 0.17%)
473 were recorded in two ilmenite-rich samples from Sra Ouertane, indicating heavy mineral
474 enrichment associated with an enhanced siliciclastic fraction (potentially of volcanogenic
475 origin). This inference is supported by the strong correlation between TiO_2 and Zr (r = 0.77).

476 The alkali components Na_2O and K_2O show some variability (0.13–1.72% and 0.06–
477 1.47%, respectively). At these concentrations, they can be considered to reflect Na
478 substitution in francolite (maximum 1.2 ± 0.2% Na; McArthur, 1985; Jarvis et al., 1994),
479 combined with variable clinoptilolite, smectite and/or feldspar contents. K_2O content is
480 primarily determined by the type and amount of smectite–illite, glauconite and K-feldspar in
481 the assemblage (Fig. 6D). Fe_2O_3 contents range from 0.16–2.17%, and show a high
482 correlation with MnO (r = 0.85), indicating an association with ferromanganese-
483 oxyhydroxides. Predictably, the glauconite-rich phosphorites of Sekarna have the highest
484 average Fe_2O_3 and K_2O contents (Fig. 6D).

The SO_3 content ranges from 0.20–6.84%. This wide range of SO_3 contents in the samples is attributable to the occurrence of sulphate as a constituent element in the phosphate lattice (maximum 2.7 ± 0.3% SO_4; McArthur, 1985; Jarvis et al., 1994), and the presence of sulphides (pyrite, sphalerite) and gypsum. The lowest SO_3 values are recorded in the samples from Sra Ouertane, Sekarna, and reworked phosphorite layer 0 at Mzinda and Jellabia (Fig. 6C). This is consistent with sediment reworking and weathering having led to sulphur depletion via sulphide oxidation and/or the loss of sulphate from the francolite structure (McArthur, 1978).

4.2.2 Trace elements

Across all samples, the mean abundance (ppm) of TEs (Table 1), in decreasing order is: Sr (1550), Cr (226), Zn (212), V (79), Ba (45), Zr (43), Cd (35), U (33), Ni (22), Br (13), Cu (12), Th (8.2), As (8.1), Mo (7.3), Rb (5.7), Sc (3.9), Nb (2.5), Sb (1.1), and Hf (0.65). These concentrations highlight the high level of Sr (>1000 ppm), an element that readily substitutes for Ca in francolite (Jarvis et al., 1994), followed by three groups of elements that we have classified according to their concentrations. The first group consists of Cr and Zn, with relatively high concentrations (~200 ppm). The second group contains TEs with moderate concentrations (10–100 ppm): V, Ba, Zr, Cd, U, Ni, Br, and Cu. The third group consists of TEs with relatively low concentrations (<10 ppm): Th, As, Mo, Rb, Sc, Nb, Sb and Hf.

Normalised trace-element patterns

Trace-element concentrations normalised to average shale are plotted in Fig. 7. Patterns similar to that of average phosphorite (yellow stars in Fig. 7; Altschuler, 1980) are apparent for all samples, but with subtle regional differences. Northern Basins samples, particularly those from Sra Ouertane (Fig. 7A), have values closest to average phosphorite, with clear enrichment in Cr, Sr, Y, U, Mo, Zn and Cd. Notable depletion occurs in Rb, Ba, Ni and Cu relative to both average shale and average phosphorite. The highest As and Sb concentrations

occur in phosphorites from Sekarna, attributable to the high glauconite content of the sediments (Dooley, 2001; Barringer et al., 2011) and local Zn-Pb mineralisation (Garnit et al., 2012b). High Th values characterise samples from the lower phosphorite beds of Jebel Jebs (Fig. 7B, C).

Aside from the reworked phosphorites (level 0 in the Jellabia and Mzinda deposits; Figs. 5, 7, Table 1), the Gafsa-Metlaoui samples have homogeneous TE levels. Of particular note are Cr, Sr, Zn, Cd enrichment, and Sc, Y, Zr, Ba, U, Cu, As depletion, relative to average phosphorite (Altschuler, 1980). In comparison, the reworked phosphorites have higher concentrations of Zr, Rb, Nb, V, Ba, Ni, Hf, and lower concentrations of U, Y, Cr, Sr, Zn, Cd than the primary beds. Phosphorites from Sekarna and Sra Ouertane contain higher concentrations of Sc, V, Ba, Ni, Cu, U, and lower concentrations of Sr, Zn and Cd than those from Gafa-Metlaoui (Table 1).

Cadmium concentrations in Tunisian phosphorites are variable, but particularly in some Gafsa-Metlaoui Basin samples, they are anomalously high (Table 1, Fig. 7; maximum 172 ppm, >100x average shale), as documented previously by Lin and Schorr (1997) and Béji-Sassi and Sassi (1999). Cadmium exhibits the highest level of enrichment of any element in average phosphorite compared to average shale (18 ppm vs. 0.13 ppm, respectively; Altschuler, 1980; Wedepohl, 1991; see also Bech et al., 2010). Cadmium commonly shows a close association with Zn in phosphorites with high Cd concentrations, where it is attributed to partitioning by sphalerite (Nathan et al., 1996, 1997). Our Metlaoui samples show a highly significant near-linear correlation between Cd and Zn (r = 0.97), but no significant correlation between Cd or Zn and P (r = 0.32 and 0.40, respectively).

Trace-element geochemistry of sulphides

Sulphide minerals occur in fresh samples as discrete grains, foraminifera chamber infills and as micro-inclusions in phosphatic particles. Sulphide formation occurred during early

diagenesis (Berner, 1984; Raiswell and Canfield, 1998; Schoonen, 2004); the source of H_2S for pyrite and sphalerite formation is attributed to bacterial sulphate reduction of organic matter, with iron and zinc being supplied principally via iron oxyhydroxides and organic matter forming the gangue.

Tables 2 and 3 show the trace-element contents of selected sphalerite and pyrite grains determined by LA-ICP-MS. Trace elements detected in sphalerite were Ag, As, Cd, Cr, Cu, Fe, Mn, Mo, Ni, Pb, Sb, Sn, Ti and V (Table 2). Their concentrations are extremely variable but cadmium is a major constituent, contents ranging from 0.8–6.5 %. Béji-Sassi and Sassi (1999) have previously described Metlaoui-Gafsa Basin sphalerites containing 2.8–5.8 % Cd (up to 11.6 mol.% CdS). Copper and Fe show large variation in sphalerite, from 5–232 ppm and from 93–1100 ppm, respectively, and are heterogeneously distributed. Trace-element behaviour in sphalerite is mainly controlled by Zn structural substitutions ($Zn^{2+} \leftrightarrow Cd^{2+}$, Co^{2+}, Fe^{2+}, Mn^{2+}, or $Zn^{2+} \leftrightarrow Cu^{2+}+In^{3+}$; Johan, 1988; Kieft and Damman, 1990; Pattrick et al., 1993), since sulphur does not show significant deviation from the stoichiometric value (32.9%).

Iron and S contents in pyrite vary from 45 to 46% and from 54 to 55%, respectively. This composition is close to stoichiometric pyrite (Fe 46.55%, S 53.45%), indicating few substitutions in the pyrite structure. Cadmium contents are low, averaging 5 ppm; arsenic is the highest abundance trace element (253–704 ppm), Cu and Mo contents vary from 0.1–5 ppm and from 39–149 ppm, respectively (Table 3).

4.2.3 Rare-earth elements and yttrium

Rare-earth element and yttrium (REY) concentrations (ppm) and elemental ratios are presented in Table 1. Total REE (ΣREE) and Y contents show considerable variation, ranging from 110–1020 and 51–402 ppm, respectively. Samples from Sekarna (ΣREE range 598–800 ppm, average 716 ppm) and Jebel Jebs (227–1020 ppm, average 577 ppm) have

higher REE contents than the Gafsa-Metlaoui (151–549 ppm, average 322 ppm) and Sra Ouertane phosphorites (111–690 ppm, average 306 ppm), despite comparable P_2O_5 contents in the Gafsa-Metlaoui samples (Fig. 8). The lowest ΣREE concentrations, recorded at Sra Ouertane, occur in phosphate-poor levels (P_2O_5 < 5%), but no consistent relationship between ΣREE and P_2O_5 is evident: ΣREE show a positive correlation with P_2O_5 for Jebel Jebs (r = 0.97), Sra Ouertane (r = 0.79), and Sekarna (r = 0.59) samples, but no correlation was observed for the Gafsa-Metlaoui data (r = 0.05). Phosphorites from the bases of the phosphorite successions in the Northern and Eastern Basins contain the highest REY contents (Fig. 8).

Post-Archean Average Shale (PAAS; McLennan, 1989) normalized REY patterns of the Metlaoui phosphorites are plotted in Fig. 9. The REY patterns of phosphorites in this study can be divided into three groups: Group I, characterized by slight enrichment of heavy REE (HREE; Ho–Lu) with moderate negative Ce anomalies (Gafsa-Metlaoui Basin samples); Group II (more shale-like), characterized by moderate enrichment of middle REE (MREE; Eu–Dy) and small to moderate negative Ce anomalies (Jebel Jebs, Sekarna); and Group III (seawater-like), characterized by slight enrichment of HREE and depletion in the light REE (LREE; La–Sm) with the largest negative Ce anomalies (Sra Ouertane). Similar patterns are seen in the majority of Late Cretaceous to modern phosphorites (e.g. Jarvis et al., 1994; Emsbo et al., 2015).

A significant negative Ce anomaly in the shale-normalised REY patterns is a feature in all Metlaoui Group phosphorite samples (Fig. 9, Table 1). The anomaly [quantified as $Ce/Ce^* = 3Ce_N/(2La_N+Nd_N)$, where N are PAAS shale-normalised values] is most pronounced (i.e. lowest Ce/Ce* values) for the Sra Ouertane (0.45) and Sekarna (0.51) deposits (Fig. 9; see Section 5.3.2 Fig. 14A for a plot of anomaly values). At Jebel Jebs, the average anomaly (0.70) is comparable to that for the Gafsa-Metlaoui sections (0.69).

Individual phosphorite beds in the Gafsa-Metlaoui Basin (Fig. 5) have distinct REY signatures (Fig. 9), and consistent stratigraphic trends are apparent in all 5 sections; from bottom to top each succession displays: (1) rising ∑REE contents; (2) progressively less negative Ce and falling Y anomalies [$Y/Y^* = 2Y_N/(Dy_N+Ho_N)$]); (3) progressive flattening of the shale-normalised REY patterns, driven by proportionally greater increases in the lighter REEs. These trends do not correspond to stratigraphic variation in P_2O_5, or other major constituents (Table 1).

4.3 Element-mineral associations: Pearson correlation coefficients

Although the element–mineral associations vary from phosphorite-rich to phosphorite-poor levels, correlation analysis can demonstrate general trends. We calculated Pearson correlation coefficients (*r*) for all possible pairs of variables to establish the existence of any correlations. A summary of this analysis is presented in Table 4. The terms "high", "medium", and "low" as applied to factor loadings refer to absolute loading values of >0.75, 0.50–0.75, and 0.36–0.50, respectively. Values lower than 0.36 were not considered to be significant. A significant positive correlation coefficient suggests a similarity in the geochemical behaviour and/or a common source material for these elements; negative coefficients reflect antithetic behaviours and/or mineral associations.

4.3.1 Major elements

For major elements, high positive correlations were found between the following pairs of constituents: Al_2O_3–TiO_2; Fe_2O_3–MnO; P_2O_5–Na_2O; Na_2O–SO_3; K_2O–TiO_2. Three groups of oxides are identifiable in the correlation matrix of Table 2. The first, called the "siliciclastic" group, contains the oxides of Si, Ti, Al, Mg and K, which are major constituents of the aluminosilicate minerals that constitute the terrigenous clastic fraction. The second, called the "authigenic" group, contains P, Ca, and Na. Phosphorus correlates positively with Ca and Na

609 due to the presence of these elements in the apatite lattice (McConnell, 1973; McClellan,
610 1980; Nathan, 1984; Jarvis et al., 1994), although these elements may also be linked to
611 carbonate (calcite, dolomite) and silicate minerals (clinoptilolite, smectite), respectively.
612 Phosphorus and Si are moderately negatively correlated, showing an antithetic relationship
613 due to quartz, opal-CT and silicate mineral dilution of total phosphate contents (Fig. 6A).

614 Our analytical protocol did not distinguish between sulphate, sulphide and organic
615 sulphur; the sulphur content of the humic acids in the Metlaoui-Gafsa Basin phosphorites is
616 up to 12% (Belayouni, 1984). However, S and P show a weak correlation, consistent with
617 SO_4 substitution in francolite (maximum 2.7 ± 0.3%; McArthur, 1985; Jarvis et al., 1994) and
618 their co-occurrence in organic matter, together with associated diagenetic pyrite and/or
619 sphalerite. Iron is strongly correlated only to Mn, representing a third "oxyhydroxide" group,
620 although the presence of glauconite in the sediments points to an additional mineralogical
621 control.

622 *4.3.2 Trace elements*

623 Among the TEs, there are both strong positive and negative correlations. Strong positive
624 correlations were found between the following pairs: Sc–Y, Zr–Nb, Zr–Hf, Nb–Hf, Ni–As,
625 Zn–Cd, and As–Sb. Scandium, Y and the REEs belong to the same group of the periodic
626 table (IIIB), owing to similarities in their atomic structures; the closest similarity exists
627 between Y and Ho (Bau and Dulski, 1999). Consequently, members of the group behave in a
628 very similar manner during geological processes. They readily substitute in the francolite
629 structure (Jarvis et al., 1994). Despite this, they show no significant correlation with P_2O_5
630 (Table 4, Fig. 8), indicating that other factors control elemental concentrations in this case.
631 By contrast, Sr shows a highly significant positive linear correlation with P_2O_5 (r = 0.90),
632 reflecting high levels of substitution in francolite (maximum 0.25 ± 0.02%; McArthur, 1985;

633 Jarvis et al., 1994) and low concentrations in other Sr-bearing minerals (e.g. carbonates,
634 feldspar), and a clear association with the authigenic group.

635 Zirconium, Nb, and Hf are attributed to the siliciclastic group, as indicated by strong
636 positive correlations between Zr and TiO_2 (r = 0.77), Hf and TiO_2 (r = 0.81), and Nb and TiO_2
637 (r = 0.91). These high field strength, incompatible elements are strongly enriched in common
638 heavy minerals such as ilmenite, rutile, titanite, titanomagnetite and zircon. In the Gafsa-
639 Metlaoui Basin, the increased abundance of TiO_2, Al_2O_3, Hf, Nb and Zr in the reworked
640 phosphorites is consistent with the inclusion of increased amounts of detrital minerals in these
641 beds.

642 Elevated Cd and Zn contents, a positive correlation between these chalcophile elements,
643 and an absence of any significant correlation with P_2O_5, have been observed in many
644 phosphorites (e.g. Nathan et al., 1996, 1997; Béji-Sassi and Sassi, 1999; Soudry and Nathan,
645 2001). Other sedimentary phosphorites contain low Zn concentrations and variable moderate
646 enrichment in Cd relative to shales (Baturin, 2006). Similarly, the high Cd and Zn values
647 recorded here in the Metlaoui phosphorites, show a poor correlation with P_2O_5 (r = 0.32 and
648 0.40, respectively). Originally bound in organic matter complexes, bivalent Cd and Zn are
649 concentrated in sulphides (principally sphalerite) during early diagenesis, and are associated
650 with phosphorites deposited in poorly oxygenated environments (Nathan et al., 1997);
651 Metlaoui Group sphalerites contain up to 6.5 wt% Cd (Table 2).

652 The correlation coefficients for As, Ni and Sb are highest for Fe and Mn, indicating an
653 association principally with the oxyhydroxide and glauconite group. This is consistent with
654 the high levels of enrichment in As, Ni and Sb that characterise Fe-Mn crusts more generally
655 (Hein et al., 2003; Hein and Koschinsky, 2014), although these elements occur at elevated
656 concentrations, along with Cr, Rb and V, in glauconite (e.g. Barringer et al., 2011; Smaill,
657 2015).

4.4 Principal Component Analysis

Principal Component Analysis (PCA) was employed to investigate TE and REY affinities and sources based on relationships among variables, and to explore similarities among geochemical samples and deposits. From the standardized geochemical dataset, principal components were extracted from the symmetrical correlation matrix computed for the 45 variables. The number of components was based on the Kaiser criterion (Kaiser, 1960), for which only components with eigenvalues greater than 1 are retained.

Table 5 presents the four principal components, as well as the variance that they each account for. The first four components extracted have eigenvalues greater than 1, and account for 76.7% of the total variance in the dataset. Each component is characterized by a few high loadings and many near-zero loadings. The first two components explain 38.8% and 24.3% of the variance, respectively, and thus account for the majority of the variance in the original dataset. Components 3 and 4 are less important; they account for approximately 8% and 5% of variance, respectively.

Component 1 explains the greatest amount of the variance, and is characterized by very high negative loadings in the REE and Y (Table 5). This component is considered to be a REY factor. The very high loading values demonstrate how these elements are a major factor defining geochemical variation in phosphorites, which occurs as REY substitute for Ca in francolite. Crystallographic parameters, the seawater source, depositional environment and diagenesis play important roles in controlling the abundance of these elements. Moderate negative loadings for Fe_2O_3(T), MnO, and a broad range of trace metals (As, Cr, Cu, Mo. Ni, Sb, Sc, Th, U, V) demonstrate a link between REY contents, palaeoproductivity and redox (see Discussion, below).

Component 2 is characterized by highly positive loadings in Al_2O_3, K_2O, TiO_2, Zr, Rb, Nb and Hf (Table 5) and high negative loadings for CaO, Na_2O, P_2O_5 and Sr. This

component is related to clays and heavy minerals; therefore, it is considered to be a detrital mineral factor. It reflects how the proportion of siliciclastic minerals vs. phosphate (i.e. lithology) controls the bulk geochemistry of the phosphorites. It will reflect detrital input and proximity to land, and changes in these in response to tectonics, climate and sea-level change.

Figure 10 summarizes this information, showing the position of the loadings in the plane defined by the axes of components 1 and 2. The negative PC1 – positive PC2 quadrant contains Fe_2O_3(T) and MnO, as well as TEs typically contained within Fe-Mn oxyhydroxides and glauconite, such as Cu, Sb, As, Ni, Mo, V and Cu (Fig. 10A). A phosphate association of P_2O_5, CaO, Na_2O, SO_3 and Sr are located together on the negative PC2 axis, but are regarded as occurring within an extended array with other TEs and REY elements typically contained within francolite, such as Cr, U, Th, Sc (Fig. 10A). This analysis reveals information about the relationship among other elements. For example, the proximity of Cd and Zn to SO_3 reflects the geochemical link to sphalerite that has been shown to enhance the Cd content of the phosphorites. On the positive PC2 axis, SiO_2, TiO_2, Al_2O_3 MgO, K_2O are grouped with Ba, Hf, Nb, Rb and Zr, reflecting the silicate and heavy mineral detrital association.

The REEs, Y and Sc exist as a distinct group within the negative PC1 axis and near zero on the PC2 axis (Fig. 10A). These elements demonstrate variable modes and levels of incorporation, with relationships to both apatite and/or Fe-Mn oxyhydroxides. This is consistent with models suggesting that Fe-oxyhydroxides provide the main scavenging and carrier phase for transfer of REEs, Y and Sc from seawater to sediment, with incorporation of those elements into francolite from porewater following iron reduction close to the sediment/water interface (Jarvis et al., 1994 fig. 3).

Components 3 and 4 each account for <10% of the variance (Table 5). Large positive scores for the two main productivity proxies Cu and Ni and negative scores for Ce and Th point to Component 3 being a productivity factor. Component 4 has the highest positive

values for Fe_2O_3(T), MnO, As, Mo, Sb and V, indicating the further influence of Fe-Mn oxyhydroxides and glauconite on the bulk chemistry.

Plotting individual samples within variable space (Fig. 10B) demonstrates strong associations between samples form individual localities. The majority of Gafsa-Metlaoui Basin samples form a tight cluster with low positive values for PC1 and low negative values of PC2. Jebel Jebs and Sra Ouertane samples define a scattered cluster along with reworked phosphorites from the Gafsa-Metlaoui Basin that has positive values for both factors, related to an increased proportion of detrital minerals effecting bulk chemistry. A second small cluster of samples from these localities in the negative sector for both factors is ascribed to francolite-associated trace-element variation. The three samples from Sekarna are the only ones to plot in the upper left quadrant, with highly negative values for PC1 and positive values for PC2 (Fig. 10B), related to the unique glauconite and Fe-Mn oxyhydroxide enrichment at this locality (Table 1).

4.5 Hierarchical Cluster Analysis

The sample groups identified by the PCA are consistent with results of the hierarchical cluster analysis (Fig. 11). The HCA provides further evidence that the trace and REE concentrations offer a valid methodology for distinguishing facies associations of phosphorites. The first cluster, representing approximately 14% of the assemblage, comprises basal phosphorite samples from the Northern and Eastern Basin samples that were previously differentiated by having low negative PCA Factor 1 scores (Fig. 10B), and is distinguished by high REE, Th, Sc, Sb, As, Ni, V, Mo, and Cu contents. The second group includes the majority of samples, all from the Gafsa-Metlaoui Basin, and accounts for 59% of the assemblage. It represents carbonate fluorapatite-rich phosphorites with notably high Sr, Cr, Zn and U contents. The third cluster comprises the remaining Northern and Eastern Basins samples and reworked phosphorites from Gafsa-Metlaoui, incorporates 27% of samples in the

733 study, and is characterized by high Ba, Rb, Hf, Zr, and Nd contents, which relate to an
734 increased abundance of detrital silicates and heavy minerals.

735 **5. Discussion**

736 *5.1 Late Paleocene–Early Eocene climate*

737 An arid warm climate in the region of central and northern Tunisia during the Late
738 Paleocene–Early Eocene is indicated by: (1) an association of Metlaoui phosphorites with
739 sabkha-facies evaporites (e.g. Moody and Grant, 1989; Messadi et al., 2016); (2) an absence
740 of significant detrital input despite close proximity to emergent landmasses (Kasserine and
741 Djeffara islands; Fig. 1); (3) marine diatom assemblages (Ahmed et al., 2015); and (4) a very
742 low proportion of terrestrial palynomorphs (pollen and spores) in the sediment organic
743 fraction (Belayouni and Trichet, 1980; Fauconnier and Slansky, 1980; Trichet et al., 1990).

744 *5.1.1 Clay mineral assemblages as climate proxies*

745 The clay mineral assemblages in the Metlaoui phosphorites provide further evidence of
746 the prevailing climate in Tunisia during the Paleocene–Eocene transition. Clay mineral
747 assemblages are generally dominated by smectite, but with high proportions of palygorskite
748 and sepiolite in the Gafsa-Metaloui Basin (Table A1). Excluding hydrothermal sources,
749 palygorskite typically forms in warm arid coastal and peri-marine environments. Here,
750 continental alkaline waters are concentrated by evaporation, leading to porewaters enriched in
751 Si and Mg that favour the formation of authigenic palygorskite and/or smectite (Bolle et al.,
752 1999; Bolle and Adatte, 2001). Palygorskite and, to a lesser extent, sepiolite are also found in
753 calcrete soils of arid to semi-arid climate zones (Millot, 1970; Robert and Chamley, 1991).

754 The geography of the Gafsa-Metlaoui Basin, situated between two emerged land areas,
755 would have been favourable to the neoformation of palygorskite and sepiolite under an arid to

semi-arid climate. By contrast, older Paleocene sediments in the basin contain high kaolinite/smectite ratios, indicative of a warm and humid climate with high rainfall (Chamley, 1989; Robert and Chamley, 1991). The disappearance of kaolinite, coincident with a gradual increase in smectite, palygorskite and sepiolite, as well as illite and chlorite, suggests the progressive development of seasonal and then increasingly arid climate in the coastal environments of SE Tethys and on the Saharan Platform during the latest Paleocene (Bolle et al., 1999), and the onset of major phosphorite deposition.

Palygorskite occurs only as an accessory phase on the oldest Eastern Basin phosphorites and is not observed in the Northern Basins (Table A1). Here, the abundance of smectite and the generally low kaolinite content suggest wetter seasonal climate conditions in ocean-facing settings. An exception to the general trends is observed at Sekarna where the phosphorites are kaolinite and illite dominated, confirming the results of Zaïer (1999) who reported kaolinite-illite assemblages in several Northern Basins deposits close to Kasserine Island (Sekarna, Kalaat Khasba, Ain El Karma, El Guessaat).

5.1.2 Oxygen isotopes

A stable warm climate during Metlaoui phosphorite deposition is further indicated by the oxygen isotope composition of structural phosphate in coprolites and shark teeth (Ounis et al., 2008; Kocsis et al., 2013). However, calculated surface water temperatures of around 20°C based on these data are likely underestimates; climate models suggest values of >27°C for Tunisia during the Paleocene–Eocene (Dunkley Jones et al., 2013). This underestimation may be ascribed to increased salinity and ^{18}O enrichment of a restricted water mass in the evaporative Gafsa-Metlaoui Basin (Ounis et al., 2008; Kocsis et al., 2014). If a higher isotopic value of 0 ‰ $\delta^{18}O$ is assumed for the basin water, rather than the estimated -1‰ of average open-ocean greenhouse-climate water (Shackleton and Kennett, 1975), then more acceptable temperatures may be calculated (Kocsis et al., 2013).

781 *5.1.3 Late Paleocene – Early Eocene climate change*

782 Earth surface temperatures increased by about 5°C from the late Paleocene through the
783 early Eocene, culminating in the "Early Eocene Climatic Optimum" at around 52–50 Ma, the
784 warmest episode of Cenozoic time (Zachos et al., 2001, 2008). Superimposed on this long-
785 term gradual warming, the PETM "hyperthermal" occurred during the earliest Eocene, a
786 short-lived (<200 kyr) event characterized by rapid global warming, major changes in the
787 environment, and massive isotopically light carbon addition (Zachos et al., 2008). The
788 current consensus is that the PETM immediately followed the Paleocene–Eocene boundary at
789 56.0 Ma (e.g. Sluijs et al., 2008, 2014; Vandenberghe et al., 2012).

790 An influx of kaolinite indicating a temporary episode of warming and increased humidity
791 during the PETM has been documented widely in the Tethyan region, but is absent from
792 restricted marginal areas, like the Gafsa-Metlaoui Basin, where aridity persisted (e.g. Dunkley
793 Jones et al., 2013; Kiehl and Shields, 2013). It is possible that the anomalous clay mineral
794 assemblage of the Sekarna and other Northern Basins phosphorites represents this event, or
795 the deposits may be of older Paleocene age. Biostratigraphic control is currently inadequate
796 to differentiate between these alternatives.

797 *5.2 Trace element geochemistry*

798 Interpretation of TE patterns in phosphorites is not straightforward. Trace-element
799 concentrations and ratios in shales have been shown to provide proxies for detrital input flux,
800 palaeoproductivity, and both water column and sediment palaeoredox conditions (Brumsack,
801 2006; Tribovillard et al., 2006; Little et al., 2015; Sweere et al., 2016). However, in
802 phosphorites, elemental concentrations result from a combination of the palaeoenvironmental
803 conditions that control the concentration and availability of specific elements in seawater,
804 sediment and porewater, and the kinetics, thermodynamics and distribution coefficients

controlling element uptake by phosphate minerals during phosphatisation, itself a complex multistage process likely involving a precursor mineral phase to francolite (Jarvis et al., 1994).

5.2.1 Substitutions in the apatite structure

Numerous substitutions occur in all of the apatite sites (the two Ca sites, the PO_4 sites and the F site), and not all of them have the same valency as the original ion (Jarvis et al., 1994). Francolite (a carbonate hydroxylfluorapatite B-type with Ca/P ratio >1.67 according to Kostova et al., 2013) is the common phosphate mineral in Tunisian phosphorites. Mineralogical and chemical studies of purified phosphatic particles have enabled empirical structural formulae to be established for the three basins (Ounis, 2011; Table 6). Ounis (2011), using XRD and the equation of Schuffert et al. (1990), noted slight but significant differences in the CO_3^{2-} substitution in apatite from the different basins: samples from the Gafsa-Metlaoui Basin have higher CO_3^{2-} substitution (8%) compared to those from the Eastern Basins (7%) and Northern Basins (6%, Sra Ouertane). The more highly substituted apatites from the Gafsa-Metlaoui deposits, in particular, have potential to accommodate many ionic substitutions (McConnell, 1973; Altschuler, 1980; Jarvis et al., 1994; Hughes and Rakovan, 2015).

The comparative concentration of each element relative to average shale (Fig. 7) provides some insight into the selectivity of phosphorites as sinks for trace elements that commonly substitute in apatite. However, the higher levels of trace elements are not necessarily located within the apatite lattice itself, but may be adsorbed onto crystal surfaces, may be associated with minerals such as silicates, oxyhydroxides and sulphides, or occur in organic matter (Jarvis et al., 1994; see discussion, below). Trace-element contents are, therefore, a combined product of depositional environment, diagenetic processes, and mineralogical controls.

5.2.2 Comparison of TE and REY distributions in phosphate grains and bulk sediments

The present study reports results obtained from bulk rock analyses. Garnit et al. (2012a) previously published TE and REY data obtained from individual phosphate grains (pellets and coprolites) using LA-ICP-MS, collected from the Sra Ouertane, Jebel Jebs and Gafsa-Metlaoui Basin sections. The elemental concentrations and distribution patterns obtained are essentially identical to those obtained for the same elements (As, Ba, Cd, Cr, Cu, Mo, Ni, Sr, U, V, Zn, REY) in the present study from the bulk sediments (Figs. 7, 9). Ounis et al. (2008) reported similar REE patterns based on LA-ICP-MS spot analyses of coprolites and shark teeth from the Gafsa-Metlaoui Basin. This demonstrates that the TE and REY bulk chemistry of the phosphorites is dominated by the composition of the phosphate grains, and is little affected by the enclosing siliciclastic and carbonate matrices. However, this does not mean that the reported TE and REY contents in either phosphorite study reflect solely francolite compositions. The LA-ICP-MS analyses employed a 50 μm spot size which sampled a complex nanostructure incorporating both apatite crystals and, particularly in the case of pellets, siliciclastic mud and secondary dolomite and sphalerite inclusions. Nonetheless, it confirms the overwhelming influence of francolite on both grain and phosphorite bulk sediment chemistry.

Individual phosphatic particles from the Sra Ouertane showed the highest contents of Ba, Cu, Ni and U, whereas phosphatic particles from the Jebel Jebs and Gafsa-Metlaoui contained the highest Cd, Mo, Sr and Zn contents (Garnit et al., 2012a). Similar trends are seen in the bulk sediment data (Table 1), although in this case individual Sra Ouertane bulk sediment samples exhibit a very wide range of TE concentrations, ranging from the highest to the lowest values in the overall sample set (Fig. 7). This reflects the more diverse lithofacies present in this section and the varying phosphate contents (4 – 26 % P_2O_5; Table 1). Elsewhere in the Northern Basins, the Sekarna section, which was not studied by Garnit et al. (2012a), displays the highest average values of Ba, Cu, Fe, Ni, Mo, U and V.

5.2.3 Palaeoenvironmental proxies

Trace element and REY abundances in the phosphorites of the Metlaoui Group reveal the extent of mineralogical and geochemical variation between different beds, sections, and basins, despite the relatively consistent processes of mineral paragenesis. Except for Cd, Cr, Mo, Sr, U, Zn and REY, the concentrations of most TEs in Metlaoui phosphorites are similar to or lower than those in average shale (Fig. 7).

To compensate for the effects of varying proportions of major diluent phases (quartz, opal-CT, carbonates) on the bulk sediment TE contents, TE enrichment factors (EF) were calculated relative to average shale, where EF element x = $(x/Al)_{sample}$ / $(x/Al)_{average\ shale}$. Selected EF data for all 8 sections are plotted in Fig. 12. Amongst the palaeoenvironmentally sensitive trace metals (Brumsack, 2006; Tribovillard et al., 2006; Little et al., 2015; Sweere et al., 2016), Cd, Cr, Mo, U and Zn show the highest enrichment factors (Fig. 12).

The fundamental physical chemistry and biogeochemical controls on TE behaviour in the environment will be the same in all sediments, but the resulting TE patterns in phosphorites may be different. This is exemplified by Mo-U covariation, which provides a proxy for seawater oxygenation and the redox status of bottom sediments (Tribovillard et al., 2012). Enrichment factors for these two elements in the Metlaoui phosphorites, in the order of 20–50 for Mo and 100–300 for U (Fig. 12), place these sediments outside the redox fields defined on shale-based bivariate discrimination diagrams (e.g. Tribovillard et al., 2012 fig. 1). Bearing this in mind, emphasis should be placed on differences in TE contents in different phosphorites, rather than absolute values or element ratios.

Detrital mineral proxies

Chromium and Zr, elements that are typically associated with heavy minerals (e.g. chromite, zircon) and silicates in the detrital fraction, are significantly enriched in Metlaoui phosphorites relative to average shale (Fig. 12). Zirconium shows a strong association with

other silicate and other heavy mineral associated elements (Fig. 10); no major differences are evident between basins, indicating similar siliciclastic fluxes. Moderate enrichment in Zr, despite lower concentrations than average shale (Figs. 7, 12, Table 1), support evidence for the inclusion of a sediment component (zircon) derived from contemporaneous acidic volcanism in the Metlaoui phosphorites (Clocchiatti and Sassi, 1972; Béji-Sassi et al., 1996; Béji-Sassi et al., 2001).

Interpretation of Cr enrichment (Fig. 12) is complicated by its ability to substitute for phosphorus in francolite (Jarvis et al., 1994), in addition to a common heavy mineral and glauconite association. Results of the PCA (Fig. 10) argue for the former being the dominant factor in the Metlaoui phosphorites. Chromium (VI) is soluble in oxic seawater, but is exported to the sediments as reduced Cr (III) via humic/fulvic acid complexes and/or adsorption to Fe- and Mn-oxyhydroxides (Little et al., 2015). It is not readily trapped within the sediments in the form of a sulphide and is generally lost to the overlying water column by diffusive/advective transport during sediment compaction. However, following liberation during organic matter decomposition and Fe-redox cycling it becomes available for incorporation by francolite, and therefore offers a potential productivity proxy in phosphorites. However, in the present case, it does not show trends that are consistent with other productivity proxies (Fig. 12, see below).

Productivity proxies

Barium and phosphate are classically used as measures of productivity (Brumsack, 2006; Paytan, 2009), but Ba may be lost to bottom waters during early sulphate reduction, and P is a major element in the phosphorites and therefore subject to multiple sedimentological and mineralogical controls. Barium generally shows no enrichment in Metlaoui phosphorites (Fig. 12), indicating likely post-depositional loss, although Northern Basins samples have higher enrichment factors.

Copper and Ni are moderately enriched in most Metlaoui phosphorites (Fig. 12), with the Northern Basins, and particularly Sekarna, displaying the highest enrichment factors. Nickel enrichment in particular is likely associated with the presence of glauconite at Sekarna. Copper and Ni EFs display a clear geographical trend in the Metlaoui-Gafsa Basin data, with progressive NW to SE decline in enrichment factors (Fig. 12; i.e. approaching the shoreline of Jeffara Island), with no corresponding change in phosphate contents (Table 1). Copper and Ni provide the best proxies for the organic carbon flux, itself a measure of surface water productivity (Tribovillard et al., 2006). Copper and Ni EFs generally show good correlation with TOC in sediments irrespective of their redox state, being predominantly supplied with organic matter (as organometallic complexes) and trapped after organic matter decay within sulphides. A Fe-Mn-oxyhydroxide association is indicated by the PCA analysis of the Metlaoui phosphorites (Fig. 10), although no TOC data are available for our samples.

Cadmium and Zn, elements that are also transferred to sediments principally via organic matter (Tribovillard et al., 2006), show the same geographical trend of concentrations in the Metlaoui-Gafsa Basin as Cu and Ni, but have a clear sphalerite association, indicating fixation by sulphate reduction following organic matter decay. Generally, Zn EFs show a straightforward relationship with TOC in modern organic-rich sediments (Little et al., 2015). Cadmium EFs in the Metlaoui phosphorites are extreme, exceeding 10,000 in several beds in the NW Metlaoui-Gafsa Basin sections. High Cd EFs of up to 800 occur today off the Peru margin in an open ocean setting with oxygen depletion driven by high productivity (Little et al., 2015), and enrichment in Cd and P with depletion in Mn (see below), as displayed by the Metlaoui phosphorites, are characteristics of coastal upwelling environments (Brumsack, 2006; Sweere et al., 2016).

Following the arguments made above, we interpret geographical variation in Cd, Cu, Ni and Zn EFs to reflect highest productivity in the deeper water areas of the NW Metlaoui-Gafsa Basin, and also high but more variable productivity in the Northern and Eastern Basins.

Redox proxies

Iron and Mn display similar geochemical behaviour. In oxic seawater both Fe (II) and Mn (II, IV) precipitate as Fe and Mn oxyhydroxides resulting in very low dissolved concentrations (<1 nM) in seawater (Little et al., 2015). These oxyhydroxides form part of a particulate shuttle that scavenges PO_4 and trace metals from the water column, but then dissolves in suboxic conditions accompanying organic matter decomposition in the sediment. This results in phosphate and Mn release, and a Fe-redox cycle that promotes francolite precipitation (e.g. Jarvis et al., 1994 fig. 3).

Variable low Fe contents in the Metlaoui phosphorites (Table 1) reflect the presence of minor glauconite, pyrite and ferromagnesian minerals in the sediments. Iron EF factors are close to 1 for all sections except Sekarna, where values of ~4 are a product of the more glauconitic facies. Manganese contents are universally low in the phosphorites, generally < 50 ppm in the Metlaoui-Gafsa and Eastern Basins, < 200 ppm in the Northern Basins (Table 1), corresponding to EFs of $< 10^{-4}$. This indicates extreme loss of Mn from the sediment by reduction and release via diffusion into suboxic bottom waters. Near complete loss of Mn from the sediment is a characteristic feature of modern coastal upwelling systems where the oxygen-minimum zone acts as a conveyor belt transporting Mn towards the open ocean (Brumsack, 2006).

Molybdenum, U and V are characteristically enriched in oxygen-depleted sediments (Tribovillard et al., 2006; Little et al., 2015) and show minimal detrital influences. For example, Mo is transferred to the sediment by absorption onto humic substances and Mn-oxyhydroxides or by uptake in solution with authigenic Fe-sulphides; Mo burial fluxes peak

in weakly sulphidic facies owing to greater aqueous Mo availability and to enhanced scavenging associated with Fe-Mn cycling (Algeo and Lyons, 2006; Algeo and Tribovillard, 2009), a process that also favours francolite precipitation (Jarvis et al., 1994). Uranium and V, by contrast, have a predisposition to become enriched under less reducing conditions than Mo. A strong coupling exists between the behaviour of Cd and U in suboxic porewaters (Rosenthal et al., 1995), and it is notable that these two elements display the highest EFs in the Metlaoui phosphorites (Fig. 12).

Molybdenum, U and V enrichments potentially allow suboxic environments to be differentiated from anoxic–euxinic ones (Tribovillard et al., 2006). All three elements have elevated enrichment factors in Metlaoui phosphorites, but U stands out as being present at significantly higher concentrations than in average shale (Fig. 7) and has very high EFs (Fig. 12). Low Mo/U ratios in shales characterise deposition in suboxic bottom and porewaters, while high ratios reflect euxinic conditions (Tribovillard et al., 2012). For phosphorites, preferential uptake of U by francolite may play a role in controlling element/U ratios. However, many phosphorites display no U enrichment (see discussion in Jarvis et al., 1994), so element ratio variation may still be diagnostic.

Metlaoui phosphorites display variable Mo, U and V contents, with the Sekarna deposit having the highest enrichment factors and concentrations in these elements (Figs. 7, 12). On balance, the trace metal geochemistry points to dominantly suboxic bottom-water conditions, evidenced by Mn depletion, with suboxic to anoxic porewaters in all three phosphorite basins. There is no evidence of water column euxinia, an interpretation supported by the ubiquitous bioturbation, although complementary TOC data are required to test this conclusion further.

5.3 Rare-earth elements and yttrium

The REEs have long been recognised as being enriched in phosphorites compared to other sedimentary rocks (Cossa, 1878; McKelvey, 1950; Altschuler et al., 1967).

978 *5.3.1 REEs and yttrium patterns*

979 There are strong positive inter-elemental correlations between all REY (Fig. 10, Tables 4,
980 5), which attest to their strong coherence as a geochemical group, their common processes of
981 enrichment, and their mineralogical association with francolite in phosphorites (McArthur and
982 Walsh, 1984; Jarvis et al., 1994). However, Pearson correlation analyses (Table 4) and PCA
983 (Fig. 10A) indicate that Fe-Mn oxyhydroxides play a role in hosting the REY in the Metlaoui
984 phosphorites. ΣREE contents reported here (Table 1; mean 370 ppm) are comparable to
985 published data from the Metlaoui Group, with higher levels present in Northern and Eastern
986 Basins localities than in the Gafsa-Metlaoui Basin (Béji-Sassi, 1984, 1999; Chaabani, 1995;
987 Béji-Sassi et al., 2005; Ounis et al., 2008; Ferreira da Silva et al., 2010; Galfati et al., 2010;
988 Garnit et al., 2012a, b).

989 The REY are readily incorporated into the apatite structure directly from seawater during
990 early diagenesis (McArthur and Walsh, 1984; Jarvis et al., 1994; Kocsis et al., 2016). For
991 example, fish debris apatite in slowly accumulating modern deep-sea muds may contain in
992 excess of 3 wt% ΣREY (Kon et al., 2014), despite concentration of <1 ppm in the original
993 biogenic phosphate (Elderfield and Pagett, 1986). Global secular variation in REE patterns in
994 biogenic apatite and coeval phosphorites has been used to support the argument that francolite
995 commonly preserves a largely unaltered seawater signal (Jarvis, 1984; Lécuyer et al., 1998;
996 Martin and Scher, 2004; Emsbo et al., 2015). However, early diagenetic uptake of REY from
997 modified porewater, or their subsequent incorporation during later diagenesis and weathering,
998 has been documented (McArthur and Walsh, 1984; Reynard et al., 1999; Shields and Stille,
999 2001; Kocsis et al., 2010; Herwartz et al., 2011). Additionally, for large constituents such as
1000 fossil bone, the REEs may be fractionated from one another during diffusive transport and
1001 adsorption (Trueman et al., 2011), leading to different patterns in the same sample.

Comparison between the shale-normalised REY patterns of Metlaoui Group phosphorites (Fig. 9) and those of modern waters and marine particulates (Fig. 13) demonstrates close similarity to surface-ocean and coastal waters and 'authigenic' marine particulates, with depletion in the LREEs, and significant negative Ce (low Ce/Ce* values) and positive Y [$Y/Y^* = 2Y_N/(Dy_N+Ho_N)$] anomalies (e.g. DeBaar et al., 1985; Shimizu et al., 1994; Alibo and Nozaki, 1999; Garcia-Solsona et al., 2014; Osborne et al., 2015). Weakly concave-down patterns caused by HREE depletion relative to the MREEs are apparent in the Sekarna and Jebel Jebs phosphorites (Fig. 9). These characteristics are also seen in modern organic matter (Freslon et al., 2014), 'lithogenic' particles (Garcia-Solsona et al., 2014), and 'anoxic' marine porewaters (Haley et al., 2004; Abbott et al., 2015; Fig. 13) although, in contrast to the phosphorites, none of these display significant negative Ce anomalies.

A plot of Ce/Ce* against shale-normalised Pr anomaly [$Pr/Pr^* = 2Pr_N/(Ce_N+Nd_N)$] confirms that the negative Ce anomalies in the Metlaoui phosphorites are not artefacts of La enrichment (Fig. 14A, cf. Bau and Dulski, 1996). Low Ce/Ce* and high Pr/Pr* values typical of modern open-ocean water characterise samples from the Northern Basins and older phosphorites in the Gafsa-Metlaoui Basin. Less negative Ce anomalies (higher Ce/Ce* values), comparable to those in many modern coastal waters (Elderfield et al., 1990) are displayed by the other phosphorites, with a clear stratigraphically-upwards trend of progressively less negative anomalies in the Gafsa-Metlaoui Basin sections (Figs. 10, 14A, 15).

Comparison of the general REE distribution, as expressed by a $(La/Yb)_N$ vs. $(La/Sm)_N$ plot (cf. Reynard et al., 1999), demonstrates patterns that are consistently less depleted in the LREEs compared to most modern open ocean seawater, but fall within the field of coastal and estuarine waters (Fig. 14B). This is consistent with the preservation of an original surface seawater pattern (Fig. 13), perhaps modified by limited early diagenetic adsorption of REEs

from porewaters. There is no evidence of late diagenetic overprinting that would generate lower La/Yb_N and La/Sm_N ratios (Reynard et al., 1999). Similarly, a plot of Y (Y/Y*) vs. La [$(La/Nd)_N$] anomalies shows that samples lie within or close to the seawater field (Shields and Stille, 2001), indicating minimal late diagenesis or weathering (Fig. 14C).

Ce/Ce* generally shows no general correlation with ΣREE (Fig. 14D) except in the Gafsa-Metlaoui Basin, where a stratigraphically-upwards trend towards less negative Ce anomalies (increasing Ce/Ce* values) and flatter REY patterns [increasing $(La/Yb)_N$ values] accompany consistently high P_2O_5 contents (Figs. 9, 14, 15, Table 1). Similar trends are apparent in the limited data set of Ounis et al. (2008). The Eastern Basins samples from Jebel Jebs show a strongly bimodal distribution with small negative Ce anomalies throughout, but extreme REE enrichment in the lower phosphorite beds (~1000 ppm ΣREE, Fig. 5), and moderate values (~300 ppm) in the upper phosphorite beds. Clearly, increasing REE contents do not *a priori* result in less negative Ce anomalies or flatter patterns, despite the trends seen in the Metlaoui-Gafsa Basin data set.

5.3.2 REEs and yttrium as palaeoenvironmental proxies

Metlaoui phosphorite REY patterns in the different basins are remarkably consistent (Fig. 9), despite the considerable differences in the location and age of the samples. Bulk sediment patterns are identical to grain analysis results from the same deposits (Garnit et al., 2012a). The seawater-like patterns in the phosphorites strongly support a shallow marine origin for the deposits. Phosphorites in the Northern Basins display the most negative Ce anomalies (lowest Ce/Ce* values); at Sra Ouertane, patterns are identical to modern surface open-ocean water. This indicates uptake of the REY by francolite either directly from seawater or via their early diagenetic remobilisation from ‘authigenic’ particulates (Figs. 9, 13), in oxic to suboxic surficial sediments with no significant element fractionation.

The higher ∑REE contents at Sekarna are associated with flatter of REY patterns, less negative Ce and lower Y anomalies, and HREE depletion. These characteristics are consistent with additional uptake of REEs from suboxic–anoxic porewaters and/or a higher proportion of the elements derived from an organic matter carrier phase. The presence of significant glauconite in these sediments also likely plays a role since that mineral typically displays REE enrichment, with no anomalies and HREE depletion (Jarvis and Jarvis, 1985; Jarrar et al., 2000; Tóth et al., 2010). Significantly, the high REE content of glauconite grains has been attributed to the presence of REE-bearing phosphates [both apatite and an unidentified (REE, Ca)-phosphate] as co-genetic impregnation or pore fillings within glauconite clay aggregates (Tóth et al., 2010). Similar overall REY patterns are displayed at Jebel Jebs in the Eastern Basins, but here with less negative Ce and lower Y anomalies. This section displays the highest ∑REE contents, indicating greater diagenetic enrichment from porewaters.

In the Gafsa-Metlaoui Basin, the lowest ΣREE concentrations occur in our stratigraphically lowest samples (generally Beds VIII and VII, and the laterally equivalent Bed III in Jellabia and Mzinda; Figs. 5, 15). These low REE contents and seawater-like patterns accompany TE evidence of high productivity – i.e. high Ni and Cu EFs. Upward decreasing productivity (indicated by falling Ni and Cu EFs) accompanies less negative Ce anomalies, flatter REE patterns and increasing ΣREE (Fig. 15). Tlili et al. (2011) have previously documented a trend of systematically upwards-falling TOC in both the bulk rock and in the fine fraction of marls (<2 μm; 4–1% TOC) through the Chouabine Formation at Kef Eddour. Low (<1) pristine/phytane ratios of 0.9–0.6 indicate preservation of organic matter under reducing conditions.

The Gafsa-Metlaoui Basin is considered to have been a semi-restricted basin during the Early Paleogene, with limited and likely intermittent exchange with Tethyan Ocean water

from the east, via the Chamsi (Shemsi) Channel and Maknassy–Mezzouna shoal. The basin deepened to the west and NW, and it is envisaged that a more open connection to Tethyan waters existed via the northern connections of the Saharan Gulf (Fig. 1B). The arid climate, and the small surface area and low relief of the adjacent Kasserine and Djeffara islands (Belayouni, 1984; Felhi et al., 2008; Tlili et al., 2011), would have limited any input of freshwater into the basin.

We interpret the stratigraphic trends in the Gafsa-Metlaoui Basin (Fig. 15) as reflecting increasing isolation of the basin during Chouabine deposition, with reduced nutrient input from upwelling leading to falling productivity and declining sedimentation rates. An increased residence time of organic matter in surficial suboxic–anoxic sediments led to decreased organic matter preservation (lower TOC content) and increased redox cycling of phosphate and REEs present in the organic fraction. A decreasing supply of deep open-ocean seawater combined with an increasing proportion of organic matter derived REEs, resulted in the flatter patterns and less negative Ce anomalies observed through the sections.

A temporary reversal of the geochemical trend is seen in Bed II, interpreted to represent the basal Eocene and equate to the PETM (Fig. 15, see above). The marls immediately below this also show a temporary reversal in trend, with a spike in TOC (Tlili et al., 2011). The PETM coincides with a short episode of maximum flooding (Sluijs et al., 2008), so it is possible that isolation of the basin was temporarily reversed by a global flooding event, prior to continued isolation during the subsequent relative sea-level fall accompanying a eustatic late highstand (i.e. falling stage system tract; cf. Catuneanu et al., 2011).

5.4 Depositional environments in the Metlaoui phosphorite basins

Results of bulk geochemical and phosphate grain analyses consistently indicate that Sra Ouertane, and to a lesser extent Sekarna, in the Northern Basins were characterised by the most open marine settings with oxic–suboxic conditions despite relative high organic matter

fluxes. The high and variable Ba, Cu, Ni, Sc, V, U and REY content and pronounced negative Ce anomaly in the phosphorites of the Northern Basins reflect a more direct connection with the open ocean, and relatively higher but fluctuating productivity compared to the Gafsa-Metlaoui Basin. The higher Hf, Nb, Rb and Zr contents of the phosphorites from the Northern and Eastern Basins, along with the positive correlations between these elements and Al_2O_3 and TiO_2 as a proxy for detrital inputs, confirm that these basins received more terrigenous input during the deposition of the phosphorites compared to the Gafsa-Metlaoui Basin, probably owing to their closer proximity to Kasserine Island and wetter local climate.

The Sekarna phosphorites display a distinctive element association related to the glauconitic facies. Unique Fe enrichment is associated with high general productivity proxies (Ba, Cu, Ni), but low sphalerite contents (low Cd, Zn) and high Mo, U, V indicating suboxic conditions and greater Fe input flux. The kaolinite and illite dominated clay mineral assemblage points to locally warm humid climate conditions. In Egypt and elsewhere Cretaceous glauconitic phosphorite facies have been tied to more nearshore areas where elevated iron fluxes originate from regions of lateritic weathering (Glenn and Arthur, 1990; Föllmi, 1996). This may be the case here.

The Eastern Basins (Jebel Jebs) and Gafsa-Metlaoui Basin were characterized by semi-restricted settings associated with suboxic bottom waters but more reducing sediments.

5.5 Sea-level change

Increased water mass isolation of the Gafsa-Metlaoui Basin might be explained by a sea-level fall causing the progressive restriction of the basin during the Late Paleocene. A long-term eustatic sea-level fall is recorded during the Paleocene–Early Eocene (Müller et al., 2008), which would have had greatest impact in shallow-water basins like Gafsa-Metlaoui. However, a number of medium- and short-term cycles of eustatic sea-level rise and falls occurred within this time interval (Haq et al., 1987; Miller et al., 2005; Kominz et al., 2008),

and a review by Sluijs et al. (2008) revealed a global pattern of latest Paleocene transgression, maximum flooding coincident with the Paleocene–Eocene Thermal Maximum (PETM), immediately above the series boundary, followed by a highstand and sea-level fall.

The Chouabine Formation is generally considered to be a predominantly transgressive unit (Sassi, 1974; Henchiri, 2007). El Ayachi et al. (2016) distinguished five third-order sequences within the Thelja section of the Gafsa-Metlaoui Basin, interpreted to represent low-amplitude (<25 m) eustatic sea-level cycles superimposed on a longer-term, rising sea-level trend. Replacement of the bioclastic limestones, dolostones, marls and evaporites of the Thelja Formation in the Gafsa-Metlaoui Basin by organic-rich marls and phosphorites yielding organic walled dinoflagellate cysts and planktonic foraminifera in the their lower part confirms the trangressive nature of the lower Chouabine. Subsequent basin isolation and decreasing productivity, however, indicate relative sea-level fall and/or restriction of the open ocean connection.

We have not characterised the basal phosphorite in the Gafsa-Metlaoui Basin (Bed IX), but it is notable that the lowest phosphorites in the Northern and Eastern Basins display a distinct geochemical signature (Figs. 10, 11) that includes the highest ∑REE values (Fig. 8), despite differing REY patterns (Fig. 9). These transgressive deposits likely represent a condensed facies that was subject to greater amounts of sediment reworking in relatively shallower water environments, which favoured greater TE and REY recycling and incorporation by francolite (Jarvis, 1984, 1992).

5.6 Connections to the Tethys Ocean

Neodymium isotopes provide a water mass proxy in the oceans. The Nd isotope ratio [εNd] in seawater is heterogeneous because of the element's low concentration and short residence time of 360 yr (Arsouze et al., 2009), compared to a global ocean mixing time of ~ 1000 yr (Broecker and Peng, 1982). Weathering of mafic volcanic and mantle-derived rocks

produces water with high εNd values, while old crustal rocks yield low, unradiogenic, signatures. Modern surface (0–126 m) Pacific water is characterised by εNd = -2 to -5, as compared to Atlantic surface water with εNd = -10 to -15 (Rempfer et al., 2011). Additionally, significant geographic and depth-related variation results from changing source compositions, water mass distributions, and water column scavenging process.

Neodymium isotope analyses of Gafsa-Metlaoui Basin biogenic phosphate have yielded εNd(t) values of -8.5 ± 0.6 (Shaw and Wasserburg, 1985; Soudry et al., 2006; Kocsis et al., 2013). Slightly more radiogenic values (εNd(t) = -5.3 ± 1.1; values recalculated after Kocsis et al., 2016) have been reported from a range of southern Tethyan localities in the Middle East (Israel, Egypt, Jordan and Syria; Soudry et al., 2006) and Morocco of (εNd(t) = -6.2 ± 0.4; Kocsis et al., 2016). This points to the influence of a local unradiogenic Nd source in the semi-confined Gafsa-Metlaoui Basin, perhaps related to groundwater input (Johannesson and Burdige, 2007). Interaction with unradiogenic Atlantic Ocean water is considered to be unlikely, since geological data and palaeoceanographic models point to a dominantly west-flowing current system along the south Tethyan margin (Fig. 1).

An open connection to the Tethys ocean at the onset (Bed IX) and termination (Bed 0 and Kef Eddour Formation) of phosphorite deposition is indicated by consistent $^{87}Sr/^{86}Sr$ and $\delta^{18}O$ values in shark teeth (Ounis et al., 2008; Kocsis et al., 2013) that are similar to latest Paleocene global values (Sluijs et al., 2006; Frieling et al., 2014). An open marine linkage is supported by records of diverse planktonic foraminifera assemblages within the lower Chouabine Formation marls between beds IX and VIII (Bolle et al., 1999). Large variation and anomalously high or low $^{87}Sr/^{86}Sr$ ratios and high $\delta^{18}O$ values in the main phosphorites beds (VIII – I; Ounis et al., 2008; Kocsis et al., 2013, 2014) point to more restricted basin conditions, confirming our interpretation of the TE and REY data.

6. Conclusions

Major Paleocene–Eocene phosphorite deposits occur in three basinal areas of central and northern Tunisia, the: Northern Basins, Eastern Basins and Gafsa-Metlaoui Basin. Stable warm arid climate conditions in the Gafsa-Metlaoui Basin and the surrounding epicontinental area during the latest Paleocene are indicated by: (1) an association of the phosphorites with sabkha evaporites; (2) evidence of minimal siliciclastic input, with clay mineral assemblages dominated by smectite and high proportions of palygorskite and sepiolite. Wetter more seasonal climate is suggested for ocean-facing settings in the other basins.

Major-element, trace-element (TE) and rare-earth element and yttrium (REY) data from the phosphorites demonstrate distinctive geochemical signatures for the three basins. Pearson correlation and principal component analysis differentiate specific element groups, ascribed largely to mineralogical controls by: carbonate fluorapatite (francolite; P_2O_5, CaO, Na_2O, SO_3, Cr, U, Sr, Th, REY); silicates and heavy minerals (quartz, feldspars, ferromagnesian minerals, clays, zeolites, heavy minerals; SiO_2, TiO_2, Al_2O_3, MgO, K_2O, Ba, Hf, Nb, Rb, Zr); ferromanganese oxyhydroxides and glauconite (Fe_2O_3, MnO, As, Cu, Mo, Ni, Sb, Sc); sulphides (sphalerite; Cd, Zn).

Geochemical signatures and trends are products of variation in mineralogy and mineral chemistry that reflect water mass composition, nutrient availability, surface-water productivity, siliciclastic supply, sedimentation rate, bottom- and pore-water redox conditions, and authigenic mineralogy. Bulk-sediment elemental data are consistent with phosphate grain microanalyses, confirming the predominance of francolite in controlling bulk-rock geochemistry. Extreme Mn depletion, enrichment of Mo, U, V and other transition metals but low Mo/U ratios, point to suboxic bottom waters and suboxic to anoxic porewaters accompanying francolite precipitation.

1199 The Northern Basins show the strongest Tethys Ocean influence, with surface open-
1200 ocean seawater REY patterns consistently developed in the Sra Ouertane deposit.
1201 Phosphorites in the Basins display considerable bed-scale compositional variation, with
1202 varying proportions of detrital minerals and carbonates producing erratic phosphate contents.
1203 Glauconitic phosphorites in the Sekarna succession have high Cu, Ni, Mo, U, and V
1204 enrichment factors but the lowest Cd and Zn values. These, together with the highest Fe and
1205 Mn values and heavy rare-earth element depleted signatures, point to high productivity but
1206 extensive organic-matter recycling in oxic to suboxic bottom water and suboxic to weakly
1207 sulphidic porewaters.

1208 Marine transgression in the Gafsa-Metlaoui Basin during the Late Paleocene renewed an
1209 open connection to Tethyan waters following a phase of basin restriction during Thelja
1210 Formation times. Improved circulation of open ocean water initiated upwelling, high organic
1211 and siliceous productivity, bottom-water oxygen depletion, enhanced organic matter
1212 deposition, and phosphogenesis in the Basin sediments. The phosphorite – organic-rich marl
1213 – diatom-bearing porcelanite facies, represents the classic coastal upwelling trinity.
1214 Enrichment in Cd and P with depletion in Mn is characteristics of high productivity coastal
1215 upwelling environments, and a decrease in marine productivity from NW to SE in the Gafsa-
1216 Metlaoui Basin is indicated by systematically falling enrichment factors for Cu, Ni, Cd and
1217 Zn in the more southeastern sections. Phosphorite deposition occurred under increasing arid
1218 climate conditions accompanying global Paleocene–Eocene warming.

1219 The main package of commercial phosphorites (Beds VIII – I, Chouabine Formation) in
1220 the Gafsa-Metlaoui Basin accumulated around Paleocene–Eocene boundary time. Upwards
1221 decreasing organic carbon contents and trace-element (Cu, Ni, Cd, Zn) enrichment factors,
1222 together with progressively less negative Ce anomalies and flatter REY distribution patterns,
1223 indicate declining productivity and increasing basin isolation during phosphorite deposition.

1224 This trend was temporarily reversed during an episode of flooding associated with the earliest
1225 Eocene Paleocene–Eocene Thermal maximum (PETM), but continued thereafter.
1226

1227 **Acknowledgements**

1228 The authors are grateful to the Groupe Chimique Tunisien (GCT) for funding the
1229 geochemical analyses at Actlabs (Canada). We thank the geologists of Compagnie des
1230 Phosphate de Gafsa (CPG) for assistance in collecting samples in the Gafsa-Metlaoui Basin,
1231 and we especially thank Bousairi Boujlel, Mohamed Salah Naili and Amara Awled Ghrib.
1232 The manuscript benefited from careful critical appraisal by Karl Föllmi, three anonymous
1233 reviewers, and journal editor Damien Delvaux.

Table captions

Table 1 Concentration of major elements (%), trace elements (ppm), rare earth elements (ppm), and elemental ratios in 58 phosphorite samples from the three phosphatic basins in Tunisia. Element concentrations for Sekarna samples are from Garnit et al. (2012b).

Table 2 Concentration (ppm) of trace elements determined by LA-ICP-MS for sphalerite (nd: not detected).

Table 3 Concentration (ppm) of trace elements determined by LA-ICP-MS for pyrite (nd: not detected).

Table 4 Inter-elemental correlations based on the Pearson correlation coefficient.

Table 5 Loadings of 45 geochemical variables in the Tunisian phosphorites on four significant principal components.

Table 6 Structural formulas of francolite from the phosphorite deposits from different basins (after Ounis, 2011).

Table A1 Mineralogy of 58 phosphorite samples from the three phosphorite basins of Tunisia determined by semi-quantitative x-ray diffraction.

Figure captions

Fig. 1. Location and stratigraphy of the study area. (A) General location of the central Tunisia study area in North Africa. (B) Early Eocene palaeogeography of Tunisia (modified from Zaïer et al., 1998) showing depositional settings of the three study basins. (C) Summary stratigraphy of the study interval in the Gafsa-Metlaoui Basin (compiled from Chaabani, 1995; Ounis, 2011; Kocsis et al., 2014). Study samples from the Basin originate from the Chouabine Formation, interval highlighted by the green box.

Fig. 2. Location and field characteristics of the *Northern Basins study sections.* (A) *Geological map of Northern Basins showing the locations of the study sites* (modified from Ben Haj Ali et al., 1985). (B) Field view of the Chouabine Formation from Sra Ouertane (Jebel Ayata). (C) Field view from Sekarna showing the main outcrops (modified from Garnit et al., 2012a).

Fig. 3. Location and field characteristics of the *Eastern Basins study sections.* (A) *Geological map of Eastern Basins showing the location of the study sites* (modified from Ben Haj Ali et al., 1985). (B) Field view of the southern flank of Jebel Jebs showing the general stratigraphic succession, which is approximately 130 m thick. (C) and (D) Successions illustrating the lower and upper phosphorite beds of the Metlaoui Group on the southern edge of the Jebel Jebs syncline; both phosphorite packages are around 20 m thick.

Fig. 4. Location and field characteristics of the *Gafsa-Metlaoui Basin study sections.* (A) *Geological map of Gafsa-Metlaoui Basin showing the location of the study sites* (modified from Ben Haj Ali et al., 1985). (B) Field view of the Chouabine Formation in Kef Eddour open cast mine showing beds of economic phosphorite ore (I – VII; bed numbers after Ounis et al., 2008) and sterile interbeds. Face is approximately 30 m high. (C) Field view of the 'phosphate of the roof' in the Kef Eddour Formation, Mzinda mine. (D) Field view of a

working face in Jellabia 56 mine showing Mio-Pliocene sediments discordantly overlying the Upper Paleocene – Eocene Metlaoui Group.

Fig. 5. Location map and summary logs for representative sections of the Chouabine Formation and its lateral equivalents from the Metlaoui Group in the Northern Basins (Sra Ouertane, Sekarna; blue name labels), Eastern Basins (Jebel Jebs; red name labels), and Gafsa-Metlaoui Basin (Naguess to Jellabia 56; green name labels). Northern Basins stratigraphy after Zaïer (1999); Eastern Basins stratigraphy after Béji-Sassi (1999); phosphorite bed nomenclature in the Gafsa-Metlaoui Basin after Ounis et al. (2008). Sample locations are indicated by the black triangles. PETM = Paleocene–Eocene Thermal Maximum; EECO = Early Eocene Climatic Optimum (Zachos et al., 2001; McInerney and Wing, 2011).

Fig. 6. Ternary diagrams illustrating selected major oxide variation in Metlaoui Group phosphorites. Numerical data are presented in Table 1. Symbol colour conventions: Northern Basins samples, blue; Eastern Basins samples, red; Gafsa-Metlaoui Basin samples, green. Stoichiometric compositions of the main mineral phases identified by light microscopy and x-ray diffraction studies are shown for comparison.

Fig. 7. Trace-element variation diagrams for Metlaoui Group phosphorites normalised to average shale. (A, B) Northern Basins sections. (C) Eastern Basins section. (D – H) Gafsa-Metaloui Basin sections. Consistent patterns relative to average shale (Wedepohl, 1971) that generally follow average phosphorite (yellow stars; Altschuler, 1980), indicate that francolite chemistry dominates the bulk sediment composition. Anomalously high concentations of Cr, Sr, Zn and Cd, and depletion of siliciclastic associated elements Rb, Zr, Nb, Hf, Ni, plus Ba, Cu and As, particularly in the Gafsa-Metlaoui Basin sections (D – H), are notable.

Fig. 8. Bivariate plot of total rare-earth elements (∑REE, ppm) versus P_2O_5 (%) contents in Metlaoui Group phosphorites. Note the lack of correlation between the two parameters in the Gafsa-Metaloui Basin deposits.

Fig. 9. Shale-normalized rare-earth element and Y (REY) patterns of Metlaoui Group phosphorites. Post-Archean average shale (PAAS) values after McLennan (1989). Sekarna data from Garnit et al. (2012b). Gafsa-Metaloui Basin sections show systematic increases in ∑REE, flatter shale-normalised patterns, and progressively less negative Ce anomalies upwards through each section.

Fig. 10. Loading plots for the first two factors from the Principal Components Analysis (PCA) of Metlaoui Group geochemical data. (A) Geochemical constituent plot. (B) Sample plot. PCA loading values are presented in Table 5.

Fig. 11. Dendrogram resulting from hierarchical cluster analysis (HCA) of the 45 geochemical variables determined in Metlaoui Group phosphorite samples.

Fig. 12. Trace-element enrichment factors in Metlaoui Group phosphorites compared to average shale (Wedepohl, 1971). EF element x = $(x/Al)_{sample}$ / $(x/Al)_{average\ shale}$. Box-and-whisker plots show minimum and maximum values linked by vertical lines, range of the second and third quartiles (25 – 75%, rectangles), and median values (50%, horizontal lines inside rectangles). Section data are presented in numerical order and colour coded to indicate their basins of origin: blue, Northern Basins; red, Eastern Basins; green Gafsa-Metlaoui Basin.

Fig. 13. Characteristic shale-normalised REY patterns of particulate and dissolved fractions in the modern oceans. Patterns are schematic representations of multiple published data, derived as follows: hydrogenous Fe-Mn crusts (Bau and Dulski, 1996; Bau et al., 2014); organic matter (Freslon et al., 2014); Fe-Mn oxyhydroxides (Palmer and Elderfield, 1986; Bayon et al., 2004; Charbonnier et al., 2012); ‘authigenic’ and ‘lithogenic’ particulates

(Garcia-Solsona et al., 2014); biogenic carbonates and marine vertebrates (Elderfield and Pagett, 1986; Sholkovitz and Shen, 1995; Webb and Kamber, 2000; Wyndham et al., 2004; Labs-Hochstein and MacFadden, 2006; Liu et al., 2011; Charbonnier et al., 2012; Zaky et al., 2015); anoxic brine (Bau et al., 1997); marine porewaters (Haley et al., 2004; Abbott et al., 2015); ocean water (DeBaar et al., 1985; Shimizu et al., 1994; Alibo and Nozaki, 1999; Garcia-Solsona et al., 2014; Osborne et al., 2015). Post-Archean average shale (PAAS) values after McLennan (1989).

Fig. 14. Rare-earth element and Y discrimination diagrams of Metlaoui Group phosphorites. (A) Plots of shale-normalised Ce anomaly [$Ce/Ce^* = 3Ce_N/(2La_N+Nd_N)$] against shale-normalised Pr anomaly [$Pr/Pr^* = 2Pr_N/(Ce_N+Nd_N)$], after Bau and Dulski (1996). Note that Tunisian phosphorite samples define a linear array entirely within the negative Ce anomaly field, with low Ce/Ce* values typical of modern open-ocean water characterising samples from the Northern Basins. (B) Compilation of shale-normalized $(La/Yb)_N$ ratios plotted against $(La/Sm)_N$ ratios of Tunisian phosphorites (cf. Reynard et al., 1999). Phosphorite patterns are tightly clustered within a field characteristic of unfractionated REE uptake by phosphate from coastal water and/or incorporation of REEs from open ocean water with adsorption processes causing mildly elevated $(La/Yb)_N$ values. (C) Yttrium anomaly [$Y/Y^* = 2Y_N/(Dy_N+Ho_N)$]) plotted against La anomaly $(La/Nd)_N$ showing a positive correlation (after Shields and Stille, 2001). Most samples fall within the 'seawater' field. (D) Cerium anomaly plotted against total REE. Note the large scatter in ∑REE values that show no correlation with Ce anomaly in the Northern and Eastern Basins.

Fig. 15. Stratigraphic variation in key REE and TE parameters through the Paleocene–Eocene boundary interval in the Gafsa-Metlaoui Basin. Data from all 5 sections are compiled and plotted against a composite log, following the correlations presented in Fig. 5. Open symbols are individual data point; colour-filled symbols are bed mean values; trend lines are

schematic. Note that vertical trends in the different parameters accompany no significant change in the phosphate content of the main phosphorite beds (I – VIII; 26.8±0.9% P_2O_5).

References

Abbott, A.N., Haley, B.A., McManus, J., Reimers, C.E., 2015. The sedimentary flux of dissolved rare earth elements to the ocean. Geochim. Cosmochim. Acta 154, 186–200.

Adatte, T., Keller, G., Stinnesbeck, W., 2002. Late Cretaceous to early Paleocene climate and sea-level fluctuations: the Tunisian record. Palaeogeogr. Palaeoclimatol. Palaeoecol. 178, 165–196.

Ahmed, A.H., Tlili, A., Zalat, A.A., Jeddoui, Y., 2015. Fossil diatoms from endogangue of the Ypresian phosphatic pellets of the Gafsa-Metlaoui basin: implication on the origin of biogenic silica and depositional environment. Arab. J. Geosci. 8, 1077–1087.

Algeo, T.J., Lyons, T.W., 2006. Mo-total organic carbon covariation in modern anoxic marine environments: Implications for analysis of paleoredox and paleohydrographic conditions. Paleoceanography 21, doi: 10.1029/2004pa001112.

Algeo, T.J., Tribovillard, N., 2009. Environmental analysis of paleoceanographic systems based on molybdenum–uranium covariation. Chem. Geol. 268, 211–225.

Alibo, D.S., Nozaki, Y., 1999. Rare earth elements in seawater: Particle association, shale-normalization, and Ce oxidation. Geochim. Cosmochim. Acta 63, 363–372.

Altschuler, Z.S., 1980. The geochemistry of trace elements in marine phosphorites. Part I: Characteristic abundances and enrichment, in: Bentor, Y.K. (Ed.), Marine Phosphorites, SEPM Spec. Publ. 29, 19–30.

Altschuler, Z.S., Berman, S., Cuttiti, F., 1967. Rare earths in phosphorites - geochemistry and potential recovery. US Geol. Surv. Prof. Paper 575(B), B1–B9.

Arsouze, T., Dutay, J.C., Lacan, F., Jeandel, C., 2009. Reconstructing the Nd oceanic cycle using a coupled dynamical - biogeochemical model. Biogeosciences 6, 2829–2846.

Barringer, J.L., Reilly, P.A., Eberl, D.D., Blum, A.E., Bonin, J.L., Rosman, R., Hirst, B., Alebus, M., Cenno, K., Gorska, M., 2011. Arsenic in sediments, groundwater, and streamwater of a glauconitic Coastal Plain terrain, New Jersey, USA - Chemical "fingerprints" for geogenic and anthropogenic sources. Appl. Geochem. 26, 763–776.

Baturin, G.N., 2006. Cadmium and zinc in Namibian shelf phosphorites. Dokl. Earth Sci. 407, 330–334.

1379 Bau, M., Dulski, P., 1996. Distribution of yttrium and rare-earth elements in the Penge and
1380 Kuruman iron-formations, Transvaal Supergroup, South Africa. Precambrian Res. 79, 37–
1381 55.
1382 Bau, M., Dulski, P., 1999. Comparing yttrium and rare earths in hydrothermal fluids from the
1383 Mid-Atlantic Ridge: implications for Y and REE behaviour during near-vent mixing and
1384 for the Y/Ho ratio of Proterozoic seawater. Chem. Geol. 155, 77–90.
1385 Bau, M., Moller, P., Dulski, P., 1997. Yttrium and lanthanides in eastern Mediterranean
1386 seawater and their fractionation during redox-cycling. Mar. Chem. 56, 123–131.
1387 Bau, M., Schmidt, K., Koschinsky, A., Hein, J., Kuhn, T., Usui, A., 2014. Discriminating
1388 between different genetic types of marine ferro-manganese crusts and nodules based on
1389 rare earth elements and yttrium. Chem. Geol. 381, 1–9.
1390 Bayon, G., German, C.R., Burton, K.W., Nesbitt, R.W., Rogers, N., 2004. Sedimentary Fe-
1391 Mn oxyhydroxides as paleoceanographic archives and the role of aeolian flux in regulating
1392 oceanic dissolved REE. Earth Planet. Sci. Lett. 224, 477–492.
1393 Bech, J., Suarez, M., Reverter, F., Tume, P., Sanchez, P., Roca, N., Lansac, A., 2010.
1394 Selenium and other trace element in phosphorites. A comparison between those of the
1395 Bayovar-Sechura and other provenances. J. Geochem. Explor. 107, 146–160.
1396 Béji-Sassi, A., 1984. Pétrographie, minéralogie et géochimie des sediments phosphatés de la
1397 bordure oriental de l'Ile de Kasserine (Tunisie). These 3ème cycle, Université d'Orléans, p.
1398 230.
1399 Béji-Sassi, A., 1999. Les phosphates dans les basins Paléogènes de la partie méridionale de
1400 l'axe Nord-Sud (Tunisie), Thèse de doctorat d'état, Department of Geology. Univ. Tunis II,
1401 Tunis.
1402 Béji-Sassi, A., Sassi, S., 1999. Le cadmium associé aux dépôts phosphatés de la Tunisie
1403 méridionale. J. Afr. Earth Sci. 29, 501–513.
1404 Béji-Sassi, A., Laridhi-Ouzaa, N., Clocchiati, R., 1996. Les inclusions vitreuses des ilménites,
1405 apatites et quartz des sédiments phosphatés de Tunisie: témoignages d'un volcanisme
1406 alcalin d'âge paléocène supérieur à éocène. Bull. Soc. géol. France 167, 227–234.
1407 Béji-Sassi, A., Laridhi-Ouzaa, N., Zäier, A., Clocchiati, R., 2001. Paleocene–Early Eocene
1408 alkaline volcanic activity in Tunisian phosphatic sediments. Comparison with Cretaceous
1409 magmatism and geodynamic sgnificance. Les journées de ETAP, 47–58.
1410 Béji-Sassi, A., Zaïer, A., Joron, J.L., Treuil, M., 2005. Rare earth elements distribution of
1411 Tertiary phosphorites in Tunisia, in: Mao, J., Bierlein, F.P. (Eds.), Mineral Deposit
1412 Research: Meeting the Global Challenge. Springer, Berlin, pp. 1061–1064.

1413 Belayouni, H., 1984. Étude de la matière organique dans la série phosphatée du bassin de
1414 Gafsa-Métlaoui (Tunisie): application à la compréhension des mécanismes de la
1415 phosphatogenèse. Documents BRGM, 77, p. 204.
1416 Belayouni, H., Trichet, J., 1980. Glucosamine as a biochemical marker for dinoflagellates in
1417 phosphate sediments, in: Douglas, A.G., Maxwell, J.R. (Eds.), Advances in Organic
1418 Geochemistry 1979: Proceedings of the Ninth International Meeting on Organic
1419 Geochemistry, University of Newcastle-upon-Tyne, UK. Pergamon, Oxford, pp. 205–210.
1420 Belayouni, H., Trichet, J., 1983. Preliminary data on the origin and diagenesis of the organic
1421 matter in the phosphate basin of Gafsa, in: Bjorøy, M. (Ed.), Advances in Organic
1422 Geochemistry 1981: Proceedings of the 10th International Meeting on Organic
1423 Geochemistry, University of Bergen, Norway, 14–18 September 1981. Pergamon, Oxford,
1424 pp. 328–335.
1425 Belayouni, H., Slansky, M., Trichet, J., 1990. A study of the organic matter in Tunisian
1426 phosphates series; relevance to phosphorite genesis in the Gafsa Basin (Tunisia). Org.
1427 Geochem. 15, 47–72.
1428 Ben Abdessalem, N., 1978. Etude palynologique et micro-paléontologique de la série
1429 phosphatée du bassin de Gafsa-Metlaoui (Tunisie). Application à la comprehension des
1430 mécanismes de la phosphatogenèse. Thèse 3eme cycle, Université Paris VI, Paris.
1431 Ben Haj Ali, M., Jedoui, Y., Dali, T., Ben Salem, H., Memmi, L., 1985. Carte géologique a
1432 l'échelle 1:500 000 de la Tunisie. Service géologique Tunisie.
1433 Ben Haj Ali, M., Kadri, A., Zagrarni, M.F., M.E., G., 2002. Les unités lithostratigraphiques
1434 de l'Eocène en Tunisie: Evolution latérale et actualisation de la nomenclature. Note. Serv.
1435 géol. Tunisie 69.
1436 Ben Hassen, A., Trichet, J., Disnar, J.-R., Belayouni, H., 2009. Données nouvelles sur le
1437 contenu organique des dépôts phosphatés du gisement de Ras-Draâ (Tunisie). CR Geosci.
1438 341, 319–326.
1439 Ben Hassen, A., Trichet, J., Disnar, J.-R., Belayouni, H., 2010. Pétrographie et géochimie
1440 comparées des pellets phosphatés et de leur gangue dans le gisement phosphaté de Ras-
1441 Draâ (Tunisie). Implications sur la genèse des pellets phosphatés. Swiss J. Geosci. 103,
1442 457–473.
1443 Berner, R.A., 1984. Sedimentary pyrite formation - an update. Geochim. Cosmochim. Acta
1444 48, 605–615.
1445 Bolle, M.P., Adatte, T., 2001. Palaeocene–early Eocene climatic evolution in the Tethyan
1446 realm: clay mineral evidence. Clay Min. 36, 249–261.

1447 Bolle, M.P., Adatte, T., Keller, G., Von Salis, K., Burns, S., 1999. The Paleocene–Eocene
1448 transition in the southern Tethys (Tunisia): climatic and environmental fluctuations. Bull.
1449 Soc. géol. France 170, 661–680.
1450 Broecker, W.S., Peng, T.-H., 1982. Tracers in the Sea. Eldigio Press, Palisades NY, p. 690.
1451 Brumsack, H.-J., 2006. The trace metal content of recent organic carbon-rich sediments:
1452 Implications for Cretaceous black shale formation. Palaeogeogr. Palaeoecol.
1453 Palaeoclimatol. 232, 344–361.
1454 Bujak, J.P., Brinkhuis, H., 1998. Global warming and dinocyst changes across the
1455 Paleocene/Eocene Epoch boundary, in: Aubry, M.-P., Lucas, S.G., Berggren, W.A. (Eds.),
1456 Late Paleocene – Early Eocene Climatic and Biotic Events in the Marine and Terrestrial
1457 Records. Columbia University Press, New York, pp. 277–295.
1458 Burollet, P.F., 1956. Contribution à l'étude stratigraphique de la Tunisie centrale. Ann. Mines
1459 Géol. (Tunisie) 18, p. 352.
1460 Burollet, P.F., Oudin, J.-P., 1980. Paléocène et Eocène en Tunisie - Pétrole et phosphate,
1461 Géologie Comparée des Gisements de Phosphate et de Pétrole. BRGM, Orléans, pp. 205–
1462 216.
1463 Castany, G., 1951. Etude géologique de l'Atlas tunisien oriental. Royaume de Tunis. Ann.
1464 Mines Géol. (Tunisie) 8, p. 632.
1465 Catuneanu, O., Galloway, W.E., Kendall, C.G.S.C., Miall, A.D., Posamentier, H.W., Strasser,
1466 A., Tucker, M.E., 2011. Sequence stratigraphy: methodology and nomenclature. Newsl.
1467 Stratigr. 44, 173–245.
1468 Cayeux, L., 1896. Note préliminaire sur la constitution des phosphates de chaux du Sénonien
1469 du sud de la Tunisie. CR Acad. Sci. Paris 123, 273–276.
1470 Cayeux, L., 1941. Les Phosphates de Chaux Sédimentaires de France II. l'Imprimerie
1471 Nationale, Paris, p. 659.
1472 Chaabani, F., 1995. Dynamique de la partie orientale du bassin de Gafsa au Crétacé et au
1473 Paléogène: Etude minéralogique et géochimique de la série phosphatée Eocène, Tunisie
1474 méridionale. Thèse Doctrat d' Etat, Université de Tunis II, Tunis.
1475 Chamley, H., 1989. Clay Sedimentology. Springer-Verlag, Berlin, Heidelberg, p. 623.
1476 Charbonnier, G., Puceat, E., Bayon, G., Desmares, D., Dera, G., Durlet, C., Deconinck, J.F.,
1477 Amedro, F., Gourlan, A.T., Pellenard, P., Bomou, B., 2012. Reconstruction of the Nd
1478 isotope composition of seawater on epicontinental seas: Testing the potential of Fe-Mn
1479 oxyhydroxide coatings on foraminifera tests for deep-time investigations. Geochim.
1480 Cosmochim. Acta 99, 39–56.

1481 Clocchiatti, R., Sassi, S., 1972. Découverte d'un témoin d'un volcanisme paléocène à éocène
1482 dans le bassin phosphaté de Métlaoui (Tunisie méridionale). CR Acad. Sci. Paris 324, 205–
1483 212.
1484 Cossa, 1878. Sur la diffusion de cerium, du lanthane et du didyme, extract of a letter from
1485 Cossa to Sella, presented by Frény. CR Acad. Sci. Paris 87, 378–388.
1486 Crouch, E.M., Heilmann-Clausen, C., Brinkhuis, H., Morgans, H.E.G., Rogers, K.M., Egger,
1487 H., Schmitz, B., 2001. Global dinoflagellate event associated with the late Paleocene
1488 thermal maximum. Geology 29, 315–318.
1489 Davis, J.C., 2002. Statistics and Data Analysis in Geology, 3rd edn. Wiley, New York, p. 656.
1490 DeBaar, H.J.W., Bacon, M.P., Brewer, P.G., Bruland, K.W., 1985. Rare-earth elements in the
1491 Pacific and Atlantic oceans. Geochim. Cosmochim. Acta 49, 1943–1959.
1492 Dooley, J.H., 2001. Baseline Concentrations of Arsenic, Beryllium and Associated Elements
1493 in Glauconite and Glauconitic Soils in the New Jersey Coastal Plain, Investigation Report.
1494 The New Jersey Geological Survey, Trenton NJ, p. 238.
1495 Dunkley Jones, T., Lunt, D.J., Schmidt, D.N., Ridgwell, A., Sluijs, A., Valdes, P.J., Maslin,
1496 M., 2013. Climate model and proxy data constraints on ocean warming across the
1497 Paleocene-Eocene Thermal Maximum. Earth-Sci. Rev. 125, 123–145.
1498 El Ayachi, M.S., Zagrarni, M.F., Snoussi, A., Bahrouni, N., Gzam, M., Ben Assi, I.,
1499 Hammami, K., Abdelli, H., Ben Rhaiem, H., 2016. The Paleocene–Lower Eocene series of
1500 the Gafsa basin (South-Central Tunisia): integrated stratigraphy and paleoenvironments.
1501 Arab. J. Geosci. 9, 395 doi: 10.1007/s12517-016-2403-0.
1502 Elderfield, H., Pagett, R., 1986. REE in ichthyoliths: variations with redox conditions and
1503 depositional environment. Sci. Total Environ. 49, 175–197.
1504 Elderfield, H., Upstillgoddard, R., Sholkovitz, E.R., 1990. The rare-earth elements in rivers,
1505 estuaries, and coastal seas and their significance to the composition of ocean waters.
1506 Geochim. Cosmochim. Acta 54, 971–991.
1507 Emsbo, P., McLaughlin, P.I., Breit, G.N., du Bray, E.A., Koenig, A.E., 2015. Rare earth
1508 elements in sedimentary phosphate deposits: Solution to the global REE crisis? Gondwana
1509 Res. 27, 776–785.
1510 Fauconnier, D., Slansky, M., 1980. Relation entre le developpement de dinoflagellés et la
1511 sédimentration phosphatée du bassin de Gafsa (Tunisie), Géologie Comparée des
1512 Gisements de Phosphates et de Pétrole. Doc. BRGM 24, 185–204.

Felhi, M., Tlili, A., Montacer, M., 2008. Geochemistry, petrography and spectroscopy of organic matter of clay-associated kerogen of Ypresian series: Gafsa-Metlaoui phosphatic basin, Tunisia. Resour. Geol 58, 428–436.

Ferreira da Silva, E., Mlayah, A., Gomes, C., Noronha, F., Charef, A., Sequeira, C., Esteves, V., Figueiredo Marques, A.R., 2010. Heavy elements in the phosphorite from Kalaat Khasba mine (north-western Tunisia): Potential implications on the environment and human health. J. Hazard. Mater. 182, 232–245.

Föllmi, K.B., 1996. The phosphorus cycle, phosphogenesis and marine phosphate-rich deposits. Earth-Sci. Rev. 40, 55–124.

Fournié, D., 1978. Nomenclature stratigraphique des séries de Crétacé supérieur au Tertiaire de Tunisie. Bull. Centre Rech. Explor.-Prod. Elf Aquitaine 2, 97–148.

Fournié, D., 1980. Phosphates et pétrole en Tunisie, Géologie Comparée des Gisements de Phosphates et de Pétrole. BRGM, Orléans, pp. 157–166.

Freslon, N., Bayon, G., Toucanne, S., Bermell, S., Bollinger, C., Cheron, S., Etoubleau, J., Germain, Y., Khripounoff, A., Ponzevera, E., Rouget, M.L., 2014. Rare earth elements and neodymium isotopes in sedimentary organic matter. Geochim. Cosmochim. Acta 140, 177–198.

Frieling, J., Iakovleva, A.I., Reichart, G.J., Aleksandrova, G.N., Gnibidenko, Z.N., Schouten, S., Sluijs, A., 2014. Paleocene–Eocene warming and biotic response in the epicontinental West Siberian Sea. Geology 42, 767–770.

Galai, H., Sliman, F., 2014. Mineral characterization of the Oum El Khacheb phosphorites (Gafsa-Metlaoui basin; S. Tunisia). Arab. J. Chem. doi:10.1016/j.arabjc.2014.10.007.

Galfati, I., Sassi, A.B., Zaier, A., Bouchardon, J.L., Bilal, E., Joron, J.L., Sassi, S., 2010. Geochemistry and mineralogy of Paleocene-Eocene Oum El Khecheb phosphorites (Gafsa-Metlaoui Basin) Tunisia. Geochem. J. 44, 189–210.

Gao, S., Liu, X., Yuan, H., Hattendorf, B., Günther, D., Chen, L., Hu, S., 2002. Determination of forty-two major and trace elements in USGS and NIST SRM glasses by laser ablation-inductively coupled plasma-mass spectrometry. Geostand. Geoanal. Res. 26, 181–196.

Garcia-Solsona, E., Jeandel, C., Labatut, M., Lacan, F., Vance, D., Chavagnac, V., Pradoux, C., 2014. Rare earth elements and Nd isotopes tracing water mass mixing and particle-seawater interactions in the SE Atlantic. Geochim. Cosmochim. Acta 125, 351–372.

Garnit, H., 2013. Pétrographie, minéralogie et géochimie des phosphorites et des minéralisations de Sr, Fe et Pb-Zn des bassins phosphatés en Tunisie. PhD thesis, Faculté des Sciences de Tunis, Université de Tunis El Manar, Tunis, p. 427.

1547 Garnit, H., Bouhlel, S., Barca, D., Chtara, C., 2012a. Application of LA-ICP-MS to
1548 sedimentary phosphatic particles from Tunisian phosphorite deposits: Insights from trace
1549 elements and REE into paleo-depositional environments. Chem Erde-Geochem. 72, 127–
1550 139.
1551 Garnit, H., Bouhlel, S., Barca, D., Johnson, C.A., Chtara, C., 2012b. Phosphorite-hosted zinc
1552 and lead mineralization in the Sekarna deposit (Central Tunisia). Mineral. Deposit. 47,
1553 545–562.
1554 Glenn, C.R., Arthur, M.A., 1990. Anatomy and origin of a Cretaceous phosphorite-greensand
1555 giant, Egypt. Sedimentology 37, 123–154.
1556 Glenn, C.R., Föllmi, K.B., Riggs, S.R., Baturin, G.N., Grimm, K.A., Trappe, J., Abed, A.M.,
1557 Galliolivier, C., Garrison, R.E., Ilyin, A.V., Jehl, C., Rohrlich, V., Sadaqah, R.M.Y.,
1558 Schidlowski, M., Sheldon, R.E., Siegmund, H., 1994. Phosphorus and phosphorites:
1559 sedimentology and environments of formation. Eclog. Geol. Helv. 87, 747–788.
1560 Grandjean, P., Cappeta, H., Michard, A., Albarède, F., 1987. The assessment of REE patterns
1561 and $^{143}Nd/^{144}Nd$ ratios in fish remains. Earth Planet. Sci. Lett. 84, 181–196.
1562 Gulbrandsen, R.A., 1966. Chemical composition of the phosphorites of the Phosphoria
1563 Formation. Geochim. Cosmochim. Acta 30, 769–778.
1564 Güler, C., Thyne, G.D., McCray, J.E., Turner, A.K., 2002. Evaluation of graphical and
1565 multivariate statistical methods for classification of water chemistry data. Hydrogeol. J. 10,
1566 455–474.
1567 Haji, T., Zouaghi, T., Boukadi, N., 2014. The role of inherited structures in the evolution of
1568 the Meknassy Basin, Central Tunisia, based on geological-geophysical transects. J. Afr.
1569 Earth Sci. 96, 51–59.
1570 Haley, B.A., Klinkhammer, G.P., McManus, J., 2004. Rare earth elements in pore waters of
1571 marine sediments. Geochim. Cosmochim. Acta 68, 1265–1279.
1572 Haq, B.U., Hardenbol, J., Vail, P.R., 1987. Chronology of fluctuating sea levels since the
1573 Triassic. Science 235, 1156–1167.
1574 Hein, J.R., Koschinsky, A., 2014. Deep-ocean ferromanganese crusts and nodules, in: Scott,
1575 S.D. (Ed.), Geochemistry of Mineral Deposits. Elsevier, Amsterdam, pp. 273–291.
1576 Hein, J.R., Koschinsky, A., Halliday, A.N., 2003. Global occurrence of tellurium-rich
1577 ferromanganese crusts and a model for the enrichment of tellurium. Geochim. Cosmochim.
1578 Acta 67, 1117–1127.
1579 Henchiri, M., 2007. Sedimentation, depositional environment and diagenesis of Eocene
1580 biosiliceous deposits in Gafsa basin (southern Tunisia). J. Afr. Earth Sci. 49, 187–200.

Herwartz, D., Tutken, T., Munker, C., Jochum, K.P., Stoll, B., Sander, P.M., 2011. Timescales and mechanisms of REE and Hf uptake in fossil bones. Geochim. Cosmochim. Acta 75, 82–105.

Hlaiem, A., Biju-Duval, B., Vially, R., Laatar, E., M'Rabet, A., 1997. Burial and thermal history modelling of the Gafsa-Metlaoui intracontinental Basin (southern Tunisia): Implications for petroleum exploration. J. Petrol. Geol. 20, 403–425.

Hughes, J.M., Rakovan, J.F., 2015. Structurally robust, chemically diverse: apatite and apatite supergroup minerals. Elements 11, 165–170.

Jarrar, G., Amireh, B., Zachmann, D., 2000. The major, trace and rare earth element geochemistry of glauconites from the early Cretaceous Kurnub Group of Jordan. Geochem. J. 34, 207–222.

Jarvis, I., 1984. Rare-earth element geochemistry of late Cretaceous chalks and phosphorites from northern France. Spec. Publ. Geol. Surv. India 17, 179–190.

Jarvis, I., 1992. Sedimentology, geochemistry and origin of phosphatic chalks: the Upper Cretaceous deposits of NW Europe. Sedimentology 39, 55–97.

Jarvis, I., Jarvis, K.E., 1985. Rare-earth element geochemistry of standard sediments: a study using inductively coupled plasma spectrometry. Chem. Geol. 53, 335–344.

Jarvis, I., Burnett, W.C., Nathan, Y., Almbaydin, F.S.M., Attia, A.K.M., Castro, L.N., Flicoteaux, R., Hilmy, M.E., Husain, V., Qutawnah, A.A., Serjani, A., Zanin, Y.N., 1994. Phosphorite geochemistry: state-of-the-art and environmental concerns. Eclog. Geol. Helv. 87, 643–700.

Jasinski, S.M., 2011. Phosphate Rock, Mineral Commodity Summary, January 2011. U.S. Department of the Interior, U.S. Geological Survey http://minerals.usgs.gov/minerals/pubs/commodity/phosphate_rock/mcs-2011-phosp.pdf.

Jasinski, S.M., 2017. Phosphate Rock, Mineral Commodity Summaries. United States Geological Survey https://minerals.usgs.gov/minerals/pubs/commodity/phosphate_rock/mcs-2017-phosp.pdf.

Johan, Z., 1988. Indium and germanium in the structure of sphalerite - an example of coupled substitution with copper. Mineral. Petrol. 39, 211–229.

Johannesson, K.H., Burdige, D.J., 2007. Balancing the global oceanic neodymium budget: Evaluating the role of groundwater. Earth Planet. Sci. Lett. 253, 129–142.

Kaiser, H.F., 1960. The application of electronic computers to factor analysis. Educ. Psychol. Meas. 20, 141–151.

1614 Kieft, K., Damman, A.H., 1990. Indium-bearing chalcopyrite and sphalerite from the Gasborn
1615 area, West Bergslagen, central Sweden. Min. Mag. 54, 109–112.
1616 Kiehl, J.T., Shields, C.A., 2013. Sensitivity of the Palaeocene–Eocene Thermal Maximum
1617 climate to cloud properties. Phil. Trans. Roy. Soc. A – Math. Phys. Eng. Sci. 371.
1618 Kocsis, L., Trueman, C.N., Palmer, M.R., 2010. Protracted diagenetic alteration of REE
1619 contents in fossil bioapatites: Direct evidence from Lu-Hf isotope systematics. Geochim.
1620 Cosmochim. Acta 74, 6077–6092.
1621 Kocsis, L., Ounis, A., Chaabani, F., Salah, N.M., 2013. Paleoenvironmental conditions and
1622 strontium isotope stratigraphy in the Paleogene Gafsa Basin (Tunisia) deduced from
1623 geochemical analyses of phosphatic fossils. Internat. J. Earth Sci. 102, 1111–1129.
1624 Kocsis, L., Ounis, A., Baumgartner, C., Pirkenseer, C., Harding, I.C., Adatte, T., Chaabani,
1625 F., Neili, S.M., 2014. Paleocene–Eocene palaeoenvironmental conditions of the main
1626 phosphorite deposits (Chouabine Formation) in the Gafsa Basin, Tunisia. J. Afr. Earth Sci.
1627 100, 586–597.
1628 Kocsis, L., Gheerbrant, E., Mouflih, M., Cappetta, H., Ulianov, A., Chiaradia, M., Bardet, N.,
1629 2016. Gradual changes in upwelled seawater conditions (redox, pH) from the late
1630 Cretaceous through early Paleogene at the northwest coast of Africa: Negative Ce anomaly
1631 trend recorded in fossil bio-apatite. Chem. Geol. 421, 44–54.
1632 Kominz, M.A., Browning, J.V., Miller, K.G., Sugarman, P.J., Mizintseva, S., Scotese, C.R.,
1633 2008. Late Cretaceous to Miocene sea-level estimates from the New Jersey and Delaware
1634 coastal plain coreholes: an error analysis. Basin Res. 20, 211–226.
1635 Kon, Y., Hoshino, M., Sanematsu, K., Morita, S., Tsunematsu, M., Okamoto, N., Yano, N.,
1636 Tanaka, M., Takagi, T., 2014. Geochemical characteristics of apatite in heavy REE-rich
1637 deep-sea mud from Minami-Torishima area, southeastern Japan. Resour. Geol 64, 47–57.
1638 Kostova, B.V., Petrova, N.L., Petkova, V., 2013. The high energy milling effect on positional
1639 redistribution of CO_3^- ions in the structure of sedimentary apatite. Bulg. Chem. Comm. 45,
1640 601–606.
1641 Labs-Hochstein, J., MacFadden, B.J., 2006. Quantification of diagenesis in Cenozoic sharks:
1642 Elemental and mineralogical changes. Geochim. Cosmochim. Acta 70, 4921–4932.
1643 Lécuyer, C., Grandjean, P., Barrat, J.A., Nolvak, J., Emig, C., Paris, F., Robardet, M., 1998.
1644 $\delta^{18}O$ and REE contents of phosphatic brachiopods: a comparison between modern and
1645 lower Paleozoic populations. Geochim. Cosmochim. Acta 62, 2429–2436.
1646 Lin, I., Schorr, M., 1997. A challenge for the phosphate industry: Cd removal. Phosphorus
1647 Potassium 208, 27–32.

1648 Little, S.H., Vance, D., Lyons, T.W., McManus, J., 2015. Controls on trace metal authigenic
1649 enrichment in reducing sediments: insights from modern oxygen-deficient settings. Am. J.
1650 Sci. 315, 77–119.
1651 Liu, Y., Peng, Z.C., Wei, G.J., Chen, T.G., Sun, W.D., He, J.F., Liu, G.J., Chou, C.L., Shen,
1652 C.C., 2011. Interannual variation of rare earth element abundances in corals from northern
1653 coast of the South China Sea and its relation with sea-level change and human activities.
1654 Mar. Env. Res. 71, 62–69.
1655 Lucas, J., Prévôt-Lucas, L., 1996. Tethyan phosphates and bioproductites, in: Nairn, A.E.M.,
1656 Ricou, L.-E., Vrielynck, B., Dercourt, J. (Eds.), The Ocean Basins and Margins, Vol. 8.
1657 The Tethys Ocean. Plenum Press, New York, pp. 367–391.
1658 Martin, E.E., Scher, H.D., 2004. Preservation of seawater Sr and Nd isotopes in fossil fish
1659 teeth: bad news and good news. Earth Planet. Sci. Lett. 220, 25–39.
1660 McArthur, J.M., 1978. Systematic variations in the contents of Na, Sr, CO_2 and SO_4 in marine
1661 carbonate fluorapatite and their relation to weathering. Chem. Geol. 21, 41–52.
1662 McArthur, J.M., 1985. Francolite geochemistry - compositional controls during formation,
1663 diagenesis, metamorphism and weathering. Geochim. Cosmochim. Acta 49, 23–35.
1664 McArthur, J.M., Walsh, J.N., 1984. Rare-earth geochemistry of phosphorites. Chem. Geol.
1665 47, 191–220.
1666 McClellan, G.H., 1980. Mineralogy of carbonate fluorapatites. J. Geol. Soc. London 137,
1667 675–681.
1668 McConnell, D., 1973. Apatite - Its Crystal Chemistry, Mineralogy, Utilization, and Geologic
1669 and Biologic Occurrences. Springer Verlag, Vienna, p. 111.
1670 McInerney, F.A., Wing, S.L., 2011. The Paleocene–Eocene Thermal Maximum: a
1671 perturbation of carbon cycle, climate, and biosphere with implications for the future, in:
1672 Jeanloz, R., Freeman, K.H. (Eds.), Ann. Rev. Earth Planet. Sci. 39, 489–516.
1673 McKelvey, V.E., 1950. Rare earths in Western Phosphate rocks, US Geol. Surv. Trace
1674 Element Mem., US Geological Survey, p. 6.
1675 McKelvey, V.E., Swanson, R.W., Sheldon, R.P., 1953. The Permian phosphorite deposits of
1676 the Western United States, in: Saint Guilhem, M.R. (Ed.), Origine des Gisements de
1677 Phosphates de Chaux. 19th International Geological Congress, Algiers, pp. 45–64.
1678 McLennan, S.M., 1989. Rare earth elements in sedimentary rocks: influence of provenance
1679 and sedimentary processes, in: Lipin, B.R., McKay, G.A. (Eds.), Geochemistry and
1680 Mineralogy of Rare Earth Elements. Mineralogical Society of America pp. 169–200.

1681 Meglen, R.R., 1992. Examining large databases - a chemometric approach using principal
1682 component analysis. Mar. Chem. 39, 217–237.
1683 Messadi, A.M., Mardassi, B., Ouali, J.A., Touir, J., 2016. Sedimentology, diagenesis, clay
1684 mineralogy and sequential analysis model of Upper Paleocene evaporite-carbonate ramp
1685 succession from Tamerza area (Gafsa Basin: Southern Tunisia). J. Afr. Earth Sci. 118,
1686 205–230.
1687 Miller, K.G., Kominz, M.A., Browning, J.V., Wright, J.D., Mountain, G.S., Katz, M.E.,
1688 Sugarman, P.J., Cramer, B.S., Christie-Blick, N., Pekar, S.F., 2005. The Phanerozoic
1689 record of global sea-level change. Science 310, 1293–1298.
1690 Millot, G., 1970. Geology of Clays: Weathering, Sedimentology, Geochemistry. Springer-
1691 Verlag, New York, p. 429.
1692 Moody, R.T.J., 1987. The Ypresian carbonates of Tunisia - a model of foraminiferal facies
1693 distribution, in: Hart, M.B. (Ed.), Micropaleontology of Carbonate Environments. Ellis
1694 Horwood for The British Micropalaeontological Society, Chichester, pp. 82–92.
1695 Moody, R.T.J., Grant, G.G., 1989. On the importance of bioclasts in the definition of
1696 depositional model for the Metlaoui carbonate group, Actes des IIème Journées de
1697 Géologie Tunisienne Appliquée à la Recherche des Hydrocarbures. L'Entreprise
1698 Tunisienne d'Activités Pétrolières, Tunis, pp. 409–427.
1699 Moreda-Pineiro, A., Marcos, A., Fisher, A., Hill, S.J., 2001. Evaluation of the effect of data
1700 pre-treatment procedures on classical pattern recognition and principal components
1701 analysis: a case study for the geographical classification of tea. J. Env. Mon. 3, 352–360.
1702 Müller, R.D., Sdrolias, M., Gaina, C., Steinberger, B., Heine, C., 2008. Long-term sea-level
1703 fluctuations driven by ocean basin dynamics. Science 319, 1357–1362.
1704 Nathan, Y., 1984. The mineralogy and geochemistry of phosphorites, in: Nriagu, J.O., Moore,
1705 P.B. (Eds.), Phosphate Minerals. Springer Verlag, Berlin, pp. 275–291.
1706 Nathan, Y., Benalioulhaj, N., Prévôt, L., Lucas, J., 1996. The geochemistry of cadmium in the
1707 phosphate-rich and organic-rich sediments of the Oulad-Abdoun and Timahdit basins
1708 (Morocco). J. Afr. Earth Sci. 22, 17–27.
1709 Nathan, Y., Soudry, D., Levy, Y., Shitrit, D., Dorfman, E., 1997. Geochemistry of cadmium
1710 in the Negev phosphorites. Chem. Geol. 142, 87–107.
1711 Notholt, A.J.G., 1980. Economic phosphatic sediments - mode of occurrence and
1712 stratigraphical distribution. J. Geol. Soc. London 137, 793–805.
1713 Notholt, A.J.G., Sheldon, R.P., Davidson, D.F., 1989. Phosphate Deposits of the World 2:
1714 Phosphate Rock Resources. Cambridge University Press, Cambridge, p. 566.

1715 Osborne, A.H., Haley, B.A., Hathorne, E.C., Plancherel, Y., Frank, M., 2015. Rare earth
1716 element distribution in Caribbean seawater: continental inputs versus lateral transport of
1717 distinct REE compositions in subsurface water masses. Mar. Chem. 177, 172–183.
1718 Ounis, A., 2011. Apport de la géochimie des terres rares et des isotopes pour la
1719 compréhension des mécanismes de la phosphatogenèse: exemple de la partie occidentale
1720 du bassin de Gafsa-Métlaoui. PhD thesis, Faculté des Sciences de Tunis, Université de
1721 Tunis El Manar, Tunis, p. 198.
1722 Ounis, A., Kocsis, L., Chaabani, F., Pfeifer, H.-R., 2008. Rare earth elements and stable
1723 isotope geochemistry ($\delta^{13}C$ and $\delta^{18}O$) of phosphorite deposits in the Gafsa Basin, Tunisia.
1724 Palaeogeogr. Palaeoclimatol. Palaeoecol. 268, 1–18.
1725 Palmer, M.R., Elderfield, H., 1986. Rare-earth elements and neodymium isotopes in
1726 ferromanganese oxide coatings of Cenozoic foraminifera from the Atlantic Ocean.
1727 Geochim. Cosmochim. Acta 50, 409–417.
1728 Pattrick, R.A.D., Dorling, M., Polya, D.A., 1993. TEM study of indium-bearing and copper-
1729 bearing growth-banded sphalerite. Can. Mineral. 31, 105–117.
1730 Paytan, A., 2009. Ocean paleoproductivity, in: Gornitz, V. (Ed.), Encyclopedia of
1731 Paleoclimatology and Ancient Environments. Springer, Netherlands, pp. 644–651.
1732 Perthuisot, V., 1981. Diapirism in northern Tunisia. J. Struct. Geol. 3, 231–235.
1733 Pervinquière, L., 1903. Étude Géologique de la Tunisie Centrale. Direction Générale des
1734 Travaux Publics, Carte Géologique de la Tunisie, F.R. de Rudeval, Paris, p. 359.
1735 Prévôt, L., 1990. Geochemistry, petrography, genesis of Cretaceous–Eocene phosphorites.
1736 Mém. Soc. géol. Fr. 158, p. 232.
1737 Raiswell, R., Canfield, D.E., 1998. Sources of iron for pyrite formation in marine sediments.
1738 Am. J. Sci. 298, 219–245.
1739 Rempfer, J., Stocker, T.F., Joos, F., Dutay, J.C., Siddall, M., 2011. Modelling Nd-isotopes
1740 with a coarse resolution ocean circulation model: sensitivities to model parameters and
1741 source/sink distributions. Geochim. Cosmochim. Acta 75, 5927–5950.
1742 Reynard, B., Lécuyer, C., Grandjean, P., 1999. Crystal-chemical controls on rare-earth
1743 element concentrations in fossil biogenic apatites and implications for paleoenvironmental
1744 reconstructions. Chem. Geol. 155, 233–241.
1745 Robert, C., Chamley, H., 1991. Development of early Eocene warm climates, as inferred from
1746 clay mineral variations in oceanic sediments. Glob. Planet. Change 89, 315–331.

1747 Rosenthal, Y., Lam, P., Boyle, E.A., Thomson, J., 1995. Authigenic cadmium enrichments in
1748 suboxic sediments - precipitation and postdepositional mobility. Earth Planet. Sci. Lett.
1749 132, 99–111.
1750 Saïd, A., Baby, P., Chardon, D., Ouali, J., 2011. Structure, paleogeographic inheritance, and
1751 deformation history of the southern Atlas foreland fold and thrust belt of Tunisia.
1752 Tectonics 30, doi: 10.1029/2011tc002862.
1753 Sandell, E.B., Hey, M.H., McConnell, D., 1939. The composition of francolite. Min. Mag. 25,
1754 395–401.
1755 Sassi, S., 1974. La sédimentation phosphatée au Paléocène dans le Sud et le Centre Ouest de
1756 la Tunisie. Thèse de Doctorat ès Sciences, Université de Paris Sud Orsay, France, p. 300.
1757 Sassi, S., 1980. Contexte paléogeographique des dépôts phosphatés de l'Eocene de Tunisie,
1758 Géologie Comparée des Gisements de Phosphates et de Pétrole. BRGM, Orléans, pp. 167–
1759 183.
1760 Schoonen, M.A.A., 2004. Mechanisms of sedimentary pyrite formation, in: Amend, J.P.,
1761 Edwards, K.J., Lyons, T.W. (Eds.), Sulfur Biogeochemistry - Past and Present. Geological
1762 Society of America, Boulder, Colorado, pp. 117–134.
1763 Schuffert, J.D., Kastner, M., Emanuele, G., Jahnke, R.A., 1990. Carbonate-ion substitution in
1764 francolite: a new equation. Geochim. Cosmochim. Acta 54, 2323–2328.
1765 Shackleton, N.J., and Kennett, J.P., 1975. Paleotemperature history of the Cenozoic and the
1766 initiation of Antarctic glaciation: Oxygen and carbon isotope analyses in DSDP sites 277,
1767 279, and 281. Initial Rep. DSDP 29, 743–755.
1768 Shaw, H.F., Wasserburg, G.J., 1985. Sm-Nd in marine carbonates and phosphorites:
1769 implications for Nd isotopes in seawater and crustal ages. Geochim. Cosmochim. Acta 49,
1770 503–518.
1771 Sheldon, R.P., 1987. Association of phosphatic and siliceous marine sedimentary deposits, in:
1772 Hein, J.R. (Ed.), Siliceous Sedimentary Rock-hosted Ores and Petroleum. Van Norstrand
1773 Reinhold Co, New York, pp. 58–80.
1774 Shields, G., Stille, P., 2001. Diagenetic constraints on the use of cerium anomalies as
1775 palaeoseawater redox proxies: an isotopic and REE study of Cambrian phosphorites.
1776 Chem. Geol. 175, 29–48.
1777 Shimizu, H., Tachikawa, K., Masuda, A., Nozaki, Y., 1994. Cerium and neodymium isotope
1778 ratios and REE patterns in seawater from the North Pacific Ocean. Geochim. Cosmochim.
1779 Acta 58, 323–333.

1780 Sholkovitz, E., Shen, G.T., 1995. The incorporation of rare-earth elements in modern coral.
1781 Geochim. Cosmochim. Acta 59, 2749–2756.
1782 Sluijs, A., Schouten, S., Pagani, M., Woltering, M., Brinkhuis, H., Damste, J.S.S., Dickens,
1783 G.R., Huber, M., Reichart, G.J., Stein, R., Matthiessen, J., Lourens, L.J., Pedentchouk, N.,
1784 Backman, J., Moran, K., Expedition, S., 2006. Subtropical arctic ocean temperatures
1785 during the Palaeocene/Eocene thermal maximum. Nature 441, 610–613.
1786 Sluijs, A., Brinkhuis, H., Crouch, E.M., John, C.M., Handley, L., Munsterman, D., Bohaty,
1787 S.M., Zachos, J.C., Reichart, G.J., Schouten, S., Pancost, R.D., Damste, J.S.S., Welters,
1788 N.L.D., Lotter, A.F., Dickens, G.R., 2008. Eustatic variations during the Paleocene–
1789 Eocene greenhouse world. Paleoceanography 23, doi: 10.1029/2008pa001615.
1790 Sluijs, A., van Roij, L., Harrington, G.J., Schouten, S., Sessa, J.A., Levay, L.J., Reichart, G.J.,
1791 Slomp, C.P., 2014. Warming, euxinia and sea level rise during the Paleocene–Eocene
1792 Thermal Maximum on the Gulf Coastal Plain: implications for ocean oxygenation and
1793 nutrient cycling. Climate Past 10, 1421–1439.
1794 Smaill, J.B., 2015. Geochemical variations in glauconitic minerals: applications as a
1795 potassium fertiliser resource. MSc thesis, Department of Geological Sciences, University
1796 of Canterbury, Christchurch NZ, p. 122.
1797 Soudry, D., Nathan, Y., 2001. Diagenetic trends of fluorine concentration in Negev
1798 phosphorites, Israel: implications for carbonate fluorapatite composition during
1799 phosphogenesis. Sedimentology 48, 723–743.
1800 Soudry, D., Glenn, C.R., Nathan, Y., Segal, I., VonderHaar, D., 2006. Evolution of Tethyan
1801 phosphogenesis along the northern edges of the Arabian-African shield during the
1802 Cretaceous–Eocene as deduced from temporal variations of Ca and Nd isotopes and rates
1803 of P accumulation. Earth-Sci. Rev. 78, 27–57.
1804 Sweere, T., van den Boorn, S., Dickson, A.J., Reichart, G.J., 2016. Definition of new trace-
1805 metal proxies for the controls on organic matter enrichment in marine sediments based on
1806 Mn, Co, Mo and Cd concentrations. Chem. Geol. 441, 235-245.
1807 Thomas, P., 1885. Sur la découverte de gisements de phosphate du chaux dans le sud de la
1808 Tunisie. Comptes Rendus de l'Academie des Sciences Paris 101, 1184.
1809 Tlili, A., Felhi, M., Montacer, M., 2010. Origin and depositional environment of palygorskite
1810 and sepiolite from the Ypresian phosphatic series, southewestern Tunisia. Clays Clay Min.
1811 58, 573–584.

1812 Tlili, A., Felhi, M., Fattah, N., Montacer, M., 2011. Mineralogical and geochemical studies of
1813 Ypresian marly clays and silica rocks of phosphatic series, Gafsa-Metlaoui basin,
1814 southwestern Tunisia: implication for depositional environment. Geosci. J. 15, 53–64.
1815 Tóth, E., Weiszburg, T.G., Jeffries, T., Williams, C.T., Bartha, A., Bertalan, E., Cora, I.,
1816 2010. Submicroscopic accessory minerals overprinting clay mineral REE patterns
1817 (celadonite-glauconite group examples). Chem. Geol. 269, 312–328.
1818 Tribovillard, N., Algeo, T.J., Lyons, T., Riboulleau, A., 2006. Trace metals as paleoredox and
1819 paleoproductivity proxies: an update. Chem. Geol. 232, 12–32.
1820 Tribovillard, N., Algeo, T.J., Baudin, F., Riboulleau, A., 2012. Analysis of marine
1821 environmental conditions based on molybdenum-uranium covariation - applications to
1822 Mesozoic paleoceanography. Chem. Geol. 324, 46–58.
1823 Trichet, J.G., Rachidi, M., Belayouni, H., 1990. Organic geochemistry of phosphorites:
1824 relative behaviours of phosphorus and nitrogen during the formation of humic compounds
1825 in phosphate-bearing sequences, in: Burnett, W.C., Riggs, S.R. (Eds.), Phosphate Deposits
1826 of the Word Volume 3: Neogene to Modern Phosphorites. Cambridge University Press,
1827 Cambridge, pp. 87–97.
1828 Trueman, C.N., Kocsis, L., Palmer, M.R., Dewdney, C., 2011. Fractionation of rare earth
1829 elements within bone mineral: A natural cation exchange system. Palaeogeogr.
1830 Palaeoclimatol. Palaeoecol. 310, 124–132.
1831 Tunis-Afrique-Press, 2016. Tunisia: study on phosphate extraction project in Sra Ouertane to
1832 be developed soon. http://allafrica.com/stories/201505280745.html, accessed 14 June
1833 2016.
1834 Vandenberghe, N., Hilgen, F.J., Speijer, R.P., Ogg, J.G., Gradstein, F.M., Hammer, O.,
1835 Hollis, C.J., Hooker, J.J., 2012. The Paleogene Period, in: Gradstein, F.M., Ogg, J.G.,
1836 Schmitz, M., Ogg, G. (Eds.), The Geologic Time Scale 2012. Elsevier, Amsterdam, pp.
1837 855–921.
1838 Webb, G.E., Kamber, B.S., 2000. Rare earth elements in Holocene reefal microbialites: a new
1839 shallow seawater proxy. Geochim. Cosmochim. Acta 64, 1557–1565.
1840 Wedepohl, K.H., 1971. Environmental influences on the chemical composition of shales and
1841 clays, in: Ahrens, L.H., Press, F., Runcorn, S.K., Urey, H.C. (Eds.), Physics and Chemistry
1842 of the Earth. Pergamon, Oxford, pp. 307–333.
1843 Wedepohl, K.H., 1991. The composition of the upper Earth's crust and the natural cycles of
1844 selected metals. Metals in natural raw materials. Natural Resources., in: Merian, E. (Ed.),
1845 Metals and Their Compounds in the Environment. VCH, Weinheim, pp. 3–17.

1846 Winnock, E., 1980. Les dépôts de l'Eocene au Nord de l'Afrique: aperçu paléogéographique
1847 de l'ensemble, Géologie Comparée des Gisements de Phosphates et de Pétrole. BRGM,
1848 Orléans, pp. 219–243.
1849 Wyndham, T., McCulloch, M., Fallon, S., Alibert, C., 2004. High-resolution coral records of
1850 rare earth elements in coastal seawater: biogeochemical cycling and a new environmental
1851 proxy. Geochim. Cosmochim. Acta 68, 2067–2080.
1852 Yunker, M.B., Macdonald, R.W., Veltkamp, D.J., Cretney, W.J., 1995. Terrestrial and marine
1853 biomarkers in a seasonally ice-covered Arctic estuary - integration of multivariate and
1854 biomarker approaches. Mar. Chem. 49, 1–50.
1855 Yunker, M.B., Belicka, L.L., Harvey, H.R., Macdonald, R.W., 2005. Tracing the inputs and
1856 fate of marine and terrigenous organic matter in Arctic Ocean sediments: A multivariate
1857 analysis of lipid biomarkers. Deep-Sea Res. Part Ii - Topical Studies in Oceanography 52,
1858 3478–3508.
1859 Zachos, J., Pagani, M., Sloan, L., Thomas, E., Billups, K., 2001. Trends, rhythms, and
1860 aberrations in global climate 65 Ma to present. Science 292, 686–693.
1861 Zachos, J.C., Dickens, G.R., Zeebe, R.E., 2008. An early Cenozoic perspective on greenhouse
1862 warming and carbon-cycle dynamics. Nature 451, 279–283.
1863 Zaïer, A., 1999. Evolution tectono-sédimentaire du bassin phosphate du centre-ouest de la
1864 Tunisie minéralogie, pétrographie, géochimie et genèse des phosphorites. Thèse de
1865 Doctorat ès Sciences, Université de Tunis II.
1866 Zaïer, A., Béji-Sassi, A., Sassi, S., Moody, R.T.J., 1998. Basin evolution and deposition
1867 during the Early Paleocene in Tunisia, in: Macgregor, D.S., Moody, R.T.J., Clark-Lowes,
1868 D.D. (Eds.), Petroleum Geology of North Africa. Geol. Soc. London Spec. Publ. 132, 375–
1869 393.
1870 Zaky, A.H., Brand, U., Azmy, K., 2015. A new sample processing protocol for procuring
1871 seawater REE signatures in biogenic and abiogenic carbonates. Chem. Geol. 416, 36–50.
1872 Zargouni, F., 1985. Tectonique de l'atlas méridional de Tunisie: évolution géométrique et
1873 cinématique des structures en zone de cisaillement. Thèse de doctorat es-Sciences,
1874 Université Louis Pasteur, Strasbourg, p. 300.
1875

Table 1. Concentrations of major elements (wt%), trace elements and rare-earth elements (ppm), and elemental ratios in 58 phosphorite samples from the three phosphorite basins of Tunisia.

Basin	Northern Basins												Eastern Basins							Gafsa-Metlaoui Basin							
Deposit	Sra Ouertane (locality 1)									Sekarna (locality 2)			Jebel Jebs (locality 3)							Naguess (locality 4)							
Samples	SRO1	SRO2	SRO3	SRO4	SRO5	SRO6	SRO7	SRO8	SRO9	SEK1	SEK3	SEK4	JBS4	JBS5	JBS10	JBS7	JBS14	JBS18	JBS19	NAGI	NAGIIa	NAGIIb	NAGIII	NAGIV	NAGV	NAGVI	NAGVII and VIII
Major oxides (%)																											
SiO_2	21.37	13.22	8.35	9.18	7.42	10.86	13.26	8.23	9.46	18.20	22.45	9.31	31.47	29.01	12.13	15.50	15.72	7.26	6.52	9.23	3.98	7.40	5.44	14.56	21.96	5.79	3.35
TiO_2	0.170	0.129	0.062	0.081	0.089	0.078	0.159	0.039	0.035	0.041	0.050	0.036	0.145	0.064	0.098	0.128	0.037	0.064	0.082	0.065	0.032	0.046	0.040	0.029	0.021	0.033	0.030
Al_2O_3	3.41	1.70	1.36	1.63	1.90	1.90	2.63	0.68	0.48	1.22	1.21	0.88	2.11	1.09	0.98	1.72	0.70	1.33	1.81	1.62	0.74	1.09	0.91	0.70	0.43	0.76	0.67
Fe_2O_3(T)	1.06	0.44	0.70	0.66	0.82	0.68	0.86	0.46	0.42	2.17	1.99	1.69	0.69	0.45	0.41	0.46	0.53	0.67	0.87	0.59	0.29	0.45	0.40	0.16	0.21	0.34	0.31
MnO	0.011	0.009	0.008	0.011	0.007	0.005	0.005	0.002	0.008	0.025	0.015	0.023	0.006	0.005	0.006	0.007	0.003	0.003	0.004	0.003	0.004	0.004	0.004	0.003	0.002	0.003	0.002
MgO	0.64	0.57	1.38	2.07	0.89	1.09	0.75	0.24	0.23	3.88	2.43	5.12	7.88	5.47	12.08	12.63	0.45	0.77	1.05	0.50	0.47	0.65	0.60	0.48	0.39	0.60	0.63
CaO	38.93	44.25	46.57	45.56	48.23	45.74	44.55	48.60	48.33	38.76	38.18	42.35	24.79	30.80	32.72	30.10	42.70	44.84	44.91	44.53	48.49	45.56	46.95	43.59	39.04	47.31	49.22
Na_2O	0.54	0.23	0.30	0.24	0.13	0.41	0.15	0.52	0.45	0.41	0.48	0.42	0.70	0.87	0.68	0.53	1.45	1.72	1.68	1.29	1.30	1.27	1.36	1.35	1.22	1.44	1.39
K_2O	0.91	0.37	0.39	0.39	0.32	0.58	0.49	0.20	0.11	0.50	0.45	0.39	1.47	0.72	0.64	1.20	0.33	0.37	0.68	0.69	0.17	0.18	0.13	0.08	0.06	0.11	0.12
P_2O_5	7.74	10.50	10.44	4.66	5.81	8.81	3.78	26.12	21.94	19.73	23.77	19.14	8.83	14.32	9.17	6.70	27.86	29.44	28.80	26.76	27.72	26.10	28.05	26.76	23.93	28.90	28.99
SO_3	0.69	0.89	2.37	0.64	0.23	0.36	0.20	0.89	0.97	0.92	1.35	3.00	nd	2.41	nd	1.75	3.55	4.74	4.47	3.00	3.10	4.09	3.75	2.65	2.13	3.50	4.42
LOI	25.09	27.11	27.69	34.04	33.90	29.03	33.73	13.13	17.69	13.74	9.06	19.02	19.64	16.17	28.87	29.48	9.97	10.80	11.19	11.41	11.74	13.28	12.11	11.60	11.07	11.69	11.44
Total	100.57	99.42	99.62	99.16	99.75	99.55	100.57	99.11	100.12	99.60	101.44	101.38	97.73	101.38	97.78	100.20	103.30	102.01	102.07	99.68	98.03	100.12	99.74	101.96	100.47	100.47	100.57
Francolite[1] (%)	22	30	30	13	17	25	11	75	63	57	69	55	25	41	26	19	80	85	83	77	80	75	81	77	69	83	84
CaO/P_2O_5	5.03	4.21	4.46	9.78	8.30	5.19	11.79	1.86	2.20	1.96	1.61	2.21	2.81	2.15	3.57	4.49	1.53	1.52	1.56	1.66	1.75	1.75	1.67	1.63	1.63	1.64	1.70
SO_3/P_2O_5	0.09	0.09	0.23	0.14	0.04	0.04	0.05	0.03	0.04	0.05	0.06	0.16	nd	0.17	nd	0.26	0.13	0.16	0.16	0.11	0.11	0.16	0.13	0.10	0.09	0.12	0.15
Trace elements (ppm)																											
As	7.5	< 0.5	7.4	5.1	3.0	3.4	8.3	8.4	7.4	18.7	37.2	37.6	10.8	5.6	< 0.5	< 0.5	9.6	6.7	11.8	5.1	< 0.5	3.5	< 0.5	< 0.5	< 0.5	< 0.5	< 0.5
Ba	92	50	61	45	30	73	34	66	68	45	99	89	64	62	79	78	37	44	42	44	33	34	33	33	24	28	26
Br	6.2	10.3	5.3	4.1	< 0.5	6.1	4.3	14.0	12.0	6.8	4.8	4.1	20.3	7.6	25.8	9.5	14.8	15.5	16.5	8.5	6.7	7.7	8.2	9.1	9.5	10.8	10.0
Cd	11.7	4.8	23.3	10.2	13.4	24.2	28.2	15.9	19.1	5.6	2.9	0.8	nd	8.8	nd	9.3	54.8	46.7	13.1	48.7	37.3	168	97.6	3.3	172	28.0	32.5
Cr	214	242	159	126	104	173	211	194	246	297	305	287	149	140	110	101	209	266	239	253	202	246	251	287	230	277	218
Cu	11	38	24	6	4	23	27	27	36	15	16	13	10	6	10	2	12	15	11	9	8	14	10	7	7	6	11
Hf	1.5	1.2	0.5	0.6	0.6	0.9	1.4	1.0	0.6	0.7	0.8	1.2	1.6	0.8	0.9	1.6	0.6	0.7	0.7	0.8	0.4	0.4	0.4	0.4	0.3	0.4	0.3
Mo	5	4	9	7	5	7	< 2	< 2	2	11	31	25	9	6	4	3	5	11	15	8	6	8	5	5	3	3	25
Nb	8	5	3	4	3	4	6	2	1	1	2	1	7	3	5	7	1	2	3	2	1	2	1	< 1	< 1	1	1
Ni	26	37	18	16	12	13	49	37	53	64	85	58	20	16	20	6	15	19	19	16	11	29	17	6	13	16	22
Rb	15	8	9	8	9	10	12	4	2	12	11	9	10	5	5	7	3	5	7	7	3	5	4	3	< 2	3	3
Sb	1.0	0.9	1.1	0.8	0.6	0.8	1.4	1.6	1.2	2.8	4.9	5.4	1.5	1.4	< 0.2	0.7	2.1	1.0	2.9	0.8	0.8	0.5	0.4	0.5	< 0.2	< 0.2	0.5
Sc	4.4	5.5	3.1	2.7	2.9	3.6	4.1	8.6	6.6	6.3	4.6	4.7	3.4	2.3	3.0	2.1	4.2	5.5	5.3	5.0	4.1	4.0	4.5	3.3	2.3	3.0	2.3
Sr	743	801	836	722	717	776	533	1400	1250	539	573	693	753	1010	693	727	2160	2220	2220	1790	1850	1730	1930	1900	1710	2030	1970
Th	4.3	3.4	5.5	2.2	10.1	7.3	2.1	6.6	3.4	9.3	9.7	5.5	5.1	6.5	6.6	5.4	29.2	26.6	24.4	14.5	10.0	9.3	13.8	6.7	3.1	5.3	4.4
U	19.3	34.5	22.6	10.9	14.6	23.3	27.1	112.0	73.9	36.2	55.0	47.8	17.4	31.8	17.4	14.6	46.7	44.7	40.8	30.6	30.5	28.6	25.4	28.6	42.2	38.8	44.2
V	58	91	37	33	42	50	221	89	67	254	164	183	33	63	30	28	78	79	93	42	30	46	33	106	122	64	98
Y	91	148	108	51	90	118	55	402	251	299	316	251	77	121	80	63	249	235	215	139	122	139	152	107	89	91	97
Zn	99	87	116	62	43	61	153	125	122	84	33	13	210	66	30	24	399	381	118	260	120	854	429	54	903	163	197
Zr	74	56	34	32	29	41	66	48	35	34	41	28	76	48	52	84	43	43	43	50	44	37	36	32	25	37	27
Rare-earth elements (ppm)																											
La	59.2	76.6	69.0	31.4	71.4	82.0	31.8	213	128	184	186	155	57.2	87.5	65.8	51.3	221	213	203	111	86.6	93.6	110	75.9	55.1	60.6	52.5
Ce	57.8	48.7	75.8	31.2	106	93.5	23.5	114	68.5	195	213	152	76.7	116	96.7	76.6	354	335	331	180	120	122	168	108	59.3	82.3	65.5
Pr	11.3	13.2	14.1	6.1	17.0	17.3	5.5	34.1	19.3	38.9	41.9	30.5	11.8	18.2	14.6	11.4	52.4	49.3	47.7	24.9	18.0	19.2	24.4	15.7	9.8	12.0	10.0
Nd	46.8	56.1	59.1	25.5	70.8	71.8	23.0	147.0	82.0	167	182	130	49.2	75.9	60.0	47.4	215	204	198	103	74.1	79.3	101	64.3	39.2	49.4	41.6
Sm	9.4	11.5	12.1	5.1	14.5	14.8	4.7	29.8	16.1	34.7	37.6	26.2	9.8	14.8	11.6	9.3	43.0	40.2	38.7	20.3	14.8	16.0	20.5	12.6	7.5	9.8	8.4
Eu	2.45	2.95	2.92	1.33	3.39	3.58	1.21	7.67	4.13	8.26	9.00	6.41	2.37	3.49	2.73	2.23	9.77	9.16	8.82	4.55	3.37	3.70	4.66	2.85	1.73	2.24	1.96
Gd	10.3	14.0	12.7	5.6	13.9	15.1	5.5	37.7	20.7	37.0	40.1	29.0	9.8	14.7	11.0	8.9	39.2	36.9	34.6	19.2	14.7	16.2	19.8	12.3	8.2	9.9	9.0
Tb	1.6	2.2	2.0	0.9	2.1	2.3	0.9	5.9	3.2	5.6	6.0	4.4	1.5	2.2	1.7	1.4	5.9	5.6	5.2	2.9	2.3	2.5	3.1	1.9	1.3	1.5	1.4
Dy	9.7	13.8	11.4	5.2	11.8	13.6	5.4	36.8	20.6	32.5	34.5	25.5	8.6	12.9	9.4	7.7	32.6	31.1	28.6	16.6	13.3	14.9	17.6	11.2	7.9	9.2	8.9
Ho	2.2	3.3	2.5	1.2	2.5	3.0	1.3	8.8	5.0	7.1	7.5	5.7	1.9	2.8	2.0	1.6	6.8	6.4	5.9	3.6	3.0	3.4	3.8	2.5	1.9	2.1	2.1
Er	6.2	9.5	7.3	3.3	6.9	8.4	3.6	25.7	15.1	19.6	20.8	15.9	5.3	7.8	5.6	4.4	18.5	17.8	16.0	10.1	8.5	9.7	10.9	7.4	5.6	6.1	6.3
Tm	0.86	1.31	0.98	0.45	0.92	1.13	0.51	3.56	2.12	2.56	2.67	2.09	0.72	1.04	0.75	0.61	2.46	2.39	2.11	1.41	1.21	1.37	1.51	1.03	0.79	0.87	0.90
Yb	5.4	8.5	6.2	2.9	5.9	7.2	3.4	22.7	13.8	15.8	16.1	12.8	4.6	6.5	4.7	3.8	15.4	15.2	13.1	9.1	8.0	8.9	9.9	6.9	5.4	5.8	6.0
Lu	0.84	1.37	0.97	0.45	0.88	1.11	0.54	3.70	2.30	2.39	2.46	2.00	0.69	0.98	0.69	0.56	2.31	2.31	1.97	1.45	1.26	1.46	1.56	1.12	0.85	0.94	0.98
∑REE	224	263	277	121	328	335	111	690	401	750	800	598	240	365	287	227	1020	968	935	508	369	392	497	324	205	253	216
Ce/Ce*	0.49	0.32	0.53	0.49	0.69	0.55	0.38	0.28	0.28	0.50	0.53	0.48	0.65	0.64	0.70	0.71	0.74	0.74	0.76	0.77	0.67	0.64	0.72	0.69	0.55	0.67	0.62
Ce anomaly	-0.31	-0.49	-0.27	-0.31	-0.16	-0.26	-0.42	-0.56	-0.55	-0.30	-0.27	-0.32	-0.19	-0.19	-0.16	-0.15	-0.13	-0.13	-0.12	-0.12	-0.17	-0.20	-0.14	-0.16	-0.26	-0.17	-0.21
Pr/Pr*	1.21	1.32	1.18	1.22	1.13	1.19	1.27	1.34	1.33	1.19	1.18	1.20	1.11	1.12	1.11	1.09	1.10	1.09	1.08	1.06	1.10	1.12	1.09	1.09	1.16	1.09	1.10

Table 1. Concentrations of major elements (wt%), trace elements and rare-earth elements (ppm), and elemental ratios in 58 phosphorite samples from the three phosphorite basins of Tunisia.

Eu/Eu*	1.15	1.21	1.22	0.85	1.33	1.36	0.79	1.94	1.41	2.03	2.12	1.79	1.12	1.34	1.20	1.09	2.25	2.18	2.15	1.51	1.29	1.36	1.53	1.19	0.91	1.05	0.98
Y/Y*	1.57	1.75	1.61	1.63	1.32	1.47	1.65	1.78	1.97	1.57	1.57	1.66	1.52	1.61	1.47	1.43	1.33	1.33	1.32	1.43	1.54	1.56	1.48	1.61	1.83	1.65	1.79
$(La/Sm)_N$	0.92	0.97	0.83	0.89	0.72	0.80	0.98	1.04	1.16	0.77	0.72	0.86	0.85	0.86	0.82	0.80	0.75	0.77	0.76	0.79	0.85	0.85	0.78	0.88	1.07	0.90	0.91
$(La/Yb)_N$	0.81	0.67	0.82	0.80	0.89	0.84	0.69	0.69	0.68	0.86	0.85	0.89	0.92	0.99	1.03	1.00	1.06	1.03	1.14	0.90	0.80	0.78	0.82	0.81	0.75	0.77	0.65
$(Dy/Yb_{jN}$	1.08	0.98	1.11	1.08	1.21	1.14	0.96	0.98	0.90	1.24	1.29	1.20	1.13	1.20	1.21	1.22	1.28	1.23	1.32	1.10	1.00	1.01	1.07	0.98	0.88	0.96	0.89
La/Nd	1.26	1.37	1.17	1.23	1.01	1.14	1.38	1.45	1.56	1.10	1.02	1.19	1.16	1.15	1.10	1.08	1.03	1.04	1.03	1.08	1.17	1.18	1.09	1.18	1.41	1.23	1.26

[1]calculated assuming 34.7% P_2O_5 in Tunisian phosphate rock francolite (McClellan 1980); nd: not determined; Post-Archean Average Shale values used for REE normalisation after McLennan (1989).

Table 1. continued.

Basin	Gafsa-Metlaoui Basin																												
Deposit	Central Kef Eddour (locality 5)								Table Metlaoui 315 (locality 6)								Mzinda (locality 7)								Jellabia 56 (locality 8)						
Samples	KECI	KECII	KECIII	KECIV	KECV	KECVI	KECVII	KECVIII	TMI	TMII	TMIII	TMIV	TMV	TMVI	TMVIIa	TMVIII	MZ0	MZI>	MZI<	MZH1	MZH2	MZII>	MZII<	MZIII	JLA0	JLAI	JLAH1	JLAH2	JLAII>	JLII<	JLAIII
Major oxides (%)																															
SiO_2	6.97	6.11	12.60	14.01	12.02	7.65	6.20	6.70	7.91	8.02	13.30	14.51	6.23	10.13	8.15	5.90	29.98	18.30	5.20	11.64	9.53	7.86	4.27	4.41	35.60	4.17	6.88	10.21	4.44	2.64	5.32
TiO_2	0.053	0.040	0.058	0.041	0.051	0.051	0.044	0.042	0.061	0.062	0.047	0.052	0.048	0.077	0.069	0.042	0.146	0.060	0.049	0.100	0.029	0.082	0.041	0.039	0.072	0.040	0.054	0.038	0.050	0.031	0.048
Al_2O_3	1.28	0.92	1.58	1.13	1.27	1.19	0.92	0.99	1.38	1.45	1.21	1.24	0.98	1.71	1.31	0.99	3.67	1.33	1.09	2.07	0.58	1.89	0.83	0.84	1.94	0.86	1.12	0.75	1.08	0.57	1.06
Fe_2O_3(T)	0.56	0.44	0.65	0.45	0.56	0.56	0.38	0.43	0.55	0.56	0.56	0.59	0.52	0.81	0.54	0.49	1.24	0.54	0.51	0.91	0.32	0.79	0.34	0.31	0.61	0.38	0.53	0.25	0.44	0.26	0.41
MnO	0.003	0.003	0.005	0.005	0.005	0.007	0.004	0.003	0.005	0.006	0.007	0.007	0.005	0.005	0.004	0.004	0.007	0.005	0.004	0.007	0.003	0.005	0.003	0.004	0.007	0.005	0.004	0.003	0.003	0.002	0.003
MgO	0.62	0.67	0.78	0.60	0.72	0.81	0.81	0.76	0.53	0.53	0.67	0.74	0.65	0.98	1.17	0.74	5.17	1.44	1.45	1.30	0.50	1.22	0.84	0.67	3.08	3.17	1.97	0.53	0.76	0.62	0.76
CaO	45.88	46.78	42.44	42.61	42.67	44.64	45.34	45.27	43.53	44.00	42.07	40.91	45.30	44.01	44.47	46.63	26.78	39.74	46.61	41.98	45.92	44.05	46.44	48.00	28.50	45.59	45.34	45.03	47.77	48.47	47.46
Na_2O	1.42	1.47	1.38	1.35	1.42	1.37	1.30	1.39	1.46	1.47	1.39	1.36	1.50	1.48	1.33	1.49	1.11	1.24	1.48	1.37	1.39	1.54	1.55	1.50	0.88	1.25	1.37	1.46	1.51	1.53	1.26
K_2O	0.32	0.15	0.20	0.15	0.16	0.14	0.14	0.18	0.45	0.45	0.15	0.14	0.13	0.19	0.17	0.21	0.74	0.29	0.13	0.24	0.10	0.19	0.11	0.16	0.59	0.11	0.12	0.10	0.14	0.08	0.32
P_2O_5	27.81	28.83	25.38	25.93	25.94	27.02	25.64	25.65	26.40	26.62	25.91	24.87	28.30	26.58	24.14	27.12	11.56	20.81	27.61	23.83	27.43	27.00	28.46	24.15	14.38	25.93	26.50	28.54	29.35	30.32	26.79
SO_3	3.90	4.99	3.72	3.57	nd	nd	6.72	5.22	nd	5.87	3.77	3.62	6.12	3.77	5.72	nd	1.46	2.67	6.84	3.70	4.49	4.14	2.37	5.22	1.54	3.22	2.65	2.95	4.52	3.95	2.70
LOI	11.90	12.03	13.01	12.60	12.56	13.45	12.98	13.39	12.01	12.24	12.36	12.75	11.64	12.20	15.06	12.12	17.98	14.10	12.64	14.85	12.64	13.70	12.05	14.80	12.71	14.48	13.29	11.71	10.38	9.98	12.86
Total	100.71	102.44	101.80	102.45	97.38	96.89	100.47	100.02	94.29	101.28	101.44	100.79	101.42	101.94	102.13	95.74	99.85	100.53	103.61	101.99	102.94	102.47	97.31	100.10	99.91	99.21	99.82	101.57	100.44	98.45	98.99
Francolite[1] (%)	80	83	73	75	75	78	74	74	76	77	75	72	82	77	70	78	33	60	80	69	79	78	82	70	41	75	76	82	85	87	77
CaO/P_2O_5	1.65	1.62	1.67	1.64	1.64	1.65	1.77	1.76	1.65	1.65	1.62	1.64	1.60	1.66	1.84	1.72	2.32	1.91	1.69	1.76	1.67	1.63	1.63	1.99	1.98	1.76	1.71	1.58	1.63	1.60	1.77
SO_3/P_2O_5	0.14	0.17	0.15	0.14	nd	nd	0.26	0.20	nd	0.22	0.15	0.15	0.22	0.14	0.24	nd	0.13	0.13	0.25	0.16	0.16	0.15	0.08	0.22	0.11	0.12	0.10	0.10	0.15	0.13	0.10
Trace elements (ppm)																															
As	6.5	3.3	< 0.5	5.2	< 0.5	< 0.5	< 0.5	3.4	7.4	< 0.5	< 0.5	< 0.5	2.8	< 0.5	< 0.5	23.2	4.3	6.6	4.5	4.3	< 0.5	4.0	2.3	2.0	7.5	4.5	5.5	< 0.5	3.9	4.0	3.5
Ba	40	32	32	30	61	31	22	29	41	42	30	34	32	33	27	41	124	59	31	42	27	33	27	28	93	34	35	30	35	30	29
Br	10.8	8.6	9.8	17.1	46.1	36.3	8.0	10.1	14.6	15.7	12.5	12.5	9.7	11.7	11.8	12.3	11.2	9.3	12.1	8.8	11.4	7.9	8.8	12.6	5.2	6.7	9.0	9.0	8.0	8.0	9.3
Cd	60.8	86.9	49.2	22.0	nd	nd	56.3	50.4	nd	35.1	69.8	21.0	36.0	25.1	66.4	nd	4.3	19.1	28.2	20.1	63.8	48.8	65.9	32.9	8.2	13.7	1.3	1.2	10.0	6.1	18.9
Cr	273	212	275	258	202	272	220	219	311	298	241	293	295	373	227	258	132	177	220	220	209	374	220	220	117	154	154	264	279	188	213
Cu	11	10	8	6	20	20	12	12	20	8	7	6	7	8	13	30	9	6	5	5	5	11	9	8	7	4	2	3	6	4	7
Hf	0.6	0.4	0.4	0.4	0.5	0.5	0.5	0.4	0.6	0.4	0.4	0.4	0.5	0.6	0.5	0.4	1.3	1.1	0.4	0.7	0.4	0.7	0.4	0.3	1.0	0.4	0.5	0.5	0.6	0.4	0.4
Mo	11	4	3	3	4	5	5	4	8	8	3	3	4	5	7	4	4	16	10	6	< 2	20	4	6	3	2	< 2	2	8	5	6
Nb	2	1	2	1	2	2	2	1	2	1	1	2	2	2	3	2	6	2	2	4	1	3	2	2	3	1	2	2	2	1	2
Ni	22	18	14	14	20	30	30	29	20	14	13	12	14	20	36	50	14	11	10	13	10	39	24	19	11	8	6	3	11	7	13
Rb	6	4	6	4	5	4	4	4	6	4	5	5	4	6	5	4	12	5	4	8	3	5	3	3	7	3	4	3	3	2	4
Sb	1.0	0.7	< 0.2	0.4	< 0.2	< 0.2	< 0.2	0.3	1.5	0.7	< 0.2	0.4	0.6	< 0.2	0.4	< 0.2	0.8	0.9	0.4	< 0.2	0.6	0.4	0.6	< 0.2	1.1	0.6	0.7	< 0.2	0.7	0.5	0.5
Sc	5.1	3.5	4.3	4.2	4.1	4.0	2.8	2.6	5.6	3.7	3.5	3.7	4.5	4.7	3.4	5.0	3.8	3.1	3.7	4.2	3.4	4.2	2.6	2.5	2.6	2.8	3.3	4.0	4.0	2.5	2.8
Sr	1820	1900	1810	1780	1800	1850	1650	1700	1840	1870	1850	1780	1930	1860	1630	1830	927	1580	1900	1820	1940	1940	1950	1720	1040	1730	2000	2040	2070	2150	1720
Th	14.1	10.5	9.3	6.1	6.6	8.1	3.1	3.0	16.8	9.5	8.4	5.6	7.0	10.3	2.6	3.0	7.3	9.4	8.7	7.3	5.5	8.8	4.9	2.7	9.9	10.5	6.2	8.6	10.8	6.0	3.2
U	34.2	26.7	26.1	23.9	31.9	37.7	41.0	33.7	33.4	26.1	23.0	20.7	32.0	36.2	34.8	33.1	17.4	26.7	27.3	15.9	16.8	51.5	41.9	29.1	19.9	29.5	20.5	23.8	53.7	47.9	33.6
V	52	44	59	71	91	80	66	73	129	61	59	83	77	73	97	65	66	39	44	57	28	187	79	55	184	43	40	139	97	64	61
Y	140	131	101	100	106	120	91	82	143	147	101	86	112	122	97	84	52	82	89	83	87	98	108	66	70	87	76	115	112	113	73
Zn	290	401	276	148	320	340	297	244	450	252	497	142	209	149	393	190	80	140	206	149	401	290	381	158	62	113	75	58	151	103	98
Zr	44	34	31	31	39	39	37	29	46	49	30	34	41	40	46	47	67	64	31	48	43	52	42	29	56	27	33	43	49	36	33
Rare-earth elements (ppm)																															
La	108	91.8	80.3	76.4	68.8	79.9	50.4	45.1	118	86.5	79.8	67.9	76.4	83.0	49.7	46.1	55.2	73.7	78.0	78.6	78.5	78.4	65.6	40.1	66.3	74.5	78.3	104	100	73.5	46.3
Ce	164	133	130	108	92.1	117	60.5	49.3	197	124	129	96.4	97.1	125	50.6	51.2	95.4	118	120	122	113	117	80.1	46.1	116	115	126	158	153	94.1	55.0
Pr	23.5	19.4	17.9	15.4	13.9	17.0	8.8	7.8	27.2	18.5	17.9	13.7	15.0	18.3	8.0	7.9	12.4	16.2	16.8	16.5	15.5	16.5	12.0	7.0	15.6	16.5	16.5	21.7	21.4	13.8	8.2
Nd	96.5	80.2	73.5	63.2	56.4	69.5	35.6	32.0	112	76.3	73.5	55.8	61.3	74.7	32.6	32.8	49.4	65.6	68.6	67.4	62.7	66.2	48.5	28.5	63.3	66.7	66.4	87.2	85.8	55.1	32.7
Sm	18.9	15.8	14.4	11.9	11.1	13.9	6.7	6.2	22.2	14.8	14.5	10.7	12.1	15.3	6.1	6.3	9.4	12.5	13.0	12.8	11.7	12.8	9.4	5.2	12.2	12.8	12.5	16.6	16.3	10.6	6.1
Eu	4.34	3.69	3.25	2.72	2.56	3.23	1.61	1.50	4.98	3.46	3.30	2.40	2.74	3.45	1.48	1.53	2.23	2.90	2.97	2.88	2.66	2.91	2.21	1.26	2.79	2.92	2.82	3.80	3.70	2.46	1.47
Gd	18.4	15.7	13.5	11.6	11.1	14.0	7.4	6.8	20.5	14.4	13.5	10.3	12.0	14.8	7.0	6.9	8.4	11.6	12.1	11.8	11.4	12.2	10.1	5.6	10.8	11.9	11.4	15.6	15.5	11.0	6.5
Tb	2.8	2.4	2.1	1.8	1.8	2.2	1.2	1.1	3.1	2.2	2.0	1.6	1.9	2.3	1.1	1.1	1.3	1.7	1.8	1.8	1.7	1.9	1.6	0.9	1.60	1.8	1.7	2.4	2.4	1.7	1.0
Dy	16.1	14.0	11.8	10.4	10.4	12.8	7.4	6.9	17.4	13.0	11.7	9.3	11.3	13.4	7.2	7.0	7.0	9.8	10.4	10.3	10.0	10.8	9.7	5.5	8.90	10.3	9.8	13.4	13.6	10.5	6.2
Ho	3.5	3.1	2.5	2.3	2.3	2.8	1.8	1.7	3.7	2.8	2.5	2.0	2.6	2.9	1.8	1.7	1.5	2.1	2.2	2.2	2.2	2.3	2.3	1.3	1.8	2.2	2.1	2.8	2.9	2.4	1.5
Er	10.1	8.9	7.3	6.7	6.9	8.2	5.7	5.3	10.3	8.2	7.1	5.9	7.6	8.3	5.7	5.3	4.1	5.8	6.3	6.3	6.4	6.7	6.9	4.1	5.10	6.3	5.8	8.2	8.4	7.3	4.5
Tm	1.38	1.26	1.01	0.96	0.98	1.16	0.82	0.76	1.43	1.13	0.99	0.83	1.08	1.16	0.83	0.77	0.56	0.80	0.87	0.87	0.90	0.94	0.99	0.59	0.69	0.86	0.81	1.15	1.16	1.05	0.66
Yb	9.2	8.3	6.7	6.4	6.7	7.8	5.7	5.2	9.3	7.5	6.6	5.6	7.3	7.8	5.6	5.2	3.6	5.1	5.8	5.7	5.9	6.2	6.6	3.9	4.4	5.7	5.4	7.4	7.8	7.0	4.3
Lu	1.46	1.32	1.04	1.03	1.08	1.22	0.96	0.86	1.45	1.22	1.03	0.88	1.19	1.22	0.94	0.87	0.54	0.78	0.90	0.89	0.92	0.97	1.06	0.65	0.66	0.90	0.81	1.14	1.21	1.12	0.71
∑REE	478	399	365	319	286	351	195	170	549	374	363	283	310	372	179	175	251	327	340	340	323	336	257	151	310	328	340	443	433	292	175
Ce/Ce*	0.73	0.70	0.77	0.69	0.66	0.71	0.62	0.56	0.78	0.69	0.77	0.70	0.63	0.72	0.54	0.57	0.83	0.77	0.74	0.75	0.71	0.73	0.62	0.59	0.82	0.74	0.78	0.74	0.74	0.65	0.61
Ce anomaly	-0.14	-0.16	-0.11	-0.16	-0.18	-0.15	-0.21	-0.25	-0.11	-0.16	-0.12	-0.16	-0.20	-0.14	-0.27	-0.24	-0.08	-0.11	-0.13	-0.12	-0.15	-0.14	-0.21	-0.23	-0.09	-0.13	-0.11	-0.13	-0.13	-0.19	-0.21
Pr/Pr*	1.08	1.09	1.07	1.08	1.12	1.09	1.10	1.13	1.07	1.10	1.07	1.09	1.12	1.10	1.14	1.12	1.06	1.07	1.08	1.06	1.07	1.09	1.12	1.12	1.06	1.10	1.06	1.08	1.09	1.11	1.12
Eu/Eu*	1.48	1.37	1.28	1.17	1.13	1.27	0.89	0.87	1.59	1.34	1.30	1.09	1.16	1.31	0.85	0.88	1.10	1.23	1.24	1.21	1.15	1.21	1.04	0.80	1.22	1.23	1.20	1.40	1.37	1.10	0.86
Y/Y*	1.49	1.59	1.48	1.63	1.73	1.60	1.98	1.90	1.42	1.94	1.49	1.59	1.65	1.56	2.14	1.94	1.28	1.44	1.48	1.39	1.48	1.57	1.82	1.97	1.39	1.46	1.34	1.50	1.42	1.79	1.91
$(La/Sm)_N$	0.83	0.84	0.81	0.93	0.90	0.84	1.09	1.06	0.77	0.85	0.80	0.92	0.92	0.79	1.18	1.06	0.85	0.86	0.87	0.89	0.97	0.89	1.01	1.12	0.79	0.85	0.91	0.91	0.89	1.01	1.10
$(La/Yb)_N$	0.87	0.82	0.88	0.88	0.76	0.76	0.65	0.64	0.94	0.85	0.89	0.90	0.77	0.79	0.66	0.65	1.13	1.07	0.99	1.02	0.98	0.93	0.73	0.76	1.11	0.96	1.07	1.04	0.95	0.78	0.79
$(Dy/Yb)_N$	1.05	1.02	1.06	0.98	0.94	0.99	0.78	0.80	1.13	1.04	1.07	1.00	0.93	1.04	0.77	0.81	1.17	1.16	1.08	1.09	1.02	1.05	0.89	0.85	1.22	1.09	1.09	1.09	1.05	0.90	0.87
La/Nd	1.12	1.14	1.09	1.21	1.22	1.15	1.42	1.41	1.05	1.13	1.09	1.22	1.25	1.11	1.52	1.41	1.12	1.12	1.14	1.17	1.25	1.18	1.35	1.41	1.05	1.12	1.18	1.19	1.17	1.33	1.42

Table 2. Concentration (ppm) of trace elements in sphalerite determined by LA-ICP-MS.

Element	Sample										
	04-SP-01	05-SP-02	06-SP-03	07-SP-04	08-SP-05	12-SP-G-01	13-SP-G-02	14-SP-G-03	15-SP-G-04	16-SP-G-05	17-SP-G-06
Ag	159	99	21	51	29	60	42	52	54	58	46
As	bd	bd	590	bd	798	bd	bd	69	72	bd	bd
Cd	44200	57500	57200	62100	64400	65300	16000	8320	9320	24600	30200
Cr	124	bd	6.3	bd	7.1	bd	bd	bd	bd	bd	3.2
Cu	232	175	7.9	36	12	44	48	5.5	5.3	33	59
Fe	446	216	93	402	105	368	1100	221	192	753	586
Mn	11	0.5	19	bd	25	bd	bd	79	82	bd	bd
Mo	2.5	0.2	0.3	0.1	0.7	bd	bd	0.1	0.1	0.1	bd
Ni	18	bd	0.3	0.4	0.6	bd	0.8	0.4	0.5	1.2	bd
Pb	7.6	3.9	5.2	3.3	6.8	3.4	15	6.4	6.4	2.6	3.2
Sb	18	8.4	52	8.9	100	12	4.3	5.1	5.4	1.4	4.5
Sn	48	20	69	20	106	26	2.6	bd	bd	1.7	3.4
Ti	39	1.4	4.5	5.2	3.7	4.4	2.0	bd	bd	1.9	5.1
V	21	0.2	0.5	0.2	0.8	0.3	0.6	0.2	bd	bd	0.6

bd: below detection

Table 3. Concentration (ppm) of trace elements in pyrite determined by LA-ICP-MS.

Element	Sample			
	24-PYG-01	25-PYG-02	26-PYG-03	27-PYG-04
Ag	0.9	2.0	0.4	0.03
As	392	704	253	279
Cd	4.0	6.7	bd	bd
Co	7.0	43.3	10.5	0.8
Cr	4.5	5.0	4.1	2.4
Cu	5.0	2.7	0.14	0.3
Mn	10.3	19.6	7.8	9.9
Mo	86	149	39	41
Ni	16.1	47.9	7.6	4.3
Pb	2.2	5.3	2.1	0.2
Sb	2.2	2.6	1.4	1.4
Sn	0.1	bd	0.07	bd
Ti	6.8	16.5	8.1	6.0
V	1.4	5.8	3.9	0.3
Zn	11.3	21.5	13.6	8.7

bd: below detection

Table 4 Inter-element correlations based on the Pearson correlation coefficient.

Positive inter-elemental correlations			
	High (>0.75)	Medium (0.75 to 0.5)	Low (0.5 to 0.36)
Major elements			
SiO_2		K_2O, Ba, Rb, Nb, Hf	Al_2O_3, MgO, TiO_2, Zr
TiO_2	Zr, Rb, Nb, Hf		Ba
Al_2O_3	TiO_2, Rb, Nb	K_2O, Ba, Zr, Hf	Fe_2O_3
Fe_2O_3(T)	MnO, As, Rb, Sb	V, Ni, Ba, Mo	Y, Hf, REE
MnO		Ni, Sb, As, Rb	V, Ba, Mo, Hf, Y
MgO		K_2O, Ba, Nb, Hf	TiO_2, Zr
CaO		P_2O_5, Sr	Cr
Na_2O	P_2O_5, SO_3, Sr		Cr, Zn
K_2O	Nb, Hf	TiO_2, Ba, Zr, Rb	
P_2O_5	Sr	SO_3, Cr	Zn, U
SO_3		Sr	Cr, Zn, Br
Trace elements			
As	Sb	Mo	REE
Ba		Zr, As, Sb, Hf, Rb, Nb	
Cu			U, HREE
Mo		Sb	U, REE
Nb	Hf		
Ni	As	Cu, Mo, Sb	Rb, U, HREE
Rb		Nb, Hf	Sb
REE	REE		
Sb		REE	
Sc	Y, HREE	Cu, U, LREE	Cr, Sb, Ni
Sr			Cr, Zn, Th
Th	LREE	HREE	
U	HREE	LREE	
V		Ni, As, Sb	Y, Cr, Mo
Y	REE	Ni, As, Sb, U	Cu, Mo, Th
Zn	Cd		
Zr	Nb, Hf		Rb

Negative inter-elemental correlations			
	High (<-0.75)	Medium (-0.75 to -0.5)	Low (-0.5 to -0.36)
Major elements			
SiO_2	CaO	P_2O_5, Sr	Na_2O, SO_3, Cr
TiO_2	P_2O_5	Sr	SO_3, U
Al_2O_3		P_2O_5	SO_3, Sr, U
Fe_2O_3(T)			Na_2O, Sr
MnO		Na_2O, Sr	P_2O_5, SO_3, Zn
MgO	CaO	P_2O_5, Sr	Na_2O, Cr
CaO	K_2O	TiO_2, Ba, Nb, Hf	Rb
Na_2O		Ba, Rb, Nb, Hf	K_2O, TiO_2, Ni, Cu, Sb
K_2O		P_2O_5, Sr	SO_3, Cr
P_2O_5	Nb	Ba, Rb, Hf	Zr
SO_3		Ba, Rb, Hf	Cu, Nb
Trace elements			

Table 5. Loadings of 45 geochemical variables in Tunisian phosphorites on first four significant principal components.

Constituent	Principal component			
	PC1 (38.8%)	PC2 (24.3%)	PC3 (8.1%)	PC4 (5.4%)
Major elements				
SiO_2	0.00	0.67	-0.23	0.09
TiO_2	0.23	**0.81**	-0.22	-0.23
Al_2O_3	0.17	**0.73**	-0.23	-0.06
Fe_2O_3(T)	-0.53	0.58	0.21	0.43
MnO	-0.39	0.56	0.38	0.42
MgO	0.11	0.62	-0.26	0.13
CaO	-0.10	**-0.70**	0.38	-0.15
Na_2O	0.10	**-0.76**	-0.39	0.18
K_2O	-0.03	**0.81**	-0.38	-0.06
P_2O_5	-0.25	**-0.87**	-0.06	0.14
SO_3	0.11	-0.64	-0.19	0.22
Trace elements				
As	-0.61	0.37	0.33	0.36
Ba	-0.22	0.79	-0.05	-0.04
Br	0.07	-0.12	0.14	-0.20
Cd	0.10	-0.47	-0.04	-0.13
Cr	-0.37	-0.42	0.25	0.19
Cu	-0.32	0.17	0.52	-0.57
Hf	-0.09	**0.89**	-0.14	-0.21
Mo	-0.45	0.15	0.16	0.54
Nb	0.28	**0.82**	-0.20	-0.27
Ni	-0.52	0.29	0.65	0.05
Rb	-0.14	**0.86**	0.05	0.09
Sb	-0.73	0.41	0.17	0.35
Sc	-0.72	0.02	0.17	-0.43
Sr	0.02	**-0.89**	-0.30	0.02
Th	-0.61	-0.20	-0.67	0.04
U	-0.61	-0.26	0.35	-0.36
V	-0.40	0.20	0.37	0.30
Y	**-0.95**	-0.02	0.16	-0.16
Zn	0.02	-0.50	-0.13	-0.12
Zr	0.10	0.66	-0.35	-0.32
Rare-earth elements				
La	**-0.97**	-0.07	-0.20	-0.05
Ce	**-0.76**	-0.17	-0.56	0.17
Pr	**-0.93**	-0.06	-0.34	0.07
Nd	**-0.94**	-0.04	-0.31	0.07
Sm	**-0.95**	-0.02	-0.28	0.07
Eu	**-0.96**	0.01	-0.24	0.04
Gd	**-0.99**	0.01	-0.13	0.00
Tb	**-0.99**	0.01	-0.12	-0.02
Dy	**-0.99**	0.00	-0.06	-0.06
Ho	**-0.99**	-0.01	0.02	-0.12
Er	**-0.98**	-0.03	0.05	-0.14
Tm	**-0.97**	-0.07	0.06	-0.18
Yb	**-0.96**	-0.11	0.06	-0.21
Lu	**-0.94**	-0.14	0.11	-0.25
Eigenvalue	17.5	10.9	3.7	2.4
Cumulative eigenvalue	17.5	28.4	32.1	34.5

Table 6. Structural formulae of francolite in Tunisian phosphorites from different basins (after Ounis, 2011).

Basin	Locality	a	c	CO_3^{2-} (%)	CO_2 (%)	Empirical formula
Gafsa-Metlaoui	Gafsa	9.347	6.903	8.31	6.11	$(Ca_{9.78}\ Mg_{0.06}\ Na_{0.16})\ [(PO_4)_{5.19}\ (CO_3)_{0.81}]\ (F_{2.32})$
Eastern Basins	Meknassy-Mezzouna 1	9.322	6.900	7.95	5.85	$(Ca_{9.53}\ Mg_{0.13}\ Na_{0.34})\ [(PO_4)_{3.96}\ (CO_3)_{2.04}]\ (F_{2.82})$
Northern Basins	Sra Ouertane (pure)	9.341	6.896	6.02	4.43	$(Ca_{9.72}\ Mg_{0.08}\ Na_{0.20})\ [(PO_4)_{4.93}\ (CO_3)_{1.81}]\ (F_{2.32})$

Table A1. Mineralogy of 58 phosphorite samples from the three phosphorite basins of Tunisia determined by semi-quantitative x-ray c

Sample	Bulk coarse fraction mineralogy (wt %)					Clay mineral assemblage (wt%)				
	Francolite	Calcite	Dolomite	Feldspar	Quartz	Smectite	Illite	Kaolinite	Palygorskite	Sepiolite
Northern Basins										
Sra Ouertane (locality 1)										
SRO1	28	50	8	6	8	100	0	0	0	0
SRO2	27	57	11	0	5	84	16	0	0	0
SRO3	29	46	7	8	10	78	22	0	0	0
SRO4	15	56	14	9	6	69	23	8	0	0
SRO5	22	64	8	2	4	70	30	0	0	0
SRO6	26	54	7	5	8	74	16	10	0	0
SRO7	37	39	10	7	7	60	20	20	0	0
SRO8	70	13	12	5	0	90	0	10	0	0
SRO9	60	19	9	7	5	100	0	0	0	0
Sekarna (locality 2)										
SEK1	42	30	15	0	13	0	36	64	0	0
SEK3	43	24	10	0	23	0	18	82	0	0
SEK4	52	15	8	0	25	15	0	85	0	0
Eastern Basins										
Jebel Jebs (locality 3)										
JBS4	30	8	32	0	30	85	15	0	0	0
JBS5	30	8	39	0	23	70	30	0	0	0
JBS10	26	15	30	4	25	100	0	0	0	0
JBS7	28	20	27	5	20	100	0	0	0	0
JBS14	48	5	17	7	23	100	0	0	0	0
JBS18	60	7	17	5	11	100	0	0	0	0
JBS19	57	8	19	7	9	70	0	15	15	0
Gafsa-Metlaoui Basin										
Naguess (locality 4)										
NAGI	61	19	10	0	10	100	0	0	0	0
NAGIIA	78	10	8	0	4	70	0	0	10	20
NAGIIB	70	16	9	0	5	80	0	0	10	10
NAGIII	60	24	12	2	2	75	0	0	10	15
NAGIV	56	18	14	5	7	75	0	0	10	15
NAGV	50	10	22	7	11	50	0	0	30	20
NAGVI	58	15	13	0	14	65	0	0	20	15
NAGVII and VIII	71	11	9	7	2	75	0	10	5	10
Central Kef Eddour (locality 5)										
KECI	72	13	6	0	9	100	0	0	0	0
KECII	74	14	8	0	4	90	0	0	5	5
KECIII	66	16	13	0	5	75	0	0	10	15
KECIV	67	16	10	4	3	72	0	0	10	18
KECV	59	19	11	5	6	70	0	0	15	15
KECVI	62	17	12	0	9	50	0	0	30	20
KECVII	67	11	12	0	10	60	0	5	20	15
KECVIII	68	9	10	4	9	70	0	10	10	10
Table Metlaoui 315 (locality 6)										
TMI	68	10	8	5	9	100	0	0	0	0
TMII	69	10	8	0	13	80	0	0	10	10
TMIII	66	16	8	0	10	78	0	0	10	12
TMIV	65	17	10	0	8	78	0	0	10	12
TMV	72	12	10	0	6	75	0	0	20	15
TMVI	71	10	5	6	8	50	0	0	30	20
TMVIIA	65	13	9	4	9	65	0	0	20	15
TMVIII	75	12	5	3	5	90	0	0	5	5
Mzinda (locality 7)										
MZ0	32	7	8	4	49	100	0	0	0	0
MZI>	48	10	16	5	21	100	0	0	0	0
MZI<	68	14	8	0	10	90	0	0	5	5
MZH1	70	9	12	0	9	75	0	0	15	10
MZH2	69	7	12	6	6	50	0	0	20	30
MZII>	56	12	16	0	16	90	0	0	5	5
MZII<	64	9	7	0	20	75	0	0	10	15
MZIII	58	8	10	0	24	55	0	5	20	20
Jellabia 56 (locality 8)										
JLA0	31	11	10	8	40	100	0	0	0	0
JLAI	36	12	26	6	20	100	0	0	0	0
JLAH1	66	8	7	0	19	80	0	0	10	10
JLAH2	68	10	12	0	10	78	0	0	12	10
JLAII>	60	16	8	0	16	90	0	0	5	5
JLII<	58	12	16	0	14	87	0	0	8	5
JLAIII	60	11	12	7	10	45	0	0	25	30

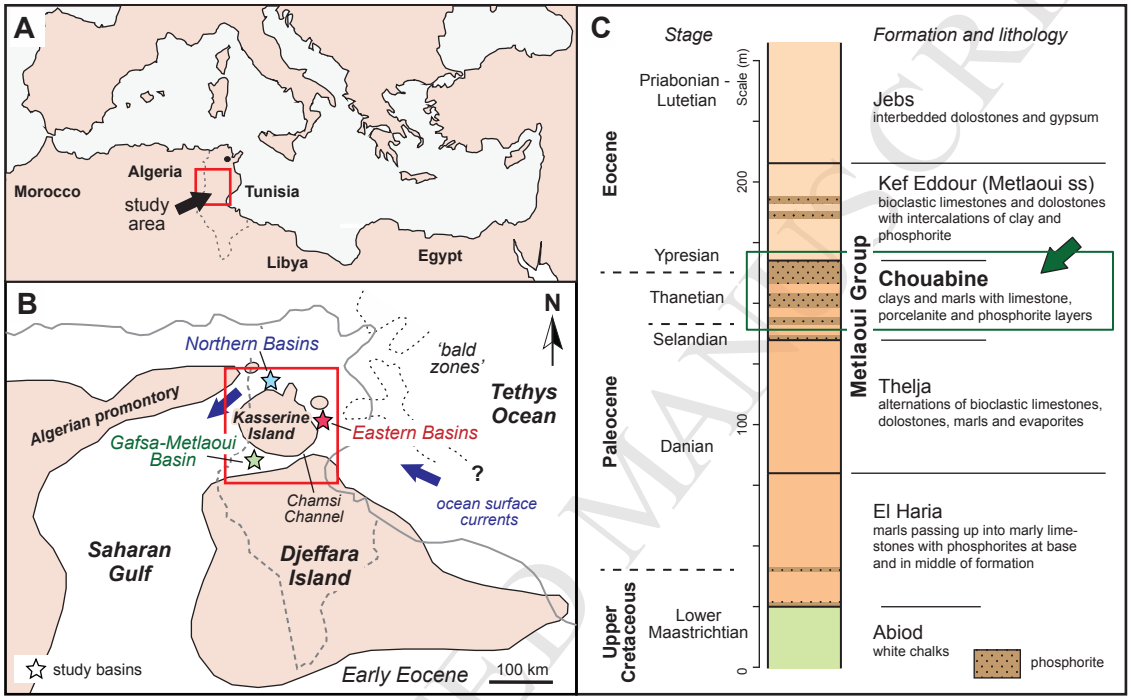

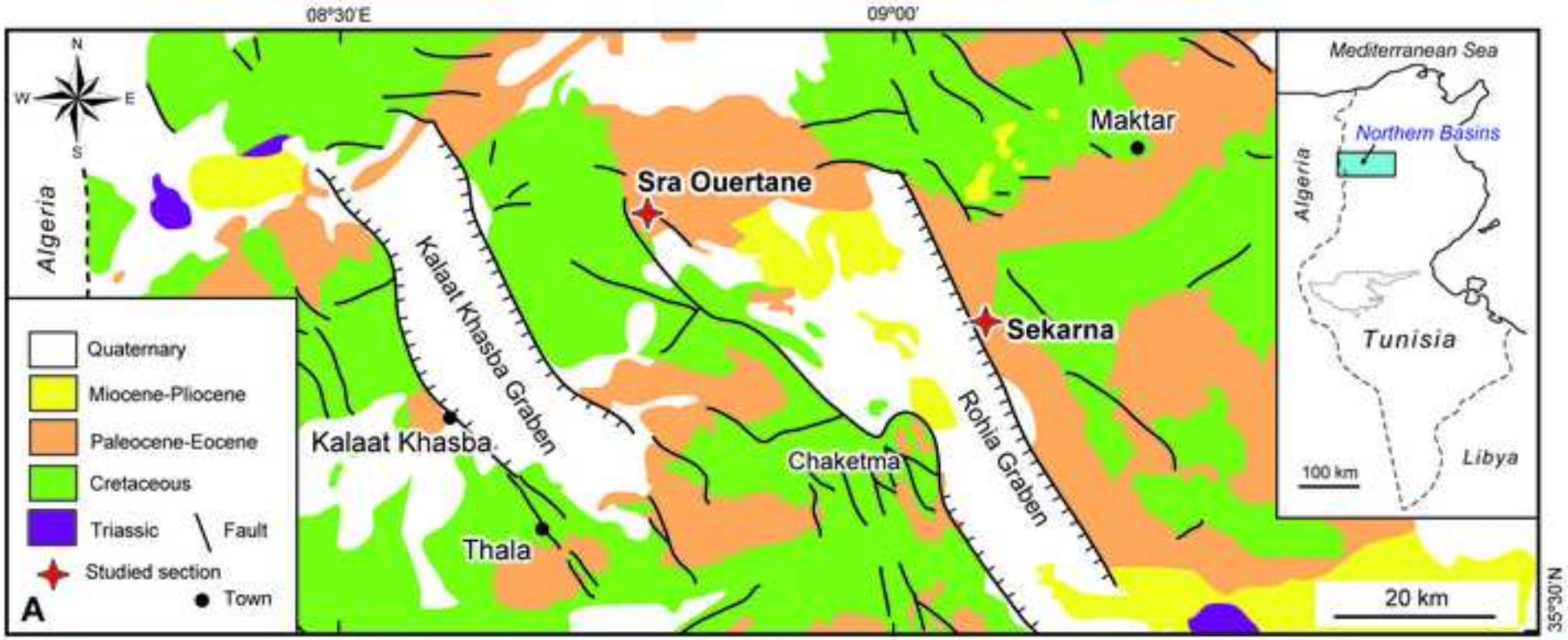
08°30'E
09°00'
35°30'N
N
W
E
S
Algeria
Quaternary
Miocene-Pliocene
Paleocene-Eocene
Cretaceous
Triassic
Fault
Studied section
Town
A
Kalaat Khasba
Thala
Kalaat Khasba Graben
Sra Ouertane
Chaketma
Rohia Graben
Maktar
Sekarna
20 km
Mediterranean Sea
Northern Basins
Algeria
Tunisia
Libya
100 km

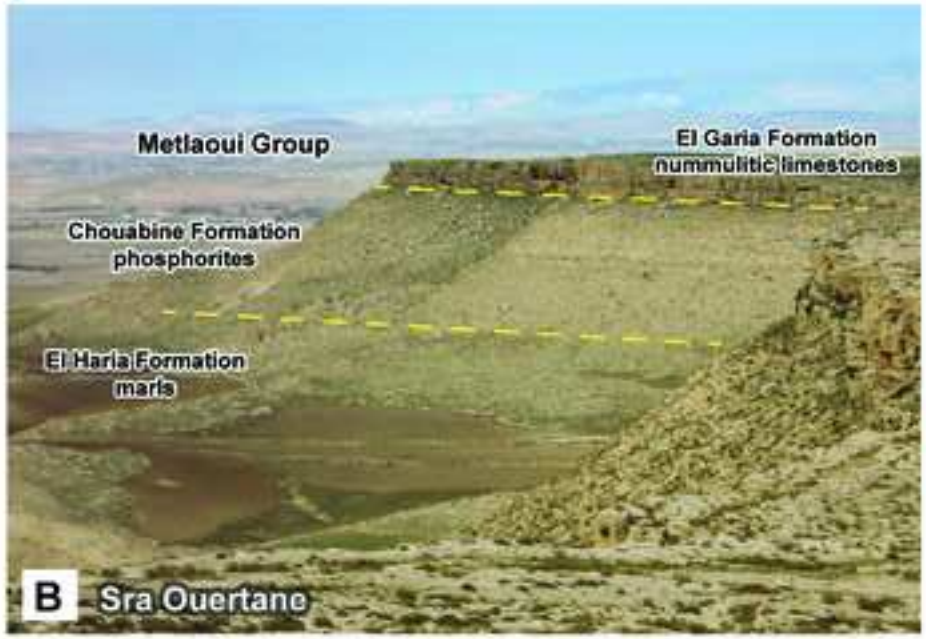
Metlaoui Group
El Garia Formation
nummulitic limestones
Chouabine Formation
phosphorites
El Haria Formation
marls
B
Sra Ouertane


Ras El Guezir 1322 m
nummulitic limestone
conglomeratic limestone
phosphatic glauconitic
microconglomerate
Metlaoui Group
Abiod Formation
chalk
Aleg Formation
interbedded limestones and marls
nummulitic limestone
C
Sekarna

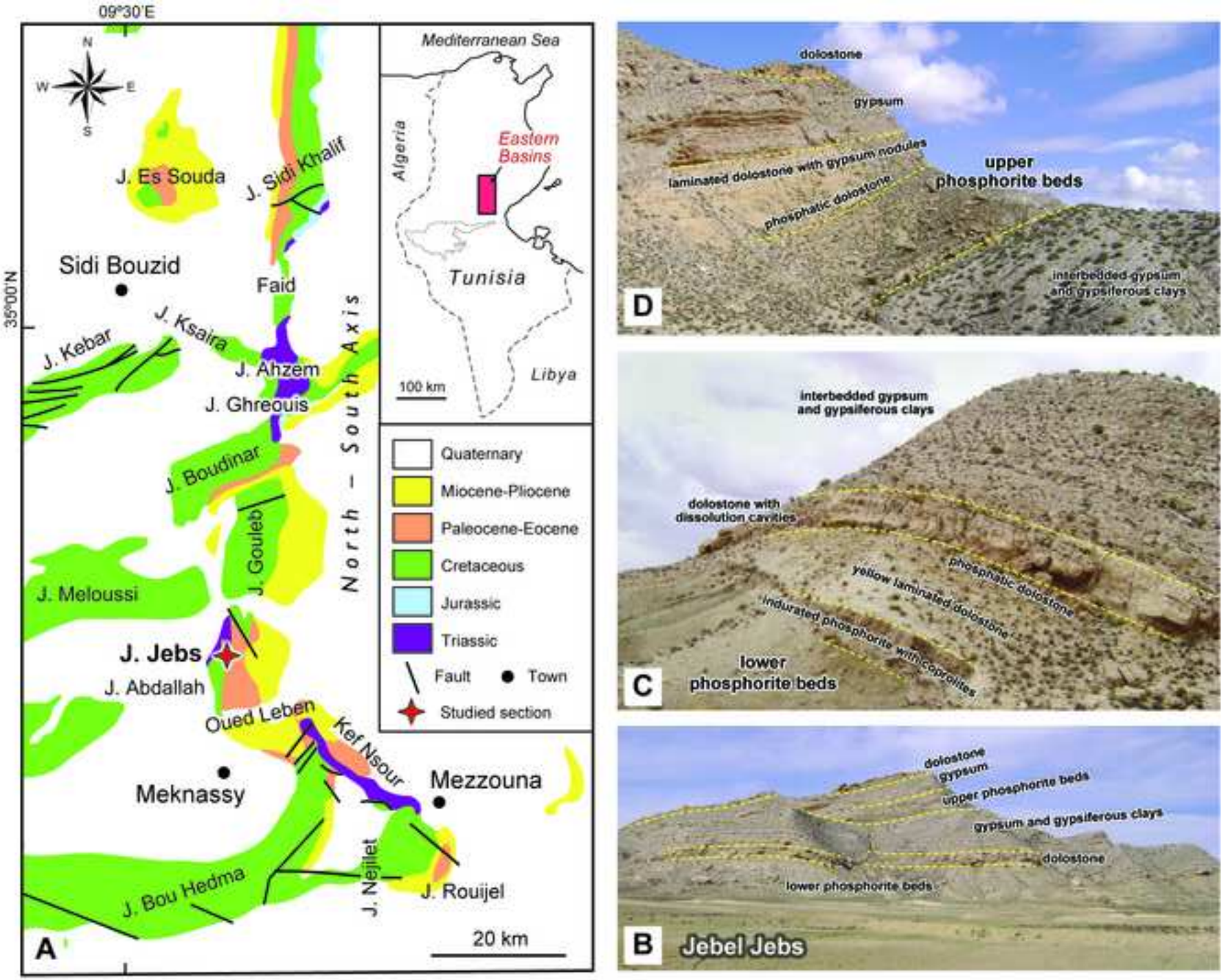
09°30'E
35°00'N
N
W
E
S
J. Es Souda
J. Sidi Khalif
Sidi Bouzid
Faid
J. Ksaira
J. Kebar
J. Ahzem
J. Ghreouis
J. Boudinar
J. Gouleb
J. Meloussi
J. Jebs
J. Abdallah
Oued Leben
Kef Nsour
Meknassy
Mezzouna
J. Nejilet
J. Rouijel
J. Bou Hedma
North – South Axis
A
20 km
Mediterranean Sea
Algeria
Eastern Basins
Tunisia
Libya
100 km
Quaternary
Miocene-Pliocene
Paleocene-Eocene
Cretaceous
Jurassic
Triassic
Fault
Town
Studied section
dolostone
gypsum
laminated dolostone with gypsum nodules
phosphatic dolostone
upper phosphorite beds
interbedded gypsum and gypsiferous clays
D
interbedded gypsum and gypsiferous clays
dolostone with dissolution cavities
phosphatic dolostone
yellow laminated dolostone
indurated phosphorite with coprolites
lower phosphorite beds
C
dolostone
gypsum
upper phosphorite beds
gypsum and gypsiferous clays
dolostone
lower phosphorite beds
B
Jebel Jebs

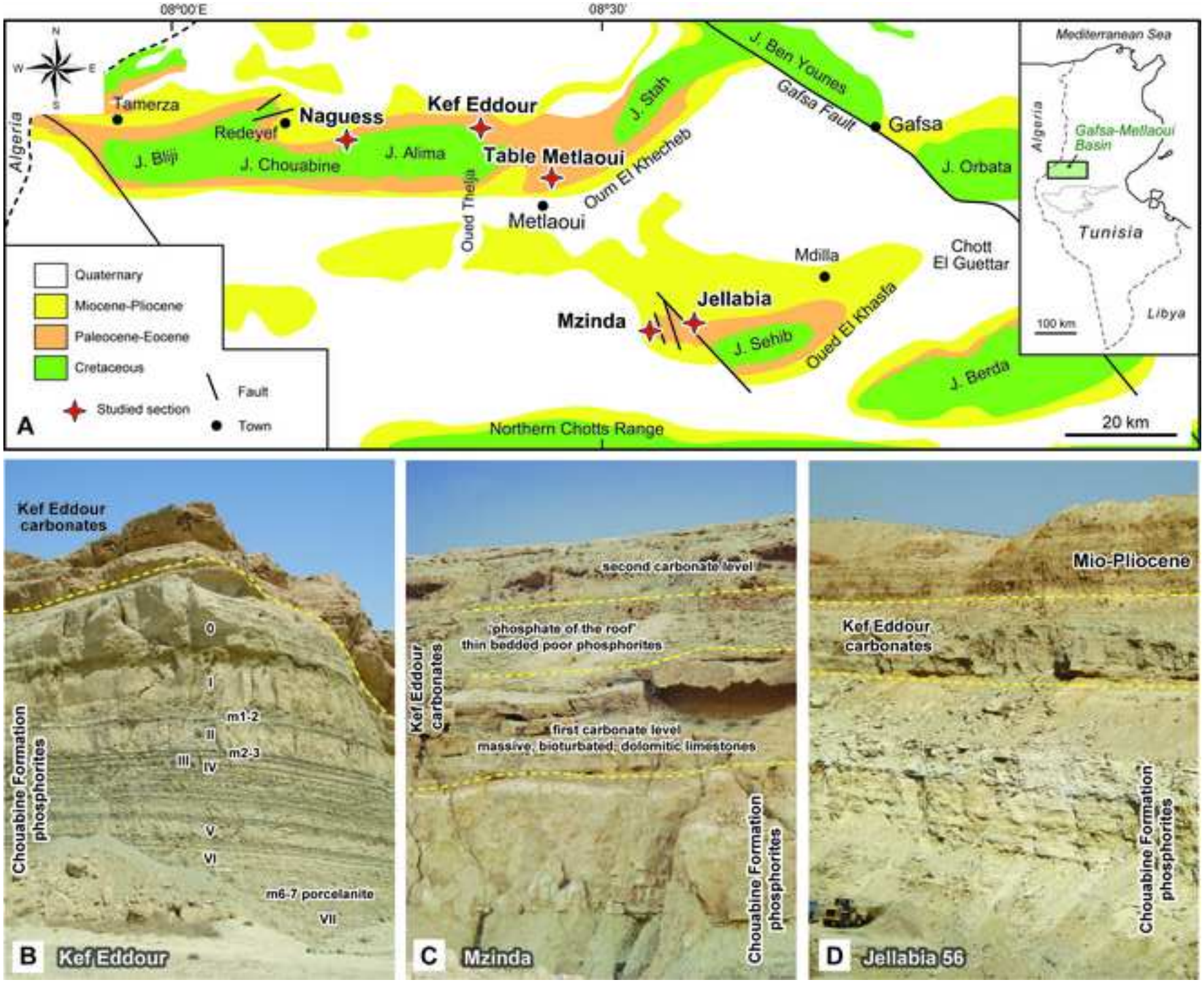
08°00'E
08°30'
N
W
E
S
Algeria
Tamerza
Redeyef
Naguess
Kef Eddour
Table Metlaoui
Metlaoui
J. Bliji
J. Chouabine
J. Alima
J. Stah
J. Ben Younes
Gafsa Fault
Gafsa
J. Orbata
Oued Thelja
Oum El Khecheb
Mdilla
Chott El Guettar
Jellabia
Mzinda
J. Sehib
Oued El Khasfa
J. Berda
Northern Chotts Range
20 km
Quaternary
Miocene-Pliocene
Paleocene-Eocene
Cretaceous
Fault
Studied section
Town
A
Mediterranean Sea
Algeria
Gafsa-Mellaoui Basin
Tunisia
Libya
100 km
Kef Eddour carbonates
0
I
m1-2
II
m2-3
III
IV
V
VI
m6-7 porcelanite
VII
Chouabine Formation phosphorites
B Kef Eddour
second carbonate level
phosphate of the roof
thin bedded poor phosphorites
first carbonate level
massive, bioturbated, dolomitic limestones
C Mzinda
Mio-Pliocene
D Jellabia 56

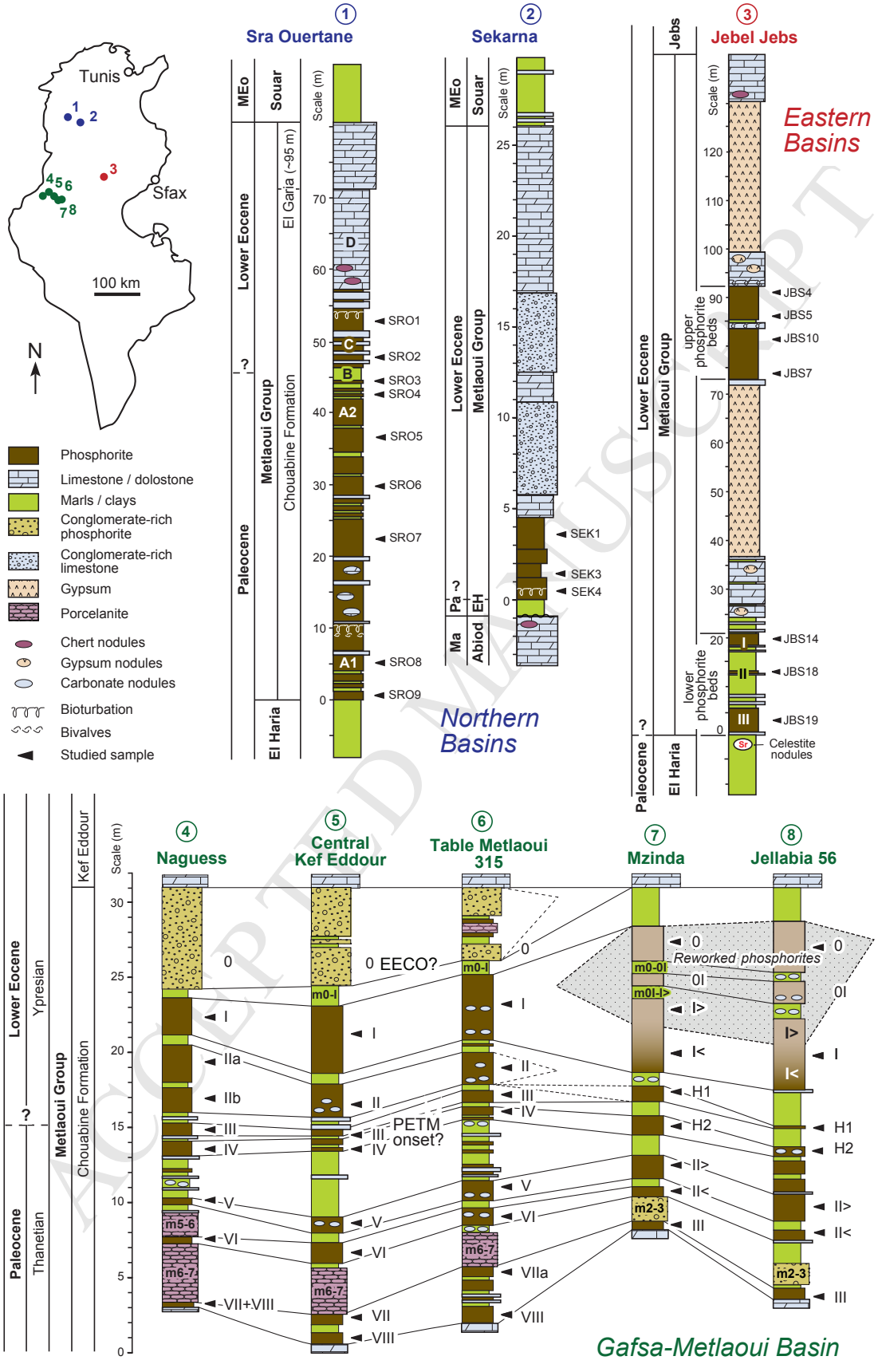

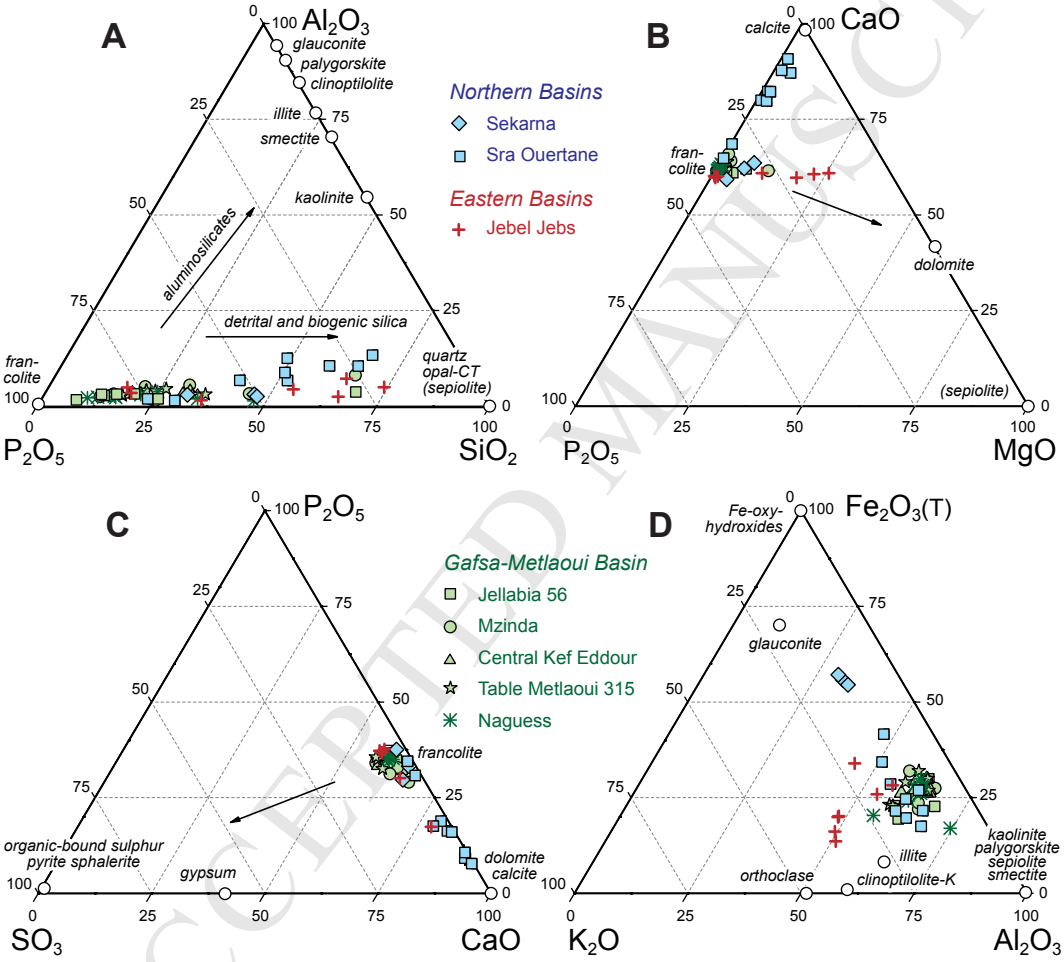

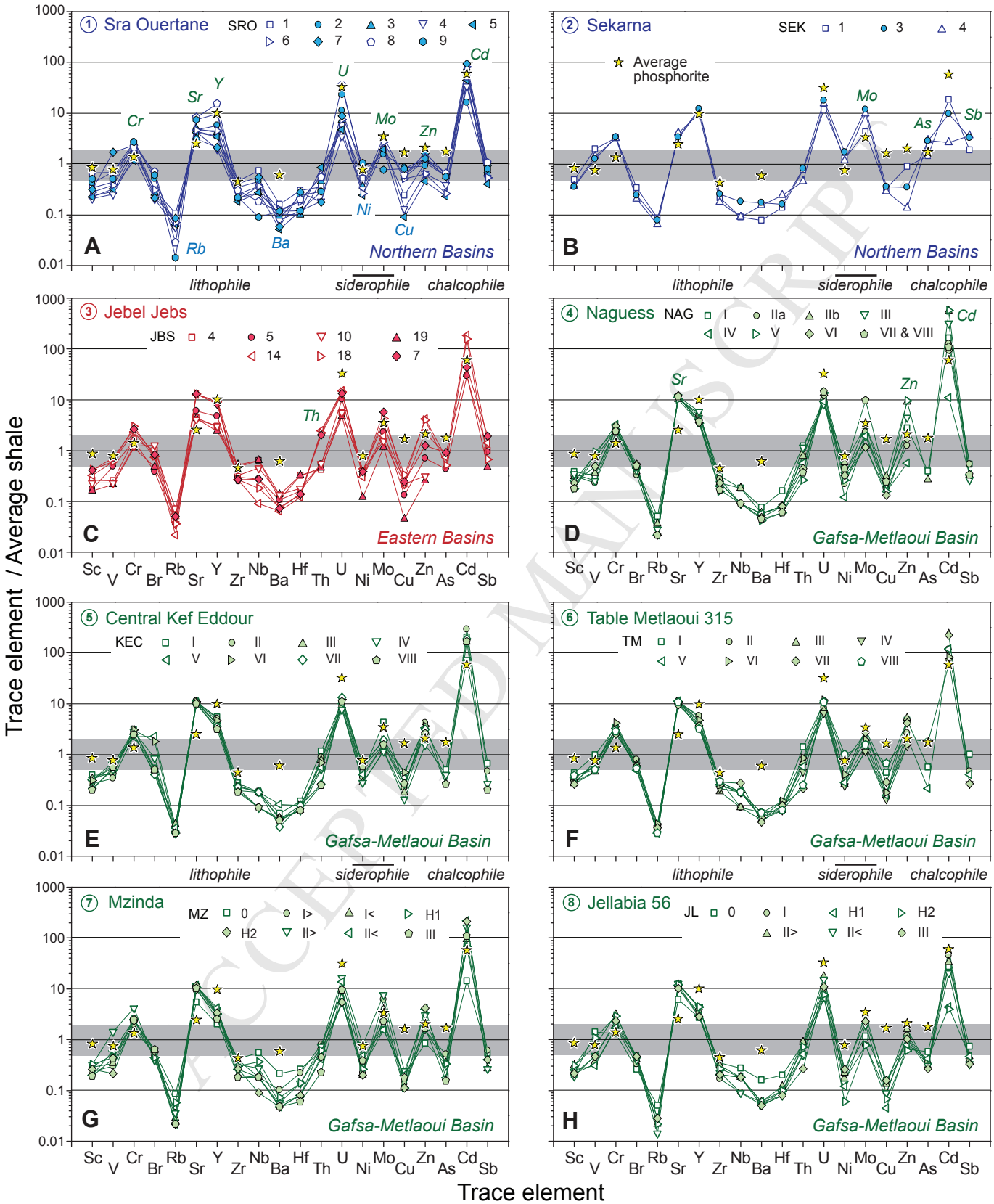

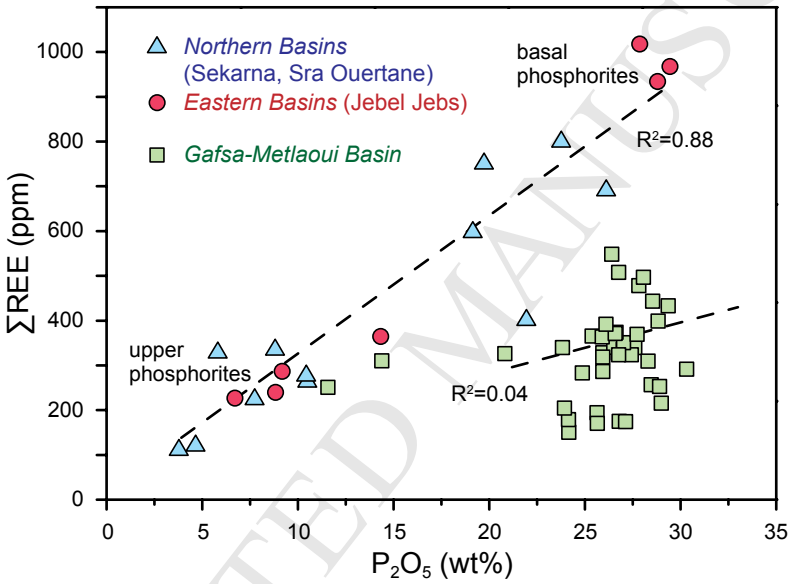

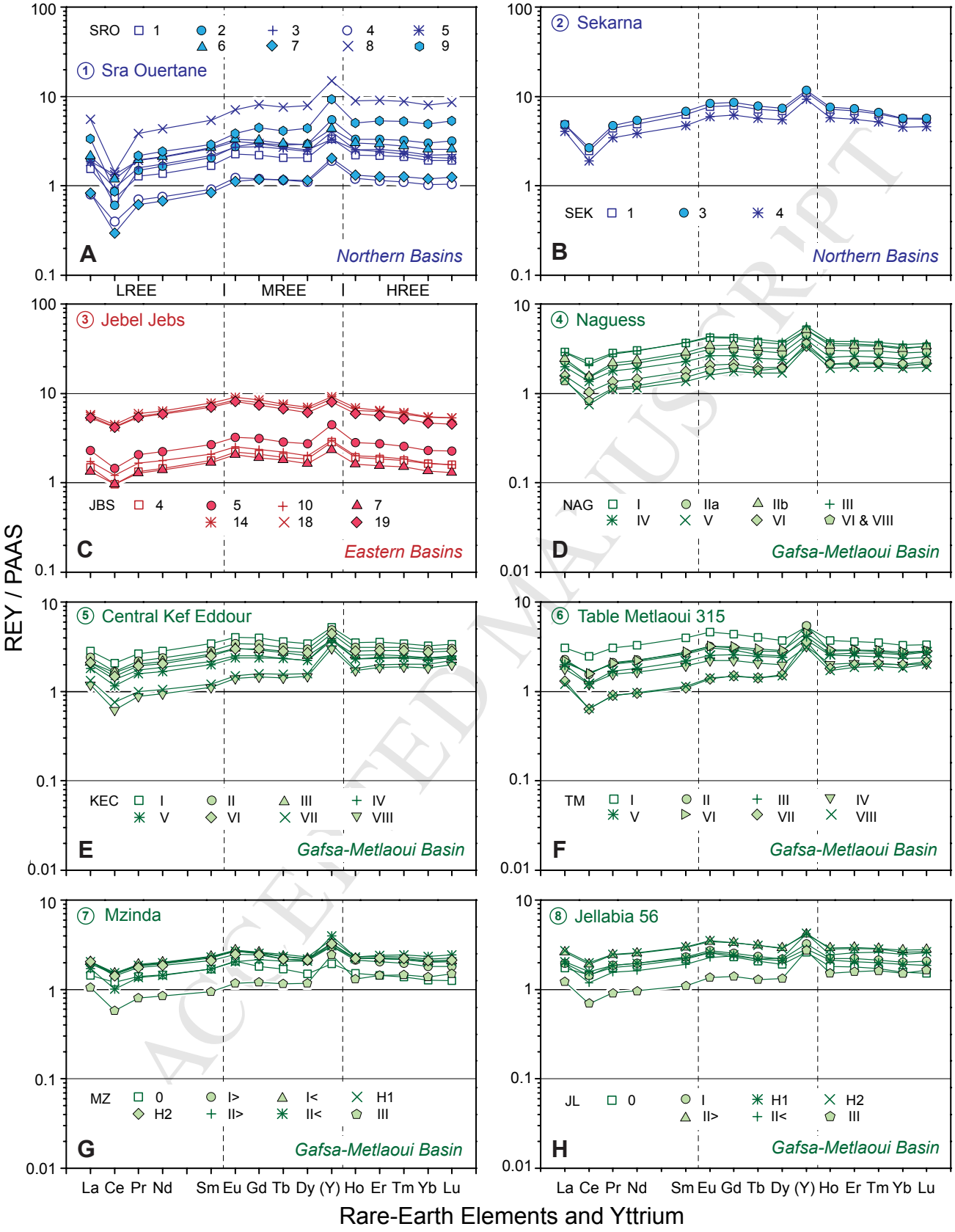

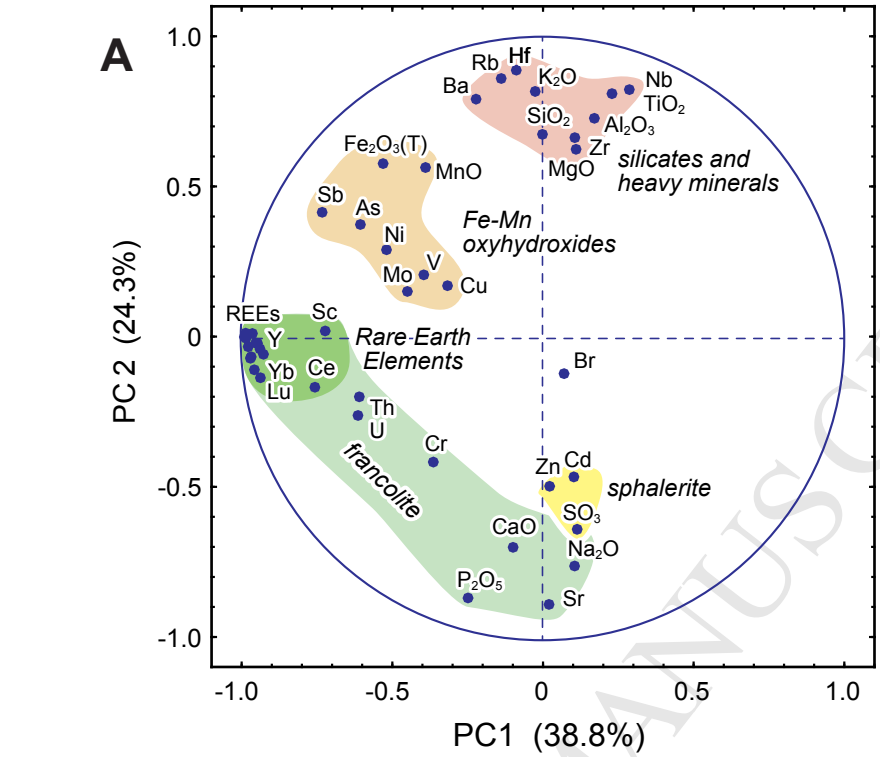

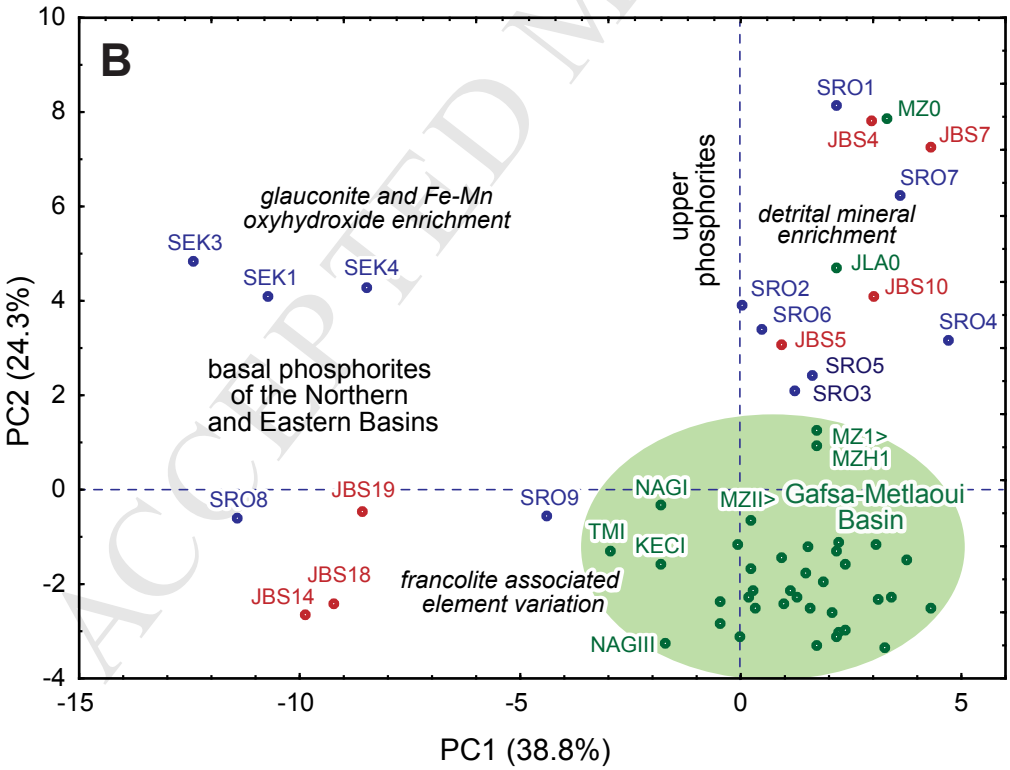

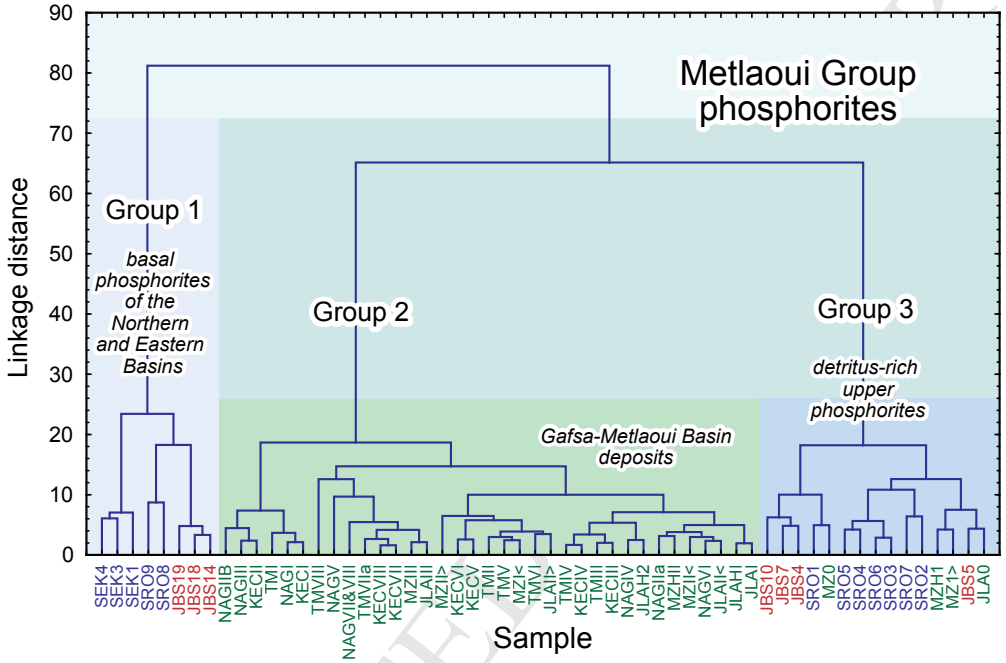

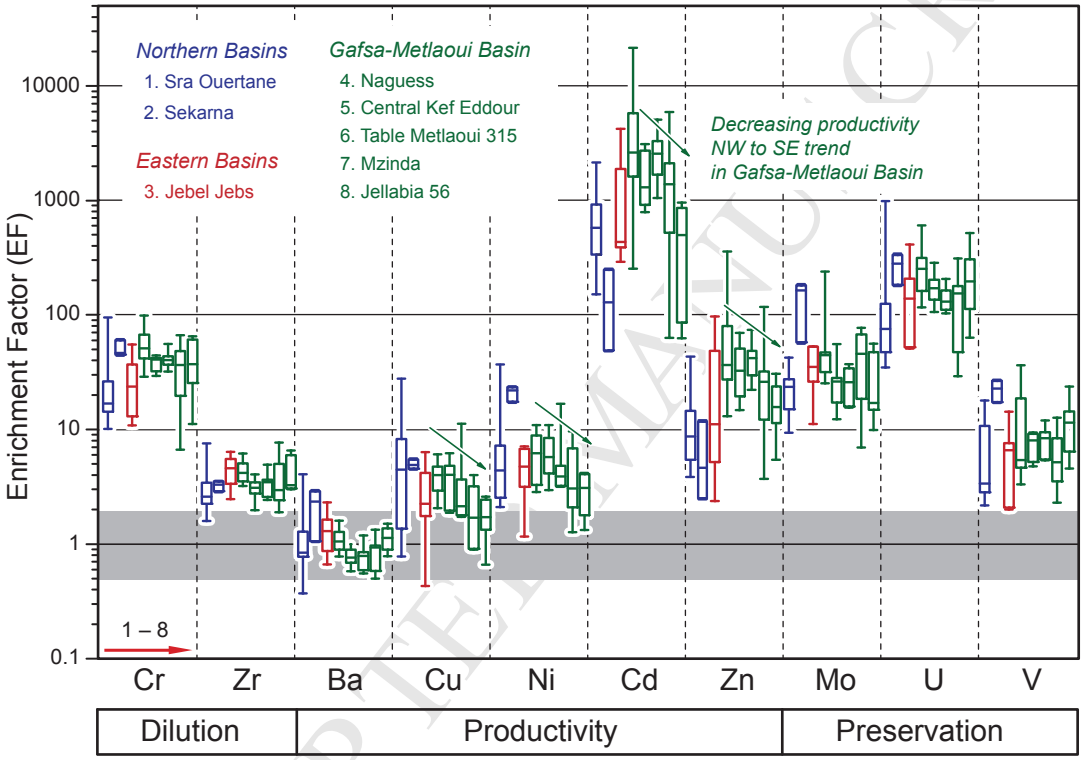

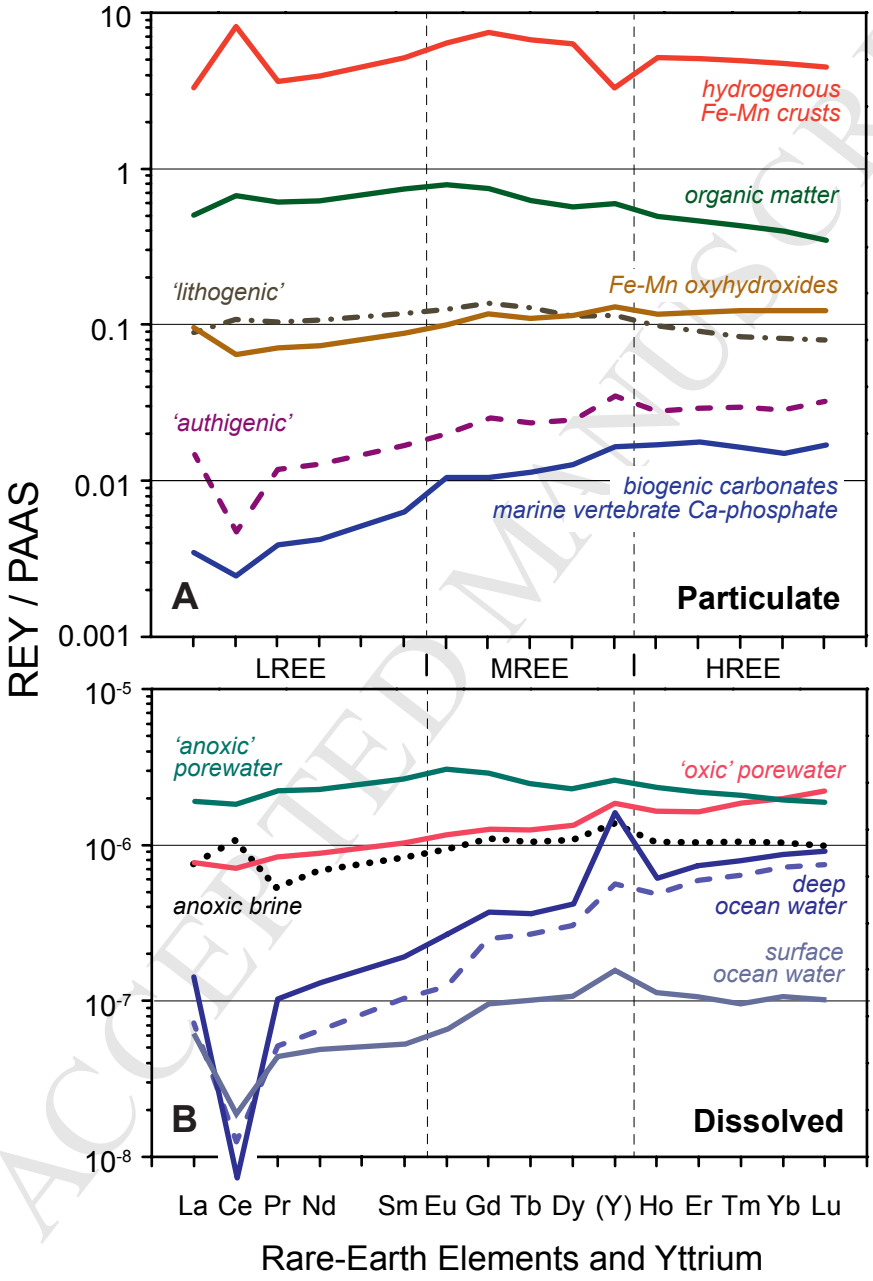

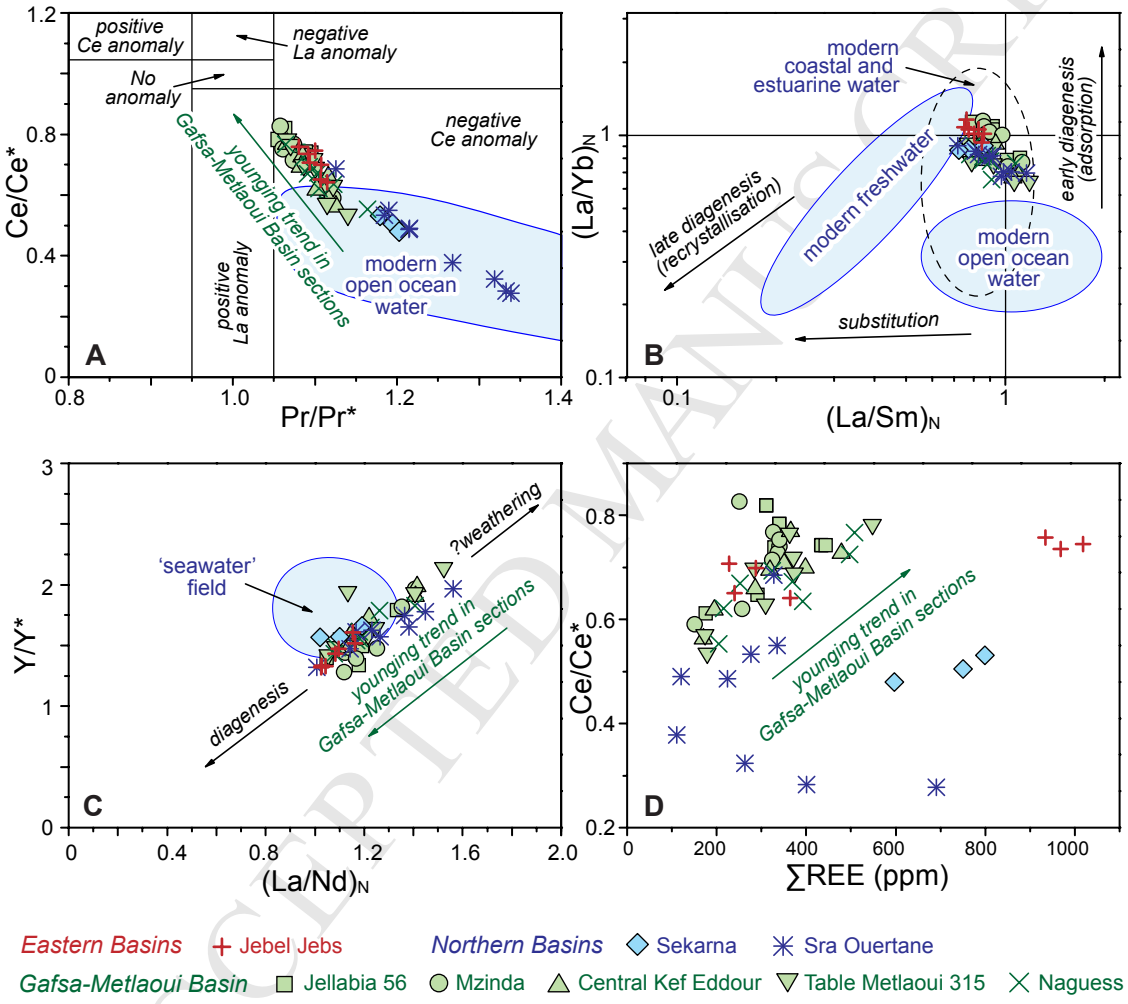

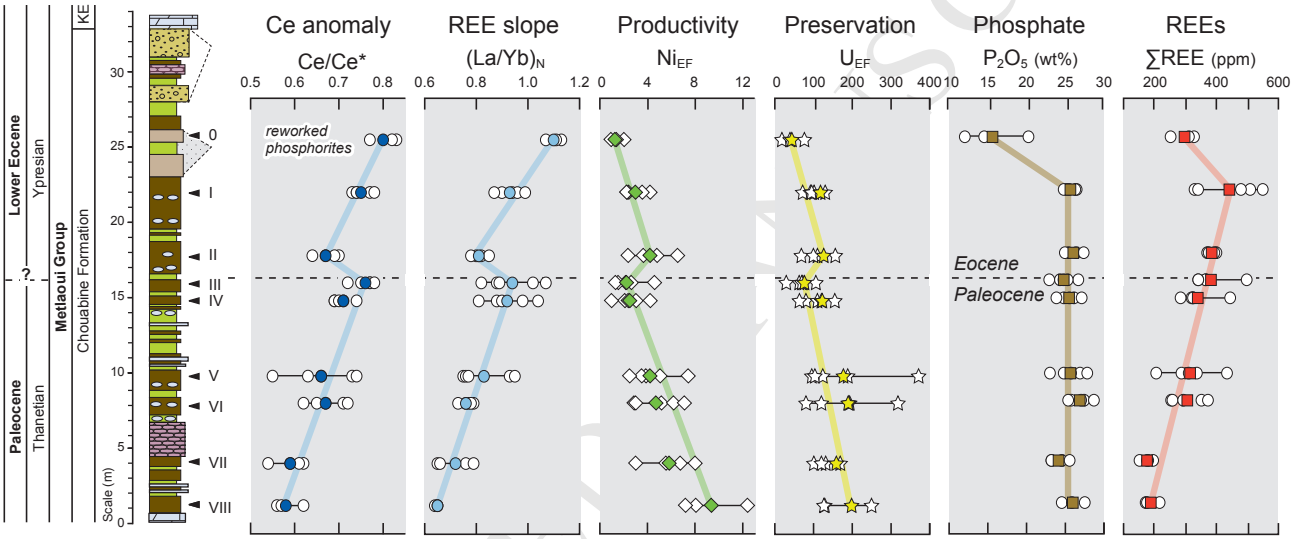

Gafsa-Metlaoui Basin

Highlights

- Tunisian Paleocene–Eocene phosphorites occur in three distinct basinal areas
- Deposits in each area have distinct geochemical signatures
- Commercial phosphorite deposits in the Gafsa-Metlaoui Basin are of Paleocene–Eocene boundary age
- The phosphorites accumulated in high productivity coastal upwelling environments
- Phosphorite deposition accompanied Paleocene-Eocene climate warming